The transcription factor EGR2 is indispensable for tissue-specific imprinting of alveolar macrophages in health and tissue repair[#]

Jack McCowan[1,2], Frédéric Fercoq[3], Phoebe M. Kirkwood[1,2], Wouter T'Jonck[1,2], Lizi M. Hegarty[1,2], Connar M. Mawer[1,4], Richard Cunningham[1,2], Ananda S. Mirchandani[1,2], Anna Hoy[1,6], Duncan C. Humphries[1,2], Gareth-Rhys Jones[1,2], Carsten G. Hansen[1,2], Nik Hirani[1,2], Stephen J. Jenkins[1,2], Sandrine Henri[7], Bernard Malissen[7], Sarah R. Walmsley[1,2], David H. Dockrell[1,2], Philippa T. K. Saunders[1,2], Leo M. Carlin[3,8], Calum C. Bain[1,2*]

1 University of Edinburgh Centre for Inflammation Research, Queens Medical Research Institute, 47 Little France Crescent, Edinburgh BioQuarter, Edinburgh, EH16 4TJ, UK

2 Institute for Regeneration and Repair, University of Edinburgh, 5 Little France Drive, Edinburgh BioQuarter, Edinburgh EH16 4UU, UK

3 Cancer Research UK Beatson Institute, Glasgow, G61 1BD, UK

4 Current address: Rayne Institute, University College London, 5 University St, Bloomsbury, London WC1E 6JF

5 Institute of Immunology & Infection Research, School of Biological Sciences, University of Edinburgh, Edinburgh EH9 3FL, UK

6 Current address: Resolution Therapeutics Limited, Centre for Regenerative Medicine, Edinburgh BioQuarter, Edinburgh, EH16 4UU, UK

7 Centre d'Immunologie de Marseille-Luminy, Aix Marseille Université UM2, INSERM, U1104, CNRS UMR7280, 13288 Marseille, France

8 Institute of Cancer Sciences, University of Glasgow, Glasgow, G61 1QH, UK

*Corresponding author & Lead Contact: calum.bain@ed.ac.uk

One Sentence Summary: EGR2 controls alveolar macrophage function in health and disease.

Abstract

Alveolar macrophages are the most abundant macrophages in the healthy lung where they play key roles in homeostasis and immune surveillance against air-borne pathogens. Tissue-specific differentiation and survival of alveolar macrophages relies on niche-derived factors, such as granulocyte-macrophage colony stimulating factor 2 (GM-CSF) and transforming growth factor beta (TGF-β). However, the nature of the downstream molecular pathways that regulate the identity and function of alveolar macrophages and their response to injury remains poorly understood. Here, we identify that the transcription factor EGR2 is an evolutionarily conserved feature of lung alveolar macrophages and show that cell-intrinsic EGR2 is indispensable for the tissue-specific identity of alveolar macrophages. Mechanistically, we show that EGR2 is driven by TGF-β and GM-CSF in a PPAR-γ-dependent manner to control alveolar macrophage differentiation. Functionally, EGR2 was dispensable for regulation of lipids in the airways, but crucial for the effective handling of the respiratory pathogen *Streptococcus pneumoniae*. Finally, we show that EGR2 is required for repopulation of the alveolar niche following sterile, bleomycin-induced lung injury and demonstrate that EGR2-dependent, monocyte-derived alveolar macrophages are vital for effective tissue repair following injury. Collectively, we demonstrate that EGR2 is an indispensable component of the transcriptional network controlling the identity and function of alveolar macrophages in health and disease.

Introduction

Alveolar macrophages provide a first line of defence against airborne pathogens, as well as maintaining lung homeostasis and orchestrating tissue repair following injury. However, in chronic lung pathologies such as allergic asthma, idiopathic pulmonary fibrosis (IPF) and chronic obstructive pulmonary disease (COPD), alveolar macrophages display aberrant activity and, in many cases, appear to perpetuate disease *(1)*. Moreover, monocytes and macrophages appear to play a particular pathogenic role in the context of severe coronavirus disease 2019 (COVID-19) *(2-4)*. Thus, understanding the environmental signals and downstream molecular pathways that control the tissue-specific imprinting of macrophages in different contexts may yield important insights into how lung-specific cues regulate homeostasis and susceptibility to disease.

Alveolar macrophages are derived from foetal progenitors that seed the lung during embryonic development *(5-7)*. However, the characteristic phenotype and functional properties of alveolar macrophages do not develop until the first few days of postnatal life in parallel with alveolarisation of the lung and are controlled by GM-CSF (also known as CSF-2) *(7, 8)* and the immunoregulatory cytokine TGF-β *(9)*. Together these cytokines induce expression of the transcription factor peroxisome proliferator-activated receptor gamma (PPAR-γ) to promote survival and tissue-specific specialisation, including upregulation of genes involved in lipid uptake and metabolism *(8)*. Consequently, mice in which *Csf2rb, Tgfbr2* or *Pparg* has been genetically ablated in myeloid cells develop spontaneous pulmonary alveolar proteinosis *(8, 9)*. However, alveolar macrophages largely fail to develop in the absence of GM-CSF and TGF-β receptor signalling due to their key role in macrophage survival. Therefore, it remains unclear if or how these factors control the tissue-specific identity and function of alveolar macrophages. Moreover, while considered the 'master transcription factor' of alveolar macrophages, PPAR-γ has been implicated in the control of other tissue macrophages, including splenic red pulp macrophages *(10, 11)*, and thus, the transcriptional network responsible for conferring specificity upon alveolar macrophage differentiation

remains unclear. Finally, if and how additional transcriptional regulators are involved in regulating these processes in the context of inflammation and repair is largely unexplored.

Here, we have used single cell RNA sequencing (scRNA-seq) to identify the transcriptional regulators expressed by alveolar macrophages. We show that expression of the transcription factor EGR2 is a distinct feature of lung alveolar macrophages. Using cell-specific ablation of *Egr2* and mixed bone marrow chimeric mice, we show that cell-intrinsic EGR2 is indispensable for the tissue-specific identity of alveolar macrophages and their ability to control infection with a major respiratory pathogen, *Streptococcus pneumoniae*. RNA sequencing (RNA-seq) shows that EGR2 controls a large proportion of the core transcriptional signature of alveolar macrophages, including expression of *Siglec5, Epcam* and *Car4*. Mechanistically, we show that EGR2 expression is induced by TGF-β and GM-CSF-dependent signalling, and acts to maintain expression of CCAAT-enhancer-binding protein beta (C/EBP-β) to control alveolar macrophage differentiation. Finally, using the bleomycin-induced model of lung injury and a combination of fate mapping approaches, we show that post-injury repopulation of the alveolar macrophage niche occurs via differentiation of bone marrow-derived cells in an EGR2-dependent manner and that these monocyte-derived macrophages are indispensable for effective tissue repair and resetting of tissue homeostasis.

Results

EGR2 expression is a selective property of alveolar macrophages

To begin to dissect the molecular pathways underlying the niche-specific imprinting of alveolar macrophages, we performed scRNA-seq of murine lung mononuclear phagocytes from lung digests to identify the transcriptional profile of alveolar macrophages. To this end, non-granulocytic $CD45^+$ cells from lungs of *Rag1*$^{-/-}$ mice were purified by FACS and sequenced using the 10x Chromium platform (**Supplementary Figure 1A**). *Rag1*$^{-/-}$ mice were used to enrich for myeloid cells and reduce potential contamination by lymphocyte-macrophage doublets. 3936 cells passed quality control and were clustered using Uniform Manifold Approximation and Projection (UMAP) dimensionality reduction analysis within the *Seurat* R package. NK cells, identified by their expression of *Ncr1, Nkg7* and *Gzma*, were excluded (**Supplementary Figure 1A, B**) and the remaining myeloid cells were re-clustered to leave six clusters of mononuclear phagocytes, and these were annotated using known landmark gene expression profiles (**Figure 1A, B**). Cluster 1 represented monocytes based on their expression of *Itgam* (encoding CD11b), *Csf1r* and *Cd68,* and could be divided into classical and non-classical monocytes based on expression of *Ly6c2* and *Treml4* respectively (**Figure 1A, B**). Cluster 2 represented interstitial macrophages based on their high expression of *Cx3cr1*, *Cd68, Csf1r* and *H2-Aa* and lack of the *Xcr1* and *Cd209a* genes which defined cDC1 (cluster 5) and cDC2 (cluster 6) respectively. Alveolar macrophages (cluster 3) formed the largest population and could be defined by their expression of *Itgax* (encoding CD11c), *Siglec5* (encoding SiglecF) and *Car4*, and lack of *Cx3cr1* and *Itgam*. Cluster 4 was transcriptionally similar to cluster 3, but was defined by genes associated with cell cycle, including *Mki67, Birc5* and *Tubb5,* suggesting these represent proliferating alveolar macrophages (**Figure 1A, B**).

Next, we compared gene expression profiles of these clusters, focussing on genes more highly expressed by alveolar macrophages relative to all other mononuclear phagocytes. 722 genes fitted these criteria, including *Fapb1*, *Spp1* (encoding osteopontin) and *Cidec* which are known to be specifically and highly expressed by alveolar macrophages (**Data File S1**) *(12, 13)*. Within this cassette of genes, we turned

our attention to genes encoding transcription factors/regulators, as we hypothesised that these might control the tissue specific differentiation of alveolar macrophages. As expected, these included *Pparg, Cebpb* and *Bhlhe41* which have been shown to control the development and self-renewal capacity of alveolar macrophages *(8) (10, 14-16)* (**Figure 1C**). However, this analysis also revealed transcription factors such as *Id1, Klf7* and *Egr2* which have not previously been implicated in the control of alveolar macrophage differentiation. We focussed on EGR2, which is part of a family of early growth response (EGR) transcription factors, comprising EGR1-4, as *Egr2* appeared to be expressed in a particularly selective manner by alveolar macrophages (**Figure 1D**) when compared with other tissue macrophages at mRNA (**Figure 1E**) and protein level (**Figure 1F, G & Supplementary Figure 2A**). In contrast, while highly expressed by alveolar macrophages, *Pparg* was also expressed at a high level by splenic red pulp macrophages (**Figure 1E**), consistent with previous reports *(10, 11)*. Of note, we did detect moderate EGR2 expression in F4/80^{lo} mononuclear phagocytes in adipose tissue, whereas F4/80^{hi} macrophage had low levels of EGR2 (**Figure 1G**). While our scRNA-seq analysis suggested that *Egr2* was expressed at lower levels by proliferating alveolar macrophages, we could not confirm this at protein level, with Ki67^{+} alveolar expressing equivalent levels of EGR2 to their Ki67^{-} counterparts (**Supplementary Figure 2B**). Next, we performed analogous analysis of *EGR2* expression across a variety of human macrophage populations from scRNA-seq data sets within the Human Cell Atlas *(17-19)*. Consistent with our analysis in the mouse, this showed that *EGR2* expression was confined to lung macrophages, and in particular *FABP4*$^{+}$ macrophages which correspond to airway macrophages (**Figure 1H**), and we confirmed this at protein level, showing that human CD163^{+}HLA-DR^{+} bronchoalveolar lavage (BAL) macrophages uniformly express EGR2 (**Supplementary Figure 2C**). Thus, these data demonstrate that EGR2 expression is a constitutive, specific and evolutionarily conserved feature of alveolar macrophages.

EGR2 is required for the phenotypic identity of alveolar macrophages

Previous work has suggested that EGR1 and EGR2 act in a redundant manner *(20)*, while other studies have suggested EGR transcription factors are completely dispensable for macrophage differentiation *(21)*. However, many of these studies were performed *in vitro* and the roles of EGRs in tissue-specific macrophage differentiation has not been assessed comprehensively *in vivo*, in part, due to the postnatal lethality of global *Egr2*$^{-/-}$ mice *(22, 23)*. To determine the role of EGR2 in alveolar macrophage development and differentiation, we crossed *Lyz2*^{Cre} mice *(24)* with *Egr2*$^{fl/fl}$ mice *(25)*, to generate a strain in which myeloid cells, including monocytes, macrophages, dendritic cells and neutrophils, lack EGR2 in a constitutive manner. We performed unbiased UMAP flow cytometry analysis on lung leukocytes obtained from *Lyz2*^{Cre}.*Egr2*$^{fl/fl}$ mice and *Egr2*$^{fl/fl}$ littermate controls, focussing on 'lineage' negative (CD3^{-}CD19^{-} NK1.1^{-}Ly6G^{-}) CD11c^{+} and CD11b^{+} cells in lung digests (**Figure 2A**). Surface marker analysis of cells pooled from *Egr2*$^{fl/fl}$ and *Lyz2*$^{Cre/+}$.*Egr2*$^{fl/fl}$ mice confirmed the presence of alveolar and interstitial macrophages, eosinophils and subsets of dendritic cells and monocytes (**Figure 2A**) and this was validated by manual gating (**Figure 2B** & **Supplementary Figure 3A**). Due to their CD11c^{hi}CD11b^{-} phenotype, alveolar macrophages clustered separately from the other CD11b^{+} myeloid cells (**Figure 2A-C**). All myeloid cells, including alveolar macrophages, were equally abundant in the lungs of *Egr2*$^{fl/fl}$ and *Lyz2*$^{Cre/+}$.*Egr2*$^{fl/fl}$ mice (**Figure 2D, E**). However, whereas alveolar macrophages from *Egr2*$^{fl/fl}$ mice expressed high levels of SiglecF, the majority of alveolar macrophages obtained from *Lyz2*$^{Cre/+}$.*Egr2*$^{fl/fl}$ mice lacked SiglecF expression (**Figure 2F**), explaining their distinct positioning within the alveolar macrophage cluster in the UMAP analysis. Indeed only ~5% of alveolar macrophages in *Lyz2*$^{Cre/+}$.*Egr2*$^{fl/fl}$ mice expressed high levels of SiglecF, and further analysis showed that these expressed high levels of EGR2 (**Figure 2G**), suggesting that the SiglecF^{+} cells remaining in the *Lyz2*$^{Cre/+}$.*Egr2*$^{fl/fl}$ mouse represent cells that have escaped Cre-mediated recombination. Consistent with this, SiglecF^{+} cells in the *Lyz2*$^{Cre/+}$.*Egr2*$^{fl/fl}$ mouse expressed high levels of CD11c equivalent to alveolar macrophages from control mice, whereas SiglecF^{-} alveolar macrophages expressed lower levels of CD11c (**Figure 2H**). We did not detect differences in the proliferative activity of *Egr2*-sufficient and -deficient alveolar macrophages (**Figure 2H**).

Importantly and consistent with the lack of EGR2 expression by other tissue resident macrophages, we saw no effect on the cell number and expression of signature markers by resident macrophages in other tissues, including in the spleen where macrophages share a dependence on PPAR-γ *(10, 11)* and adipose tissue where we detected EGR2 expression (**Supplementary Figure 3B-D**). Thus, these data demonstrate that while EGR2 expression is dispensable for alveolar macrophages survival and self-maintenance, it is indispensable for imprinting key phenotypic features of the cells in the healthy lung.

EGR2 controls the tissue-specific transcriptional programme of alveolar macrophages

The failure of alveolar macrophages from *Lyz2*$^{Cre/+}$.*Egr2*$^{fl/fl}$ mice to express SiglecF suggested that the tissue-specific differentiation programme of these cells may be altered by *Egr2* deficiency. Hence, to ascertain the global effects of *Egr2* deletion on alveolar macrophage differentiation, we next performed bulk RNA-seq of CD11c^{hi}CD11b^{lo} alveolar macrophages from lung digests of *Egr2*$^{fl/fl}$ and *Lyz2*$^{Cre/+}$.*Egr2*$^{fl/fl}$ mice (using only SiglecF^{-} macrophages from *Lyz2*$^{Cre/+}$.*Egr2*$^{fl/fl}$ mice to exclude confounding effects of EGR2-sufficient alveolar macrophages) (**Supplementary Figure 4**). Unbiased clustering confirmed the biological replicates from each group were highly similar (**Figure 3A**) and differential gene expression (DEG) analysis revealed that 858 genes were differentially expressed by at least 2-fold (417 and 440 genes downregulated and upregulated, respectively) (**Data File S2**). Consistent with our flow cytometry analysis, *Siglec5*, which encodes SiglecF, was one of the most downregulated genes in *Egr2*-deficient alveolar macrophages (**Figure 3B**). Many of the most differentially expressed genes formed part of the alveolar macrophage gene set identified in our scRNA-seq analysis. Moreover, approximately 30% of the core alveolar macrophage signature identified by the ImmGen consortium *(12)* was altered by *Egr2* deficiency (32 genes) (**Figure 3B, C**), including the expression of *Spp1, Epcam, Car4* and *Fabp1*, all of which were confirmed by flow cytometry or qPCR (**Figure 3D, E**). The vast majority of these 'signature' genes was downregulated in *Egr2*-deficient macrophages compared with their *Egr2*-sufficient counterparts. Gene Ontology (GO) analysis revealed that the top pathways affected by *Egr2* deficiency were 'Chemotaxis', 'Cell chemotaxis' and 'Immune system process' (**Supplementary Table 1**). Consistent with this, the

expression of chemokine receptors, such as *Ccr2* and *Cx3cr1*, was elevated in alveolar macrophages from *Lyz2*$^{Cre/+}$.*Egr2*$^{fl/fl}$ mice compared with their *Egr2*$^{fl/fl}$ counterparts (**Figure 3F**). Genes encoding antigen presentation machinery, such as *H2-Aa, H2-Eb1, Ciita* and *Cd74* were also upregulated in alveolar macrophages from *Lyz2*$^{Cre/+}$.*Egr2*$^{fl/fl}$ mice. In parallel, there was significantly greater expression of MHCII at the protein level in *Egr2*-deficient alveolar macrophages (**Figure 3F**). Indeed, over 50 genes upregulated in *Egr2*-deficient alveolar macrophages were genes that defined interstitial macrophages in our scRNA-seq analysis, including *Cd63, Mafb, Mmp12* and *Msr1* (**Figure 3D**, **Data File S2**). Thus, EGR2 ablation renders alveolar macrophages transcriptionally more similar to their interstitial counterparts.

Further phenotypic analysis revealed reduced expression of 'core signature' alveolar macrophage markers TREM1 and CD11a at protein level in the context of *Egr2* deficiency (**Figure 3G**). EpCAM and CD11a expression have been implicated in regulating adherence to and patrolling of the lung epithelium by alveolar macrophages *(26)*, which suggested these behaviours may be altered by *Egr2* deficiency. However, *ex vivo* analysis of live Precision-Cut Lung Slices (PCLS) showed that CD11c^{+} alveolar macrophages remained sessile in both strains, as compared with Ly6G^{+} CD11b^{+} neutrophils moving freely in sections (**Data file S3 and Supplementary Figure 5A**). Nevertheless, morphodynamics analysis of macrophages demonstrated increased changes in cell shape over time (as shown by the standard deviation of cell sphericity) indicating a more active behavior of *Egr2*-deficient macrophages (**Data file S4 and Supplementary Figure 5B, C**). In addition to this, while we found equivalent numbers of alveolar macrophages amongst tissue digests, we obtained consistently higher numbers of alveolar macrophages in the bronchoalveolar lavage (BAL) fluid of *Lyz2*$^{Cre/+}$.*Egr2*$^{fl/fl}$ mice (**Figure 3H**). Taken together, these data suggest the EGR2-dependent differentiation programme may control the ability of alveolar macrophages to adhere to and interact with cells of their niche in the airways.

EGR2 controls distinct functional characteristics of alveolar macrophages

Individuals with mutations in *EGR2* develop peripheral neuropathies due to the crucial role for EGR2 in Schwann cell function *(26)*. However, many of these individuals also frequently encounter respiratory

complications, including recurrent pneumonias and/or restrictive pulmonary disease, and in some cases respiratory failure *(26)*. The cause of respiratory compromise in these individuals remains unexplained. To determine if alterations in alveolar macrophage behaviour may contribute to this, we next tested the function of *Egr2*-deficient alveolar macrophages. A major homeostatic function of alveolar macrophages is the regulation of pulmonary surfactant, and the absence of alveolar macrophages results in the development of pulmonary alveolar proteinosis *(14, 28-32)*. We first examined neutral lipid context of alveolar macrophages using LipidTox. We found a small but significant increase in the neutral lipid context in alveolar macrophages from *Lyz2*$^{Cre/+}$.*Egr2*$^{fl/fl}$ mice mice compared with *Egr2*$^{fl/fl}$ littermates (**Figure 4A**). Despite this, *Egr2* deficiency did not lead to spontaneous pulmonary alveolar proteinosis, as there were no differences in the levels of total protein in BAL fluid from *Lyz2*$^{Cre/+}$.*Egr2*$^{fl/fl}$ and *Egr2*$^{fl/fl}$ mice at either 4 or >9 months of age, a time at which proteinosis is detectable in *Csf2rb*$^{-/-}$ mice *(32)* (**Figure 4B**). Moreover, there was no detectable increase in the presence of dead cells in the BAL fluid, a common consequence of alveolar macrophage deficiency (**Figure 4C**). However, these results were confounded by the fact that the majority of alveolar macrophages in aged (>9 months) *Lyz2*$^{Cre/+}$.*Egr2*$^{fl/fl}$ mice was now EGR2-sufficient, with most cells expressing high levels of SiglecF (**Figure 4D**). These findings suggested that the cells that had escaped Cre recombination may have a competitive advantage over their EGR2-deficient counterparts. Indeed, the absolute number of SiglecF^{+} alveolar macrophages no longer differed between aged *Egr2*$^{fl/fl}$ and *Lyz2*$^{Cre/+}$.*Egr2*$^{fl/fl}$ mice (**Figure 4E**). These data are consistent with other studies noting age-related repopulation of the alveolar niche with Cre 'escapees' in the *Lyz2*^{Cre} mouse *(9)*. Notably, however, this preferential expansion of EGR2-sufficient 'escapees' did not relate to differences in the level of proliferation by EGR2-defined subsets, with identical frequencies of Ki67^{+} cells amongst EGR2-sufficient and -deficient macrophages in young adult and aged mice (**Figure 2H & Figure 4F**).

In an attempt to circumvent the confounding effects of these escapees, we generated a second strain to delete *Egr2* from macrophages by crossing *Egr2*$^{fl/fl}$ mice with mice expressing 'improved' Cre recombinase under control of the endogenous *Fgcr1* promoter (*Fcgr1*^{iCre})*(13)*. By using

Fcgr1^{iCre}.*Rosa26*$^{LSL\text{-}RFP}$ reporter mice, we confirmed that this approach led to efficient Cre recombination in alveolar macrophages, as well as in other tissue macrophages, but not in other leukocytes (**Supplementary Figure 6A**). Importantly, alveolar macrophages from *Fcgr1*$^{iCre/+}$.*Egr2*$^{fl/fl}$ mice phenocopied those from *Lyz2*$^{Cre/+}$.*Egr2*$^{fl/fl}$ mice (**Supplementary Figure 6B**), but the frequency of Cre escapees was markedly lower in *Fcgr1*$^{iCre/+}$.*Egr2*$^{fl/fl}$ mice compared with *Lyz2*$^{Cre/+}$.*Egr2*$^{fl/fl}$ mice (**Supplementary Figure 6C, D**). Despite this, we did not detect the development of proteinosis or accumulation of dead cells in the BAL fluid of aged *Fcgr1*$^{iCre/+}$.*Egr2*$^{fl/fl}$ mice compared to their littermate controls (**Supplementary Figure 6E**). Consistent with this, *Egr2* deficiency had little if any effect on the expression of molecules associated with lipid uptake and metabolism that are characteristic of normal alveolar macrophages *(8)* (**Figure 4G & Supplementary Figure 6F**). Thus, while EGR2 is indispensable for the phenotypic identity of alveolar macrophages, it appears to be largely dispensable for lipid regulation.

We next sought to determine if EGR2-dependent differentiation controls protective immune functions of alveolar macrophages. To do so, we infected *Egr2*$^{fl/fl}$ mice and *Lyz2*$^{Cre/+}$.*Egr2*$^{fl/fl}$ mice with $1x10^4$ colony forming units (CFU) *Streptococcus pneumoniae*, based on previous work showing that wild type alveolar macrophages efficiently clear infection at this dose *(33, 34)*. This showed that the majority of *Egr2*$^{fl/fl}$ mice (8 out of 12) had cleared infection at 14 hours post infection, whereas the majority of *Lyz2*$^{Cre/+}$.*Egr2*$^{fl/fl}$ mice (8 out of 10) had detectable bacteria in the airways at this timepoint (**Figure 4H**). Importantly, the failure to handle bacteria did not reflect the loss of tissue resident macrophages that can occur during inflammation or infection, as alveolar macrophages continued to dominate the airways in both groups (**Figure 4I, J**). Similarly, increased bacteria in *Lyz2*$^{Cre/+}$.*Egr2*$^{fl/fl}$ mice is also unlikely to reflect an effect in neutrophils, as neutrophil recruitment was negligible in both strains, and, although targeted in the *Lyz2*^{Cre} system, neutrophils failed to express EGR2 during health or in the context of *S. pneumoniae* infection (**Supplementary Figure 7A**). Instead, our RNA-seq analysis showed that expression of genes encoding molecules for the recognition, opsonisation and elimination of bacteria, including *Colec12, Wfdc10, C3* and *Marco*, the latter of which has been shown to be indispensable for immunity to *S.*

pneumoniae (35), were significantly reduced in *Egr2*-deficient alveolar macrophages (**Figure 4K**). Thus, EGR2-dependent differentiation is crucial for equipping alveolar macrophages with the machinery to capture and destroy pneumococci.

EGR2 expression by alveolar macrophages is dependent on TGFβ and GM-CSF

Alveolar macrophages derive from foetal monocytes that seed the developing lung in the late gestational period *(7)*. To determine the point at which EGR2 is first expressed, we assessed EGR2 expression by E10.5 yolk sac macrophages, by macrophages in the embryonic lung (E16.5) and by $CD11c^{hi}CD11b^{lo}$ alveolar macrophages in the neonatal and adult lung using the ImmGen database. This revealed that *Egr2* was absent from yolk sac macrophages and macrophages in the embryonic lung at E16.5, but it was expressed by both neonatal and adult alveolar macrophages (**Figure 5A**), suggesting that it is induced during alveolarization in the neonatal period. Consistent with this, we found high expression of EGR2 at protein level by neonatal (d1) $CD64^{+}$ lung macrophages (sometimes referred to as 'pre-alveolar macrophages') in $Egr2^{fl/fl}$ mice; as expected, this expression was deleted efficiently in $Lyz2^{Cre/+}.Egr2^{fl/fl}$ mice (**Figure 5B, C**). Importantly, $Ly6C^{hi}$ monocytes in the lung of d1 neonatal mice lacked any expression of EGR2 (**Figure 5B, C**), reinforcing the selectivity of EGR2 expression even at this highly dynamic stage of myeloid cell development in the lung. Consistent with our analysis of mature alveolar macrophages in adult mice, *Egr2* deletion had no impact on the frequency and absolute number of pre-alveolar macrophages (**Figure 5D**). However, phenotypic differences were already apparent in macrophages from $Lyz2^{Cre/+}.Egr2^{fl/fl}$ mice at this stage, with reduced CD11c and SiglecF expression which persisted into adulthood (**Figure 5E, F**). In parallel, EpCAM expression was absent from alveolar macrophages in the neonatal period and was progressively upregulated with age in an EGR2-dependent manner (**Figure 5F**). CD11b expression, which is downregulated in mature alveolar macrophages, was found on pre-alveolar macrophages in both $Egr2^{fl/fl}$ and $Lyz2^{Cre/+}.Egr2^{fl/fl}$ mice, and it was downregulated to the same extent with age in both strains.

We next set out to determine the environmental factors that drive EGR2 expression. Many studies employing *in vitro* culture systems have described EGR2 expression as a feature of 'alternatively activated'

macrophages, dependent on IL-4R signalling *(36, 37).* Importantly, expression of EGR2 by alveolar macrophages was independent of IL-4R signalling (**Figure 5G & Supplementary Figure 6G**), as were key EGR2-dependent phenotypic traits, such as SiglecF and EpCAM expression (**Supplementary Figure 6F**). TGF-β has recently been shown to be crucial for the development of alveolar macrophages *(9)* and thus we next explored if the TGF-β-TGF-βR axis drives expression of EGR2. To do so, we generated a new mouse line by crossing *Fcgr1*^{iCre} mice to mice with LoxP sites flanking the *Tgfbr2* allele (*Tgfbr2*$^{fl/fl}$). Consistent with the crucial role for TGF-βR in controlling alveolar macrophage development *(9)*, there was a paucity of alveolar macrophages in the lungs of neonatal *Fcgr1*$^{iCre/+}$.*Tgfbr2*$^{fl/fl}$ compared with *Fcgr1*$^{+/+}$.*Tgfbr2*$^{fl/fl}$ and *Fcgr1*$^{iCre/+}$.*Tgfbr2*$^{fl/+}$ controls (**Figure 5H**). Strikingly, while CD11c^{+}CD11b^{lo} alveolar macrophages expressed high levels of EGR2 in control groups, EGR2 expression was largely abolished in *Fcgr1*$^{iCre/+}$.*Tgfbr2*$^{fl/fl}$ mice, demonstrating that TGF-βR signalling is vital for EGR2 induction *in vivo*. As *Fcgr1*$^{iCre/+}$.*Tgfbr2*$^{fl/fl}$ developed fatal seizures between d14 and d21 of age, perhaps reflecting the indispensable role for TGF-βR in controlling microglia activity *(38, 39),* we were unable to carry out further analyses using this strain.

Given the central role for GM-CSF in alveolar macrophage development, we also assessed the role of GM-CSF in driving EGR2 expression using an *in vitro* culture system in which Ly6C^{hi} monocytes from bone marrow were FACS-purified and cultured with recombinant CSF-1 or GM-CSF. This revealed that GM-CSF was also capable of driving EGR2 expression in this system (**Figure 5I**). Given that GM-CSF receptor and TGF-βR signalling is known to induce expression of PPAR-γ *(8, 9, 14),* we next determined if PPAR-γ is upstream of EGR2. Analysis of a publicly available dataset (ImmGen) comparing the transcriptional profile of *Pparg*-sufficient and -deficient alveolar macrophages revealed downregulation (2.1-fold change) of *Egr2* in the context of *Pparg* deficiency (**Figure 5j**). In contrast, *Pparg* expression was unaffected in alveolar macrophages from *Lyz2*$^{Cre/+}$.*Egr2*$^{fl/fl}$ mice (**Figure 5K**), suggesting EGR2 is downstream of PPAR-γ. Another transcription factor implicated in controlling alveolar macrophage differentiation is C/EBPβ *(15)* and EGR2 has been shown to modulate C/EBPβ *in vitro (36)*. *Egr2*

deficiency led to reduced expression of C/EBPβ at mRNA (**Figure 5K**) and protein level (**Supplementary Figure 6H**). Taken together, these data support the premise that EGR2 expression by alveolar macrophages is induced by TGF-β and GM-CSF in a PPAR-γ-dependent manner in the neonatal period and this in turn induces expression of C/EBPβ to drive tissue-specific differentiation.

Egr2 deficiency confers a competitive disadvantage on alveolar macrophages

Given the observation that EGR2-sufficient alveolar macrophages come to dominate the airspace of *Lyz2*$^{Cre/+}$.*Egr2*$^{fl/fl}$ mice, we next set out to determine if EGR2 deletion confers an intrinsic competitive disadvantage on alveolar macrophages. To this end, we generated mixed bone marrow chimeric mice by reconstituting lethally irradiated WT (CD45.1^{+}/.2^{+}) mice with a 1:1 ratio of WT (CD45.1^{+}) and either *Egr2*$^{fl/fl}$ or *Lyz2*$^{Cre/+}$.*Egr2*$^{fl/fl}$ (CD45.2^{+}) bone marrow cells (**Figure 6A**). 8 weeks after reconstitution, we found that *Egr2*-deficient and *Egr2* sufficient bone marrow contributed equally to the pools of monocytes, interstitial macrophages and dendritic cell subsets in the lung (**Figure 6B, C**). In contrast, alveolar macrophages were derived almost exclusively from WT BM in WT:*Lyz2*$^{Cre/+}$.*Egr2*$^{fl/fl}$ chimeric mice, whereas they were derived equally from both BM sources in WT:*Egr2*$^{fl/fl}$ chimeric mice (**Figure 6B, C**). These effects were not a general feature of macrophages derived from *Egr2*-deficient bone marrow, as *Egr2* deletion did not adversely affect the replenishment of splenic red pulp or adipose tissue macrophages (**Figure 6D**). The mixed BM chimeric model also confirmed that the phenotypic differences seen in alveolar macrophages from intact *Lyz2*$^{Cre/+}$.*Egr2*$^{fl/fl}$ mice were due to cell intrinsic loss of EGR2, rather than effects of *Egr2* deficiency on the lung environment (**Figure 6E, F**). We also used this system to confirm the reduced expression of C/EBPβ by alveolar macrophages deriving from *Lyz2*$^{Cre/+}$.*Egr2*$^{fl/fl}$ bone marrow (**Figure 6F**).Taken together, these results demonstrate that cell intrinsic EGR2 is indispensable for the differentiation of alveolar macrophages and repopulation of the alveolar niche following radiation-induced depletion.

Bone marrow-derived monocytes replenish the alveolar macrophage niche following lung injury

Loss of tissue resident macrophages is a frequent consequence of inflammation, including in the lung *(40)*. Thus, given that *Egr2*-deficient macrophages failed to replenish the alveolar niche following radiation treatment, we next sought to determine if EGR2 plays a role in macrophage repopulation following lung injury. The chemotherapeutic agent bleomycin is a common model of chronic lung injury and self-resolving pulmonary fibrosis *(41)*, which is characterised by initial loss of alveolar macrophages during the inflammatory phase (day 7), followed by repopulation during the fibrotic and resolution phases (from day 14 onwards) (**Figure 7A**). To determine if bone marrow-derived monocytes contribute to the alveolar macrophage compartment following bleomycin-induced injury, we used tissue protected bone marrow chimeric mice to assess replenishment kinetics without exposing the lung to the additional insult of ionising radiation (**Figure 7B**). Consistent with previous studies *(42)*, we found that bleomycin instillation led to progressive replacement of resident alveolar macrophages by BM-derived cells, with the entire alveolar macrophage compartment being replaced at 32 weeks post injury (**Figure 7B**). Interestingly, recently arrived, monocyte-derived alveolar macrophages expressed low-intermediate levels of SiglecF, with acquisition of SiglecF requiring long-term residence in the airway (**Figure 7C)**.

We next interrogated this process further to determine if monocyte-derived macrophages that accumulate in the lung parenchyma during injury can subsequently mature into alveolar macrophages during tissue repair *(42, 43).* Indeed, during the recovery phase of disease, we noted the presence of cells with features of both alveolar and interstitial macrophages ($CD11c^{hi}CD11b^{+}$ $MHCII^{+}CD64^{hi}$) in the BAL fluid (**Figure 7D**), and these cells expressed intermediate levels of SiglecF (**Figure 7E**), indicative of recent monocyte origin. To examine the relationship of these 'hybrid' cells found in the airways to elicited monocyte-derived macrophages in the lung parenchyma more directly, we performed fate mapping studies using *Cx3cr1*$^{Cre\text{-}ERT2/+}$.*Rosa26*$^{LSL\text{-}RFP/+}$ reporter mice, in which administration of tamoxifen leads to irreversible expression of RFP by CX3CR1 expressing cells *(44, 45)* (**Figure 7F**). Administration of tamoxifen led to labelling of 40-50% of $CD11b^{+}$ parenchymal macrophages in both healthy lung and at d21

post bleomycin administration (**Figure 7F**). No recombination was seen in *Cx3cr1*$^{Cre\text{-}ERT2/+}$.*Rosa26*$^{LSL\text{-}RFP/+}$ mice in the absence of tamoxifen (**Supplementary Figure 8A**). Although very low levels of recombination were detected in control alveolar macrophages, a clear population of RFP^{+} cells could be detected in the BAL of the recipients of bleomycin following tamoxifen treatment (**Figure 7F**). As monocytes are poorly labelled in this system and *Cx3cr1* levels do not change in *bona fide* resident alveolar macrophages in response to bleomycin treatment (**Supplementary Figure 8B**), these RFP^{+} cells likely represent fate-mapped, monocyte-derived CX3CR1^{+} cells. In line with this, RFP^{+} cells had a 'hybrid' CD11c^{hi}CD11b^{+}SiglecF^{int} profile, supporting the idea that these represent transitional cells (**Figure 7F**). Thus, following bleomycin-induced injury, the alveolar macrophage compartment is restored, in part, by monocytes that transition through a CX3CR1^{hi} state.

EGR2 is indispensable for alveolar macrophage repopulation and tissue repair following lung injury

Given that transitional CD11b^{+}SiglecF^{int} cells also expressed EGR2, contrasting with its restriction to SiglecF^{hi} alveolar macrophages in health (**Figure 7E**), we examined whether EGR2 is necessary for the replenishment of the alveolar niche during recovery from bleomycin-induced injury. To do this, we administered bleomycin to *Lyz2*$^{Cre/+}$.*Egr2*$^{fl/fl}$ mice and their *Egr2*$^{fl/fl}$ littermates and assessed macrophage dynamics in total lung digests. The inflammatory phase of this disorder (day 7) was associated with accumulation of CD11b^{+} macrophages and this occurred to the same extent in both strains (**Figure 8A, B**). Consistent with recent reports *(46)*, the CD11b^{+}CD64^{+} interstitial macrophage population was heterogeneous during the fibrotic phase of disease (d14-d21), with MHCII^{+} and MHCII^{lo}CD36^{+}Lyve1^{+} subsets. This pattern was identical in between *Egr2*$^{fl/fl}$ and *Lyz2*$^{Cre/+}$.*Egr2*$^{fl/fl}$ groups, as were the numbers of Ly6C^{hi} monocytes and neutrophils (**Supplementary Figure 9A-C**). We did however detect a significant reduction in eosinophils in the lung of *Lyz2*$^{Cre/+}$.*Egr2*$^{fl/fl}$ mice compared with *Egr2*$^{fl/fl}$ littermates, despite eosinophils lacking EGR2 expression and no differences in the level of eosinophil chemoattractant CCL11 (**Supplementary Figure 9D-F**).

A reduction in alveolar macrophages was observed in both groups on day 7 after administration of bleomycin. Although this began to be restored by day 14 in *Egr2*$^{fl/fl}$ control mice, this did not occur in *Lyz2*$^{Cre/+}$.*Egr2*$^{fl/fl}$ mice and indeed, the alveolar macrophage compartment remained significantly reduced in *Lyz2*$^{Cre/+}$.*Egr2*$^{fl/fl}$ mice compared with *Egr2*$^{fl/fl}$ littermates even after 6 weeks (**Figure 8A-C**), suggesting EGR2 is indispensable for the repopulation of the alveolar macrophage niche following bleomycin-induced injury. The lack of repopulation in *Lyz2*$^{Cre/+}$.*Egr2*$^{fl/fl}$ mice did not appear to reflect an inability of *Egr2*-deficient macrophages to proliferate, as the proportion of Ki67^{+} proliferating cells was equivalent across both strains (**Figure 8D**). Equally, this also did not reflect a lack of chemoattractants in the airways to recruit monocyte-derived cells, as both CCL2 and CCL7 were actually elevated in *Lyz2*$^{Cre/+}$.*Egr2*$^{fl/fl}$ mice compared with control littermates (**Figure 8E**). Similarly, GM-CSF levels were elevated in the BAL fluid of *Lyz2*$^{Cre/+}$.*Egr2*$^{fl/fl}$ mice, ruling out the possibility that lack of appropriate growth factors is responsible for defective alveolar macrophage differentiation in the absence of EGR2 (**Figure 8E**). Instead, these data suggested that *Egr2* deficiency led to an intrinsic inability of bone marrow-derived cells to repopulate the macrophage niche. To test this directly, we crossed *Cx3cr1*$^{Cre\text{-}ERT2/+}$.*Rosa26*$^{LSL\text{-}RFP/+}$ mice with *Egr2*$^{fl/fl}$ mice to allow for temporal RFP labelling of CX3CR1-expressing cells and *Egr2* deficiency in the same animal. We administered tamoxifen during the period of alveolar macrophage reconstitution (d16 to d21) and assessed the presence of RFP-labelled cells amongst alveolar macrophages. Although labelling efficiencies were low, most likely reflecting the short period of tamoxifen induction and the dynamic nature of macrophage repopulation, compared with tamoxifen-treated controls (*Cx3cr1*$^{Cre\text{-}ERT2/+}$.*Rosa26*$^{LSL\text{-}RFP/+}$.*Egr2*$^{+/+}$ or *Cx3cr1*$^{Cre\text{-}ERT2/+}$.*Rosa26*$^{LSL\text{-}RFP/+}$.*Egr2*$^{fl/+}$ mice), we found a marked reduction in the frequency of RFP^{+} alveolar macrophages in the BAL of tamoxifen treated *Cx3cr1*$^{Cre\text{-}ERT2/+}$.*Rosa26*$^{LSL\text{-}RFP/+}$.*Egr2*$^{fl/fl}$ mice during lung repair (**Figure 8F**), demonstrating that EGR2 controls the post-injury repopulation of the alveolar macrophage compartment by CX3CR1^{+} cells.

To determine the consequence of the failure of *Egr2*-deficient cells to reconstitute the alveolar niche, we assessed the fibrotic response and subsequent repair processes in *Lyz2*$^{Cre/+}$.*Egr2*$^{fl/fl}$ mice. Notably,

we did not detect differences in the degree of fibrosis or expression of key genes associated with fibrosis, including *Col3a1* and *Pdgfrb* between *Lyz2*$^{Cre/+}$.*Egr2*$^{fl/fl}$ mice and their *Egr2*$^{fl/fl}$ littermate controls at day 21, a time considered 'peak' fibrosis (**Figure 8H, Supplementary Figure 10A, B**). However, analysis at 6 weeks post bleomycin showed that whereas the *Egr2*$^{fl/fl}$ mice had largely repaired their lungs, *Lyz2*$^{Cre/+}$.*Egr2*$^{fl/fl}$ mice had defective repair evidenced by persistent fibrosis and architectural damage (**Figure 8G, H, Supplementary Figure 10A**). This was paralleled by elevated numbers of macrophages in the lung parenchyma (**Figure 8I, Supplementary Figure 10A**) and parenchymal macrophage persistence correlated with the degree of fibrosis (**Supplementary Figure 10C**). Furthermore, homeostasis failed to be restored in the airways. Flow cytometric analysis of BAL fluid revealed that CD45^{+} leukocytes comprised only 10% of all events in *Lyz2*$^{Cre/+}$.*Egr2*$^{fl/fl}$ mice compared with 60% in their *Egr2*$^{fl/fl}$ littermates (**Figure 8J**). The vast majority of the CD45^{-} fraction failed to express signature markers for cells of epithelial, endothelial or fibroblast origin, suggesting this may represent cellular debris, which could also be found amongst lung digests (**Supplementary Figure 11A-C**). This was paralleled by elevated BAL fluid protein levels and turbidity in the *Lyz2*$^{Cre/+}$.*Egr2*$^{fl/fl}$ mice compared with controls, suggesting that the inability to replenish the alveolar macrophage niche following injury was associated with the development of alveolar proteinosis (**Figure 8K**). Thus, loss of EGR2-dependent, monocyte-derived alveolar macrophages leads to defective tissue repair, persistent cellular damage and failed restoration of lung homeostasis.

Discussion

Given the multifaceted role of macrophages in tissue homeostasis, inflammation and tissue repair, as well as many chronic pathologies, understanding the environmental signals and the downstream molecular pathways that govern macrophage differentiation is a key objective in the field of immunology. Here, we identify the transcription factor EGR2 as a selective and indispensable part of the tissue-specific differentiation of lung alveolar macrophages.

Our transcriptomic analysis identified EGR2 as a feature of murine lung alveolar macrophages, a finding consistent with previous studies using bulk transcriptomic analysis *(5, 12)* and a recent study using a similar scRNA-seq based approach *(47)*. Our finding that EGR2 appears to represent an evolutionarily conserved transcriptional regulator is also consistent with previous studies *(37, 48)*. While EGR2 has been implicated in controlling monocyte to macrophage differentiation in the past, these studies have often reached discrepant conclusions *(20, 21)*. This could reflect the fact that most studies examining the role of EGR2 in monocyte-macrophage differentiation have employed *in vitro* culture systems due to the postnatal lethality of global *Egr2*-deficient mice *(22, 23)*. By generating *Lyz2*^{Cre}.*Egr2*$^{fl/fl}$ and *Fcgr1*^{iCre}.*Egr2*$^{fl/fl}$ mice, we circumvented this lethality and demonstrated that EGR2 controls a large proportion of the alveolar macrophage 'signature'. This is consistent with recent epigenetic analysis showing an overrepresentation of EGR motifs in the genes defining alveolar macrophages *(49)*. Importantly, although previous work has suggested that there is redundancy between EGR family members, specifically EGR1 and EGR2, we found *Egr1* expression was unaffected by EGR2 deficiency and was unable to rescue alveolar macrophage differentiation.

Notably, if assessed simply on the basis of their CD11c^{hi}CD11b^{lo} profile, the absolute number of alveolar macrophages was equivalent between adult *Egr2*$^{fl/fl}$ and *Lyz2*^{Cre}.*Egr2*$^{fl/fl}$ mice. This could explain why a recent study using an independent strain of *Lyz2*^{Cre}.*Egr2*$^{fl/fl}$ mice concluded that EGR2 is dispensable for macrophage differentiation *(37)*. Alternatively, this could reflect that the majority of their studies involved *in vitro* generated, CSF1-dependent macrophages. Indeed, we found that *Egr2*-deficient monocytes matured into macrophages equally well when cultured *in vitro* with CSF-1. However, in our hands, CSF-1 led to poor upregulation of EGR2 in maturing macrophages *in vitro*. Instead, we identified GM-CSF as a potent inducer of EGR2 expression, a finding consistent with the dependence of alveolar macrophages on alveolar epithelial cell-derived GM-CSF for their development and survival *(7, 8)*. Importantly, deficiencies in *Lyz2*^{Cre}.*Egr2*$^{fl/fl}$ mice did not reflect consistent differences in the expression of GM-CSF signalling molecules. EGR2 is often referred to as a feature of alternative macrophage activation on the basis that IL-4 can drive EGR2 upregulation *in vitro* in a STAT6-dependent manner *(36, 37)*. However, we ruled out a role for IL-4 in EGR2 regulation in alveolar macrophages. Thus, the IL-4–IL-4R

axis is sufficient, but not necessary, for inducing EGR2 expression *in vivo*. TGF-β also induced EGR2 and we confirmed that TGF-βR signalling is indispensable for the development of alveolar macrophages *(9)*. If and how GM-CSF and TGF-β cooperate to promote alveolar macrophage differentiation is incompletely understood, however they both induce expression of PPAR-γ *(8, 9)* and *Pparg*-deficient alveolar macrophages expressed reduced EGR2 *(8)*, suggesting EGR2 lies downstream of PPAR-γ. Whether an initial TGFβ signal is needed to induce EGR2 during alveolar macrophage development or if continual TGFβR signalling is needed to maintain EGR2 remains to be determined and will require new transgenic systems to allow inducible deletion of TGFβR. Notably, while genetic ablation of *Pparg, Csf2rb* or *Tgfbr2* leads to defects in the development and self-maintenance of alveolar macrophages, this was not replicated by *Egr2* deficiency. Thus, the EGR2-dependent programme appears to represent a discrete part of alveolar macrophage differentiation. Consistent with this, mice with myeloid or macrophage deletion of *Egr2* did not develop spontaneous alveolar proteinosis, suggesting EGR2 is redundant for regulation of surfactant. However, *Egr2*-deficient mice displayed functional deficiencies in the ability to control low dose *S. pneumoniae* infection. Although we cannot rule out the possibility that this reflects differences in the killing capacity of *Egr2*-deficient alveolar macrophages, genes encoding e.g. reactive oxygen and nitrogen species were unaffected by *Egr2* deficiency. Instead, genes encoding key pathogen recognition receptors and opsonins, were significantly downregulated in the absence of EGR2. These included MARCO and the complement component C3, both of which have been shown to be crucial for the effective elimination of *S. pneumoniae (35, 50)*. Indeed, opsonisation is a critical factor in optimizing bacterial clearance by alveolar macrophages in health and disease *(51).* Thus, it is clear that EGR2-dependent differentiation equips alveolar macrophages with the machinery to recognise and engulf pneumococci, and this may explain the recurrent pneumonias in individuals with mutations in *EGR2 (22)*. In future work, it will be important to determine if this extends to other respiratory pathogens. Moreover, given that MARCO appears to define a discrete subset of CXCL2-expressing alveolar macrophages with elevated pro-inflammatory features in the context of fungal infection *(52)*, it will be of interest to determine if all alveolar macrophages are equal in their ability to eliminate *S. pneumoniae* or if an analogous $CXCL2^+$ subset with superior anti-bacterial capacity exists in this context.

Loss of alveolar macrophages is a common feature of lung inflammation or injury. Consistent with previous work *(42, 53)*, we found that the principal mechanism of macrophage replenishment was through recruitment of BM-derived cells which mature into bona fide alveolar macrophages with time. Using *Cx3cr1*-based genetic fate mapping, we also showed that $CX3CR1^+MHCII^+$ cells with a hybrid phenotype could be found in the airways during the fibrotic phase of injury, suggesting that monocyte-derived macrophages that accumulate in the lung parenchyma following injury may replenish the alveolar

504 macrophage niche. Although we cannot rule out that monocytes, including Ly6C^{low} monocytes *(54)*, enter
505 the airways during this phase to give rise to alveolar macrophages directly, the phenotype of the RFP^{+}
506 transitional cells was more aligned with the phenotype of elicited, monocyte-derived macrophages in the
507 parenchyma, including high levels of MHCII. Importantly, repopulation of the alveolar macrophage
508 compartment was dependent on EGR2, with constitutive deletion of EGR2 severely blunting the
509 engraftment of monocyte-derived cells into the alveolar macrophage niche. This contrasts with initial
510 population of the developing alveolar niche by foetal liver-derived monocytes, where *Egr2* deficiency does
511 not affect the development of alveolar macrophages. This could indicate differential dependence of
512 developmentally distinct monocytes on EGR2, or the presence of compensatory pathways during
513 development that are not present during repopulation and further work is required to fully understand this.

514 Interestingly, although previous work has suggested that monocyte-derived alveolar macrophages
515 are key pro-fibrotic cells *(42, 53)*, fibrosis appeared to develop normally in *Egr2*-deficient mice, despite the
516 near absence of monocyte-derived alveolar macrophages. The reason for the discrepancy in our findings
517 and those of Misharin *et al. (42)* is unclear, but it could reflect differences in the systems used. For instance,
518 the Misharin study exploited the dependence of alveolar macrophages on Caspase-8 to impede monocyte
519 differentiation into alveolar macrophages by using *Lyz2*^{Cre}.*Casp8*$^{fl/fl}$ and *Itgax*^{Cre}.*Casp8*$^{fl/fl}$ mice. However,
520 deletion of Caspase-8 also affects the ability of interstitial macrophages to repopulate following depletion,
521 meaning that *Casp8* deficiency may have wider effects on lung macrophage behaviour than disrupting the
522 differentiation of monocyte-derived alveolar macrophages. In contrast, EGR2 expression is restricted to
523 alveolar macrophages and deletion does not affect the reconstitution of the interstitial macrophage
524 compartment. The location of interstitial macrophages in the parenchyma adjacent to fibroblasts and their
525 production of the fibroblast mitogen PDGF-aa, suggests that interstitial macrophages are likely to be key
526 to the fibrotic process *(43)*. Indeed, depletion of interstitial macrophages using *Cx3cr1*$^{Cre\text{-}ERT2}$.*Rosa26*$^{LSL\text{-}}$
527 ^{DTA} mice reduces lung fibrosis *(43)*, although as we show here, this will also target CX3CR1^{+} cells destined
528 to become monocyte-derived alveolar macrophages. Nevertheless, our data show a clear role for monocyte-
529 derived macrophages in tissue repair processes, as *Lyz2*^{Cre}.*Egr2*$^{fl/fl}$ mice failed to repair the lung after injury,
530 a finding consistent with an older study using non-specific, clodronate-mediated depletion of lung
531 macrophages *(55)* and a recent study implicating ApoE-producing, monocyte-derived alveolar
532 macrophages in lung fibrosis resolution *(56)*. These results may help explain the development of restrictive
533 pulmonary disease in individuals with mutations in *EGR2 (22)*.

534 In summary, our results demonstrate that EGR2 is an evolutionarily conserved transcriptional
535 regulator of alveolar macrophage differentiation, loss of which leads to major phenotypic, transcriptional
536 and functional deficiencies. By identifying EGR2 as a transcriptional regulator, we have begun to dissect

how common factors such as GM-CSF and TGFβ confer specificity during macrophage differentiation. Our work reveals how distinct molecular modules appear to control the homeostatic versus immune protective functions of alveolar macrophages, which may be beneficial to the host by allowing these functions to be controlled independently. Importantly, given that recent studies using human systems have proposed that alveolar macrophage maintenance in humans requires monocyte input *(57, 58)*, EGR2 may play a particularly important role in alveolar macrophage differentiation in man. Thus, further work is required to fully understand the molecular pathways downstream of EGR2 and whether this is conserved between mouse and humans, and if EGR2 plays distinct roles in different pathological settings.

Materials and Methods

Study Design

We performed phenotypic, transcriptomic and functional analysis of alveolar macrophages in the context of *Egr2* deficiency to assess the features controlled by this transcription factor. Fate mapping techniques were used to assess the macrophage dynamics during bleomycin-induced injury and to test the cell intrinsic effects of *Egr2* deficiency. Infection with *Streptococcus pneumoniae* was used to assess the immune protective features of alveolar macrophages. All imaging and associated analysis was blinded. Experimental replicate details are provided in figure legends.

Experimental Animals

Mice were bred and maintained in SPF facilities at the University of Edinburgh or University of Glasgow, UK. All experimental mice were age matched and both sexes were used throughout the study. The mice used in each experiment is documented in the appropriate figure legend. Experiments performed at UK establishments were permitted under license by the UK Home Office and were approved by the University of Edinburgh Animal Welfare and Ethical Review Body. Genotyping was performed by Transnetyx using real-time PCR. Mouse strains are detailed in **Table S2**.

Human cells. BAL fluid was obtained from patients attending the Edinburgh Lung Fibrosis Clinic. Ethical permission was granted from the NHS Lothian Research ethics board (LREC 07/S1102/20 06/S0703/53). BAL fluid cells were stained for flow cytometric analysis with antibodies listed in **Table S3**.

Tamoxifen-based fate mapping. For induction of Cre activity in *Cx3cr1*$^{\text{Cre-ERT2/+}}$ mice, tamoxifen was dissolved in sesame oil overnight at 50mg/ml in a glass vial and administered by oral gavage at 5mg per day for five consecutive days. In bleomycin experiments, tamoxifen was administered from d16 post bleomycin administration for 5 days. Fresh tamoxifen was prepared for each experiment.

Bleomycin lung injury. Bleomycin sulphate (Cayman chemicals) was prepared by first dissolving in sterile DMSO (Sigma) and further in sterile PBS at 0.66mg/ml. 8-12-week-old *Lyz2*$^{\text{Cre}}$.*Egr2*$^{\text{fl/fl}}$ and *Egr2*$^{\text{fl/fl}}$ littermate controls were anaesthetised with isofluorane and administered 50µl bleomycin (33µg) or vehicle control (DMSO/PBS) by oropharyngeal aspiration.

Streptococcus pneumoniae infection. *Lyz2*$^{\text{Cre/+}}$.*Egr2*$^{\text{fl/fl}}$ mice and *Egr2*$^{\text{fl/fl}}$ littermate control male mice (8–14-week-old) were anaesthetised ketamine/medetomidine and inoculated intratracheally with 50µl of PBS containing 10^4 CFU *S. pneumoniae* (capsular type 2 strain D39). 100µl of inoculum was plated on blood agar to determine exact dose. Mice were culled 14 h later and BAL fluid collected by lavage performed using sterile PBS. 100µl of lavage fluid was cultured for bacterial growth for 24 h. The remaining lavage fluid was centrifuged at 400g for 5 mins and the resulting cells counted and prepared for flow cytometric analysis.

BM chimeric mice. To generate WT:*Lyz2*$^{\text{Cre}}$.*Egr2*$^{\text{fl/fl}}$ mixed chimeras, CD45.1^{+}CD45.2^{+} WT mice were lethally irradiated with two doses of 5 Gy 1 hour apart before being reconstituted immediately WT (CD45.1^{+})

and *Lyz2*$^{Cre/+}$.*Egr2*$^{fl/fl}$ or *Egr2*$^{fl/fl}$ (CD45.2^{+}) bone marrow at a ratio of 1:1.Chimerism was assessed at 8 weeks after reconstitution.

Processing of tissues. Mice were sacrificed by overdose with sodium pentobarbitone followed by exsanguination. Mice were then gently perfused with PBS through the heart. In lung injury/fibrosis experiments, the right lobe was tied off, excised and stored in RPMI with 10% FCS on ice before being prepared for enzymatic digestion (see below). The left lung lobe was inflated with 600µl 4% PFA through an intra-tracheal canula. The trachea was tied off with thread and the lung and heart carefully excised and stored in 4% PFA overnight. Fixed lung tissue was moved to 70% ethanol before being processed for histological assessment. Right lung lobes were chopped finely and digested in pre-warmed RPMI1640 with 'collagenase cocktail' (0.625mg ml^{-1} collagenase D (Roche), 0.425mg ml^{-1} collagenase V (Sigma-Aldrich), 1mg ml^{-1} Dispase (ThermoFisher), and 30 U ml^{-1} DNase (Roche Diagnostics GmbH)) for 25 minutes in a shaking incubator at 37°C before being passed through a 100µm strainer followed by centrifugation at 300g for 5 mins. Erythrocytes were lysed using Red Blood Cell Lysing Buffer Hybri-Max (Sigma-Aldrich) for 2mins at room temperature, washed in FACS buffer (2% FCS/2mM EDTA/PBS) and resuspended in 5mls of FACS buffer, counted and kept on ice until staining for flow cytometry. In some experiments BAL fluid was obtained by lavaging the lungs with 0.8ml DPBS/2mM EDTA via an intra-tracheal catheter. This was repeated three times, with the first wash kept separate for analysis of BAL cytokines, turbidity and protein concentration. To obtain splenic leukocytes, spleens were chopped and digested in HBSS with 1mg/ml collagenase D for 45 mins in a shaking incubator at 37°C before being passed through a 100µm strainer followed by centrifugation at 400g for 5 mins. Erythrocytes were lysed as above. To obtain liver leukocytes, livers were perfused through the inferior vena cava with sterile PBS and liver tissue excised. Livers were then chopped finely and digested in pre-warmed collagenase 'cocktail' (5ml/liver) for 30 minutes in a shaking incubator at 37°C before being passed through an 100µm filter. Cells were washed twice in 50ml ice cold RPMI followed by centrifugation at 300g for 5 mins *(59)*. Supernatants were discarded and erythrocytes were lysed. Epidermal and dermal leukocytes were isolated as described previously *(60).* Colonic and adipose tissue leukocytes were isolated as described previously *(61-63)*. To obtain peritoneal leukocytes, the peritoneal cavity was lavaged with RPMI containing 2mM EDTA and 10mM HEPES (both ThermoFisher) as described previously *(64)*. Cells were resuspended in FACS buffer, counted and kept on ice until staining for flow cytometry.

Flow cytometry. For analysis of unfixed cells, cells were first incubated with 0.025 µg anti-CD16/32 (2.4G2; Biolegend) for 10mins on ice to block Fc receptors and then stained with a combination of the antibodies detailed in **Table S3**. Where appropriate, cells were subsequently stained with streptavidin-conjugated BV650 (Biolegend). Dead cells were excluded using DAPI or 7-AAD (Biolegend) added 2mins before acquisition. When assessing intracellular markers, cells were first washed in PBS and then incubated with Zombie NIR fixable viability dye (Biolegend) for 10mins at room temperature protected from light before following the approach detailed above. Following the final wash step, cells were subsequently fixed and permeabilized using FoxP3/Transcription Factor Staining Buffer Set (eBioscience), and intracellular staining performed using antibodies detailed in **Table** S**3**. Samples were acquired using a FACS LSRFortessa or AriaII using FACSDiva software (BD) and analyzed with FlowJo software (version 9 or 10; Tree Star). Analysis was performed on single live cells determined using forward scatter height (FCS-H) versus area (FSC-A) and negativity for viability dyes. mRNA was detected by flow cytometry using

PrimeFlow technology (ThermoFisher) using probes against Spp1 (AF647) according to the manufacturer's guidelines. For staining controls in PrimeFlow analysis, the Target Probe Hybridization step was omitted with all other steps identical to samples.

BAL fluid analysis. The first BAL wash was centrifuged at 400g for 5mins and supernatant removed and stored at -80ºC until analysis. Total protein concentrations in BAL fluid were measured by BCA Protein Assay according to the manufacturer's instructions (ThermoFisher). Turbidity was determined following gentle mixing by diluting 25ul of sample with 75ul DPBS and measuring the optical density of 600nm and multiplying by the dilution factor. BAL cytokines were measured using 50ul undiluted sample and the Cytokine & Chemokine 26-Plex ProcartaPlex (Panel 1) assay according to manufacturer's guidelines (ThermoFisher).

Lung histology. Formalin-inflated lungs were fixed overnight in 4% buffered formalin and stored in 70% ethanol. Paraffin-embedded sections of mouse lungs were stained with Masson's trichome as per the manufacturer's guidelines.

***Statistics*.** Statistics were performed using Prism 7 (GraphPad Software). The statistical test used in each experiment is detailed in the relevant figure legend.

Details of transcriptional analysis and imaging can be found in the Supplementary Materials and Methods.

Acknowledgements. We are grateful to Prof. Ping Wang and Dr. Su-Ling Li, QMUL, London for the kind gift of the *Egr2*-floxed strain and to Prof. Rick Maziels, University of Glasgow for the provision of *Il4ra*-deficient mice. Flow cytometry data were generated with support from the QMRI Flow Cytometry and Cell Sorting Facility, University of Edinburgh. mRNA sequencing was performed by Edinburgh Genomics, The University of Edinburgh. Edinburgh Genomics is partly supported through core grants from NERC (R8/H10/56), MRC (MR/K001744/1) and BBSRC (BB/J004243/1). Genewiz performed the bulk RNA-seq analysis. We would like to thank Beth Henderson for technical expertise in setting up 10X sequencing; Dr. Jordan Portman for initial processing of the scRNAseq raw data; the ShIELD (Sheffield, Edinburgh, Newcastle and Birmingham) consortium for access to bacterial stocks; and Dr. Brian McHugh and Dr Manuel Sánchez García for help and advice on bacterial studies. We would also like to thank the Core Services and Advanced Technologies at the Cancer Research UK Beatson Institute, with particular thanks to the Beatson Advanced Imaging Resource (BAIR). Finally, we would like to thank the Bioresearch and Veterinary Services at the University of Edinburgh for husbandry of our mice and other technical assistance. Servier Medical Art was used for the generation of some of the graphics.

Funding. This research was funded by a Sir Henry Dale Fellowship jointly funded by the Wellcome Trust and the Royal Society [Grant number 206234/Z/17/Z to C.C.B]. CGH is supported by a University of Edinburgh Chancellor's Fellowship and CGH and RC are supported by Worldwide Cancer Research. The *Lyz2*^{Cre}.*Egr2*$^{fl/fl}$ line was originally generated with funding from the Medical Research Council UK (MR/L008076/1 to S.J.J). GRJ is funded by a Wellcome Trust Clinical Career Development Fellowship (220725/Z/20/Z). SRW is funded by a Wellcome Trust Senior Clinical Fellowship (209220). PTKS received funding from the MRC (MR/N024524/1). FF and LMC are funded by Cancer Research UK core funding (A23983 & A31287), and Breast Cancer Now (2019DecPR1424). This research was funded in whole or in part by The Wellcome Trust [Grant number 206234/Z/17/Z], a cOAlition S organization. The author will make the Author Accepted Manuscript (AAM) version available under a CC BY public copyright license.

Author Contributions. J. McC. performed experiments, analysed the data and edited the manuscript. P.M.K. Performed scRNA-seq analysis. F.F. Designed and performed immunofluorescence analysis of lung tissue. W. T'J. Performed experiments, analysed data and edited the manuscript. L. M. H. & C.M.M performed experiments and analysed the data. R. C. and C. G. H provided bioinformatic analysis of ImmGen data. A.S.M. provided advice on and help with the execution of fibrosis experiments. A. H. performed analysis. D.H. advised and helped with the execution of infection experiments. G.R.J. performed histological analysis of lung sections. S.J.J. generated the *Lyz2*^{Cre}.*Egr2*$^{fl/fl}$ mice. N. H. provided access to human bronchoalveolar samples. S.H. and B.M. generated and provided the *Fcgr1*^{iCre} mice. S.R.W. advised on the design of fibrosis experiments and provided reagents for infection experiments. D.D. advised on the design and execution of infection experiments. P.T.K.S. advised and provided infrastructure to perform scRNA-seq analysis. L.M.C. supervised F.F., advised and provided infrastructure and reagents to perform multi-parameter immunofluorescence analysis. C.C.B. conceived and performed experiments, analysed and interpreted the data, wrote the manuscript, obtained funding and supervised the project.

Competing Interests. The authors declare no competing interests.

Data and materials availability. All data needed to evaluate the conclusions in the paper are present in the paper or the Supplementary Materials, and RNA-seq data have been deposited in National Center for Biotechnology Information Gene Expression Omnibus public database (www.ncbi.nlm. nih.gov/geo/). Population-level RNA-seq (accession code: GSE182044) and scRNA-seq (accession code: GSE181894). *Fcgr1*^{iCre} mice are available from Prof. Bernard Malissen under a material transfer agreement with the Centre d'Immunologie de Marseille-Luminy, Aix Marseille Université**.** Further information and requests for resources and reagents should be directed to and will be fulfilled by the Lead Contact, Calum Bain (calum.bain@ed.ac.uk).

Supplementary materials:

Supplementary Methods

Figure S1: Gating strategy for and cluster annotation of scRNA-seq data (associated with Figure 1).
Figure S2: Validation of EGR2 expression by mouse and human alveolar macrophages (associated with Figure 2).
Figure S3: Effects of *Egr2* deficiency on macrophages in brain, spleen and adipose tissue (associated with Figure 2).
Figure S4: Gating strategy for alveolar macrophage purification and representative purity (associated with Figure 3).
Figure S5: Analysis of alveolar macrophage motility and morphodynamics (associated with Figure 3).
Figure S6: Analysis of *Fcgr1*$^{iCre/+}$.*Egr2*$^{fl/fl}$ and *Il4ra*$^{-/-}$ mice (associated with Figure 4 & 5).
Figure S7: EGR2 expression in context of *Strepococcus pneumoniae* infection (associated with Figure 4).
Figure S8: Validating the use of the *Cx3cr1*$^{Cre\text{-}ERT2/+}$.*Rosa26*$^{LSL\text{-}RFP/+}$ fate mapping model (associated with Figure 7).
Figure S9: Effects of *Egr2* deficiency on parenchymal myeloid cells during bleomycin induced fibrosis (associated with Figure 8).
Figure S10: Assessment of the effects of *Egr2* deficiency on lung injury and fibrosis (associated with Figure 8).
Figure S11: Phenotypic characterisation of the airway and parenchymal CD45^{-} fraction during resolution of bleomycin induced lung injury (associated with Figure 8).

Table S1: Gene ontology analysis of differentially expressed genes between alveolar macrophages from *Egr2*$^{fl/fl}$ and *Lyz2*$^{Cre/+}$.*Egr2* mice (relates to Figure 3).
Table S2: List of mouse strains
Table S3: List of antibodies
Table S4: List of primers

Data file S1: Cluster defining genes in scRNA-seq (relates to Figure 1).
Data file S2: Differentially expressed genes between alveolar macrophages from *Egr2*$^{fl/fl}$ and *Lyz2*$^{Cre/+}$.*Egr2* mice (relates to Figure 3).
Data file S3. *Ex vivo* imaging of Live Precision cut Lung Slices

Data file S4. *Ex vivo* imaging of Live Precision cut Lung Slices (zoom).
Data file S5. Raw data file (Excel file).

References.

1. P. P. Ogger, A. J. Byrne, Macrophage metabolic reprogramming during chronic lung disease, *Mucosal Immunol* **14**, 282–295 (2021).

2. P. Bost, A. Giladi, Y. Liu, Y. Bendjelal, G. Xu, E. David, R. Blecher-Gonen, M. Cohen, C. Medaglia, H. Li, A. Deczkowska, S. Zhang, B. Schwikowski, Z. Zhang, I. Amit, Host-Viral Infection Maps Reveal Signatures of Severe COVID-19 Patients, *Cell* **181**, 1475–1488.e12 (2020).

3. M. Liao, Y. Liu, J. Yuan, Y. Wen, G. Xu, J. Zhao, L. Cheng, J. Li, X. Wang, F. Wang, L. Liu, I. Amit, S. Zhang, Z. Zhang, Single-cell landscape of bronchoalveolar immune cells in patients with COVID-19, *Nat. Med.* **26**, 842–844 (2020).

4. M. Merad, J. C. Martin, Pathological inflammation in patients with COVID-19: a key role for monocytes and macrophages, *Nature reviews* **20**, 355–362 (2020).

5. E. Mass, I. Ballesteros, M. Farlik, F. Halbritter, P. Günther, L. Crozet, C. E. Jacome-Galarza, K. Händler, J. Klughammer, Y. Kobayashi, E. Gomez Perdiguero, J. L. Schultze, M. Beyer, C. Bock, F. Geissmann, Specification of tissue-resident macrophages during organogenesis, *Science (New York, N.Y* **353** (2016), doi:10.1126/science.aaf4238.

6. E. Gomez Perdiguero, K. Klapproth, C. Schulz, K. Busch, E. Azzoni, L. Crozet, H. Garner, C. Trouillet, M. F. de Bruijn, F. Geissmann, H.-R. Rodewald, Tissue-resident macrophages originate from yolk-sac-derived erythro-myeloid progenitors, *Nature* **518**, 547–551 (2015).

7. M. Guilliams, I. De Kleer, S. Henri, S. Post, L. Vanhoutte, S. De Prijck, K. Deswarte, B. Malissen, H. Hammad, B. N. Lambrecht, Alveolar macrophages develop from fetal monocytes that differentiate into long-lived cells in the first week of life via GM-CSF, *The Journal of experimental medicine* **210**, 1977–1992 (2013).

8. C. Schneider, S. P. Nobs, M. Kurrer, H. Rehrauer, C. Thiele, M. Kopf, Induction of the nuclear receptor PPAR-γ by the cytokine GM-CSF is critical for the differentiation of fetal monocytes into alveolar macrophages, *Nature immunology* **15**, 1026–1037 (2014).

9. X. Yu, A. Buttgereit, I. Lelios, S. G. Utz, D. Cansever, B. Becher, M. Greter, The Cytokine TGF-β Promotes the Development and Homeostasis of Alveolar Macrophages, *Immunity* **47**, 903–912.e4 (2017).

10. E. L. Gautier, A. Chow, R. Spanbroek, G. Marcelin, M. Greter, C. Jakubzick, M. Bogunovic, M. Leboeuf, N. Van Rooijen, A. J. Habenicht, M. Merad, G. J. Randolph, Systemic analysis of PPARgamma in mouse macrophage populations reveals marked diversity in expression with critical roles in resolution of inflammation and airway immunity, *J. Immunol.* **189**, 2614–2624 (2012).

11. K. Okreglicka, I. Iten, L. Pohlmeier, L. Onder, Q. Feng, M. Kurrer, B. Ludewig, P. Nielsen, C. Schneider, M. Kopf, PPARγ is essential for the development of bone marrow erythroblastic island macrophages and splenic red pulp macrophages, *The Journal of experimental medicine* **218** (2021), doi:10.1084/jem.20191314.

12. E. L. Gautier, T. Shay, J. Miller, M. Greter, C. Jakubzick, S. Ivanov, J. Helft, A. Chow, K. G. Elpek, S. Gordonov, A. R. Mazloom, A. Ma'ayan, W. J. Chua, T. H. Hansen, S. J. Turley, M. Merad, G. J. Randolph, Gene-expression profiles and transcriptional regulatory pathways that underlie the identity and diversity of mouse tissue macrophages, *Nature immunology* **13**, 1118–1128 (2012).

13. C. L. Scott, W. T'Jonck, L. Martens, H. Todorov, D. Sichien, B. Soen, J. Bonnardel, S. De Prijck, N. Vandamme, R. Cannoodt, W. Saelens, B. Vanneste, W. Toussaint, P. De Bleser, N. Takahashi, P. Vandenabeele, S. Henri, C. Pridans, D. A. Hume, B. N. Lambrecht, P. De Baetselier, S. W. F. Milling, J. A. Van Ginderachter, B. Malissen, G. Berx, A. Beschin, Y. Saeys, M. Guilliams, The Transcription Factor ZEB2 Is Required to Maintain the Tissue-Specific Identities of Macrophages, *Immunity* **49**, 312–325.e5 (2018).

14. A. D. Baker, A. Malur, B. P. Barna, S. Ghosh, M. S. Kavuru, A. G. Malur, M. J. Thomassen, Targeted PPAR{gamma} deficiency in alveolar macrophages disrupts surfactant catabolism, *J. Lipid Res.* **51**, 1325–1331 (2010).

15. D. W. Cain, E. G. O'Koren, M. J. Kan, M. Womble, G. D. Sempowski, K. Hopper, M. D. Gunn, G. Kelsoe, Identification of a tissue-specific, C/EBPβ-dependent pathway of differentiation for murine peritoneal macrophages, *J. Immunol.* **191**, 4665–4675 (2013).

16. R. Rauschmeier, C. Gustafsson, A. Reinhardt, N. A-Gonzalez, L. Tortola, D. Cansever, S. Subramanian, R. Taneja, M. J. Rossner, M. H. Sieweke, M. Greter, R. Månsson, M. Busslinger, T. Kreslavsky, Bhlhe40 and Bhlhe41 transcription factors regulate alveolar macrophage self-renewal and identity, *EMBO J.* **38**, e101233 (2019).

17. E. Madissoon, A. Wilbrey-Clark, R. J. Miragaia, K. Saeb-Parsy, K. T. Mahbubani, N. Georgakopoulos, P. Harding, K. Polanski, N. Huang, K. Nowicki-Osuch, R. C. Fitzgerald, K. W. Loudon, J. R. Ferdinand, M. R. Clatworthy, A. Tsingene, S. van Dongen, M. Dabrowska, M. Patel, M. J. T. Stubbington, S. A. Teichmann, O. Stegle, K. B. Meyer, scRNA-seq assessment of the human lung, spleen, and esophagus tissue stability after cold preservation, *Genome Biol.* **21**, 1 (2019).

18. S. A. MacParland, J. C. Liu, X.-Z. Ma, B. T. Innes, A. M. Bartczak, B. K. Gage, J. Manuel, N. Khuu, J. Echeverri, I. Linares, R. Gupta, M. L. Cheng, L. Y. Liu, D. Camat, S. W. Chung, R. K. Seliga, Z. Shao, E. Lee, S. Ogawa, M. Ogawa, M. D. Wilson, J. E. Fish, M. Selzner, A. Ghanekar, D. Grant, P. Greig, G. Sapisochin, N. Selzner, N. Winegarden, O. Adeyi, G. Keller, G. D. Bader, I. D. McGilvray, Single cell RNA sequencing of human liver reveals distinct intrahepatic macrophage populations, *Nat Commun* **9**, 4383 (2018).

19. N. Habib, I. Avraham-Davidi, A. Basu, T. Burks, K. Shekhar, M. Hofree, S. R. Choudhury, F. Aguet, E. Gelfand, K. Ardlie, D. A. Weitz, O. Rozenblatt-Rosen, F. Zhang, A. Regev, Massively parallel single-nucleus RNA-seq with DroNc-seq, *Nat Methods* **14**, 955–958 (2017).

20. P. Laslo, C. J. Spooner, A. Warmflash, D. W. Lancki, H.-J. Lee, R. Sciammas, B. N. Gantner, A. R. Dinner, H. Singh, Multilineage transcriptional priming and determination of alternate hematopoietic cell fates, *Cell* **126**, 755–766 (2006).

21. J. H. Carter, W. G. Tourtellotte, Early growth response transcriptional regulators are dispensable for macrophage differentiation, *J. Immunol.* **178**, 3038–3047 (2007).

22. P. J. Swiatek, T. Gridley, Perinatal lethality and defects in hindbrain development in mice homozygous for a targeted mutation of the zinc finger gene Krox20, *Genes Dev* **7**, 2071–2084 (1993).

812 23. P. Topilko, G. Levi, G. Merlo, S. Mantero, C. Desmarquet, G. Mancardi, P. Charnay, Differential
813 regulation of the zinc finger genes Krox-20 and Krox-24 (Egr-1) suggests antagonistic roles in Schwann
814 cells, *J Neurosci Res* **50**, 702–712 (1997).

815 24. B. E. Clausen, C. Burkhardt, W. Reith, R. Renkawitz, I. Förster, Conditional gene targeting in
816 macrophages and granulocytes using LysMcre mice. *Transgenic Res*. **8**(4):265-277 (1999).
817
818 25. E. Taillebourg, S. Buart, P. Charnay, Conditional, floxed allele of the Krox20 gene. *Genesis*.
819 **32**(2):112-113 (2002).
820

821 26. A. S. Neupane, M. Willson, A. K. Chojnacki, F. Vargas E Silva Castanheira, C. Morehouse, A.
822 Carestia, A. E. Keller, M. Peiseler, A. DiGiandomenico, M. M. Kelly, M. Amrein, C. Jenne, A.
823 Thanabalasuriar, P. Kubes, Patrolling Alveolar Macrophages Conceal Bacteria from the Immune System
824 to Maintain Homeostasis, *Cell* **183**, 110–125.e11 (2020).

825 27. K. Szigeti, W. Wiszniewski, G. M. Saifi, D. L. Sherman, N. Sule, A. M. Adesina, P. Mancias, S. C.
826 Papasozomenos, G. Miller, L. Keppen, D. Daentl, P. J. Brophy, J. R. Lupski, Functional, histopathologic
827 and natural history study of neuropathy associated with EGR2 mutations, *Neurogenetics* **8**, 257–262
828 (2007).

829 28. G. Dranoff, A. D. Crawford, M. Sadelain, B. Ream, A. Rashid, R. T. Bronson, G. R. Dickersin, C. J.
830 Bachurski, E. L. Mark, J. A. Whitsett, et al. Involvement of granulocyte-macrophage colony-stimulating
831 factor in pulmonary homeostasis. *Science* **29**;264(5159):713-6 (1994).
832
833 29. E. Stanley, G. J. Lieschke, D. Grail, D. Metcalf, G. Hodgson, J. A. Gall, D. W. Maher, J. Cebon, V.
834 Sinickas, A. R. Dunn. Granulocyte/macrophage colony-stimulating factor-deficient mice show no major
835 perturbation of hematopoiesis but develop a characteristic pulmonary pathology. *Proc. Natl. Acad. Sci.*
836 *U.S.A.* **7**;91(12):5592-6 (1994).
837
838 30. M. Martinez-Moczygemba, M. L. Doan, O. Elidemir, L. L. Fan, S. W. Cheung, J. T. Lei, J. P. Moore,
839 G. Tavana, L. R. Lewis, Y. Zhu, D. M. Muzny, R. A. Gibbs, D. P. Huston, Pulmonary alveolar
840 proteinosis caused by deletion of the GM-CSFRalpha gene in the X chromosome pseudoautosomal region
841 1, *The Journal of experimental medicine* **205**, 2711–2716 (2008).

842 31. T. Willinger, A. Rongvaux, H. Takizawa, G. D. Yancopoulos, D. M. Valenzuela, A. J. Murphy, W.
843 Auerbach, E. E. Eynon, S. Stevens, M. G. Manz, R. A. Flavell, Human IL-3/GM-CSF knock-in mice
844 support human alveolar macrophage development and human immune responses in the lung, *Proc. Natl.*
845 *Acad. Sci. U.S.A.* **108**, 2390–2395 (2011).

846 32. T. Suzuki, P. Arumugam, T. Sakagami, N. Lachmann, C. Chalk, A. Sallese, S. Abe, C. Trapnell, B.
847 Carey, T. Moritz, P. Malik, C. Lutzko, R. E. Wood, B. C. Trapnell, Pulmonary macrophage
848 transplantation therapy, *Nature* **514**, 450–454 (2014).

849 33. J. A. Preston, M. A. Bewley, H. M. Marriott, A. McGarry Houghton, M. Mohasin, J. Jubrail, L.
850 Morris, Y. L. Stephenson, S. Cross, D. R. Greaves, R. W. Craig, N. van Rooijen, C. D. Bingle, R. C.
851 Read, T. J. Mitchell, M. K. B. Whyte, S. D. Shapiro, D. H. Dockrell, Alveolar Macrophage Apoptosis-
852 associated Bacterial Killing Helps Prevent Murine Pneumonia, *Am. J. Respir. Crit. Care Med.* **200**, 84–97
853 (2019).

34. H. M. Marriott, M. Daigneault, A. A. R. Thompson, S. R. Walmsley, S. K. Gill, D. R. Witcher, V. J. Wroblewski, P. G. Hellewell, M. K. B. Whyte, D. H. Dockrell, A decoy receptor 3 analogue reduces localised defects in phagocyte function in pneumococcal pneumonia, *Thorax* **67**, 985–992 (2012).

35. M. Arredouani, Z. Yang, Y. Ning, G. Qin, R. Soininen, K. Tryggvason, L. Kobzik, The scavenger receptor MARCO is required for lung defense against pneumococcal pneumonia and inhaled particles, *The Journal of experimental medicine* **200**, 267–272 (2004).

36. T. Veremeyko, A. W. Y. Yung, D. C. Anthony, T. Strekalova, E. D. Ponomarev, Early Growth Response Gene-2 Is Essential for M1 and M2 Macrophage Activation and Plasticity by Modulation of the Transcription Factor CEBPβ, *Front Immunol* **9**, 2515 (2018).

37. B. Daniel, Z. Czimmerer, L. Halasz, P. Boto, Z. Kolostyak, S. Poliska, W. K. Berger, P. Tzerpos, G. Nagy, A. Horvath, G. Hajas, T. Cseh, A. Nagy, S. Sauer, J. Francois-Deleuze, I. Szatmari, A. Bacsi, L. Nagy, The transcription factor EGR2 is the molecular linchpin connecting STAT6 activation to the late, stable epigenomic program of alternative macrophage polarization, *Genes Dev* **34**, 1474–1492 (2020).

38. O. Butovsky, M. P. Jedrychowski, C. S. Moore, R. Cialic, A. J. Lanser, G. Gabriely, T. Koeglsperger, B. Dake, P. M. Wu, C. E. Doykan, Z. Fanek, L. Liu, Z. Chen, J. D. Rothstein, R. M. Ransohoff, S. P. Gygi, J. P. Antel, H. L. Weiner, Identification of a unique TGF-β-dependent molecular and functional signature in microglia, *Nat. Neurosci.* **17**, 131–143 (2014).

39. H. Lund, M. Pieber, R. Parsa, D. Grommisch, E. Ewing, L. Kular, J. Han, K. Zhu, J. Nijssen, E. Hedlund, M. Needhamsen, S. Ruhrmann, A. O. Guerreiro-Cacais, R. Berglund, M. J. Forteza, D. F. J. Ketelhuth, O. Butovsky, M. Jagodic, X.-M. Zhang, R. A. Harris, Fatal demyelinating disease is induced by monocyte-derived macrophages in the absence of TGF-β signaling, *Nature immunology* **19**, 1–7 (2018).

40. M. Guilliams, F. R. Svedberg, Does tissue imprinting restrict macrophage plasticity? *Nature immunology* **496**, 445 (2021).

41. R. Peng, S. Sridhar, G. Tyagi, J. E. Phillips, R. Garrido, P. Harris, L. Burns, L. Renteria, J. Woods, L. Chen, J. Allard, P. Ravindran, H. Bitter, Z. Liang, C. M. Hogaboam, C. Kitson, D. C. Budd, J. S. Fine, C. M. T. Bauer, C. S. Stevenson, Bleomycin induces molecular changes directly relevant to idiopathic pulmonary fibrosis: a model for "active" disease, *PLoS ONE* **8**, e59348 (2013).

42. A. V. Misharin, L. Morales-Nebreda, P. A. Reyfman, C. M. Cuda, J. M. Walter, A. C. McQuattie-Pimentel, C.-I. Chen, K. R. Anekalla, N. Joshi, K. J. N. Williams, H. Abdala-Valencia, T. J. Yacoub, M. Chi, S. Chiu, F. J. Gonzalez-Gonzalez, K. Gates, A. P. Lam, T. T. Nicholson, P. J. Homan, S. Soberanes, S. Dominguez, V. K. Morgan, R. Saber, A. Shaffer, M. Hinchcliff, S. A. Marshall, A. Bharat, S. Berdnikovs, S. M. Bhorade, E. T. Bartom, R. I. Morimoto, W. E. Balch, J. I. Sznajder, N. S. Chandel, G. M. Mutlu, M. Jain, C. J. Gottardi, B. D. Singer, K. M. Ridge, N. Bagheri, A. Shilatifard, G. R. S. Budinger, H. Perlman, Monocyte-derived alveolar macrophages drive lung fibrosis and persist in the lung over the life span, *The Journal of experimental medicine* **214**, 2387–2404 (2017).

43. D. Aran, A. P. Looney, L. Liu, E. Wu, V. Fong, A. Hsu, S. Chak, R. P. Naikawadi, P. J. Wolters, A. R. Abate, A. J. Butte, M. Bhattacharya, Reference-based analysis of lung single-cell sequencing reveals a transitional profibrotic macrophage, *Nature immunology* **20**, 163–172 (2019).

44. S. Yona, K.-W. Kim, Y. Wolf, A. Mildner, D. Varol, M. Breker, D. Strauss-Ayali, S. Viukov, M. Guilliams, A. Misharin, D. A. Hume, H. Perlman, B. Malissen, E. Zelzer, S. Jung, Fate mapping reveals

origins and dynamics of monocytes and tissue macrophages under homeostasis, *Immunity* **38**, 79–91 (2013).

45. T. Goldmann, P. Wieghofer, P. F. Müller, Y. Wolf, D. Varol, S. Yona, S. M. Brendecke, K. Kierdorf, O. Staszewski, M. Datta, T. Luedde, M. Heikenwalder, S. Jung, M. Prinz, A new type of microglia gene targeting shows TAK1 to be pivotal in CNS autoimmune inflammation, *Nat. Neurosci.* **16**, 1618–1626 (2013).

46. S. Chakarov, H. Y. Lim, L. Tan, S. Y. Lim, P. See, J. Lum, X.-M. Zhang, S. Foo, S. Nakamizo, K. Duan, W. T. Kong, R. Gentek, A. Balachander, D. Carbajo, C. Bleriot, B. Malleret, J. K. C. Tam, S. Baig, M. Shabeer, S.-A. E. S. Toh, A. Schlitzer, A. Larbi, T. Marichal, B. Malissen, J. Chen, M. Poidinger, K. Kabashima, M. Bajénoff, L. G. Ng, V. Angeli, F. Ginhoux, Two distinct interstitial macrophage populations coexist across tissues in specific subtissular niches, *Science (New York, N.Y* **363**, eaau0964 (2019).

47. E. Sajti, V. M. Link, Z. Ouyang, N. J. Spann, E. Westin, C. E. Romanoski, G. J. Fonseca, L. S. Prince, C. K. Glass, Transcriptomic and epigenetic mechanisms underlying myeloid diversity in the lung, *Nature immunology* **21**, 221–231 (2020).

48. S. Hirano, C. D. Anuradha, S. Kanno, Transcription of krox-20/egr-2 is upregulated after exposure to fibrous particles and adhesion in rat alveolar macrophages, *Am. J. Respir. Cell Mol. Biol.* **23**, 313–319 (2000).

49. Y. Lavin, D. Winter, R. Blecher-Gonen, E. David, H. Keren-Shaul, M. Merad, S. Jung, I. Amit, Tissue-resident macrophage enhancer landscapes are shaped by the local microenvironment, *Cell* **159**, 1312–1326 (2014).

50. J. S. Brown, T. Hussell, S. M. Gilliland, D. W. Holden, J. C. Paton, M. R. Ehrenstein, M. J. Walport, & M. Botto, The classical pathway is the dominant complement pathway required for innate immunity to Streptococcus pneumoniae infection in mice, *PNAS* ***99***(26), 16969–16974 (2002).

51. M. A. Bewley, R. C. Budd, E. Ryan, J. Cole, P. Collini, J. Marshall, U. Kolsum, G. Beech, R. D. Emes, I. Tcherniaeva, G. A. M. Berbers, S. R. Walmsley, G. Donaldson, J. A. Wedzicha, I. Kilty, W. Rumsey, Y. Sanchez, C. E. Brightling, L. E. Donnelly, P. J. Barnes, D. Singh, M. K. B. Whyte, D. H. Dockrell, COPDMAP, Opsonic Phagocytosis in Chronic Obstructive Pulmonary Disease Is Enhanced by Nrf2 Agonists, *Am. J. Respir. Crit. Care Med.* **198**, 739–750 (2018).

52. S. Xu-Vanpala, M. E. Deerhake, J. D. Wheaton, M. E. Parker, P. R. Juvvadi, N. MacIver, M. Ciofani, M. L. Shinohara, Functional heterogeneity of alveolar macrophage population based on expression of CXCL2, *Sci Immunol* **5** (2020), doi:10.1126/sciimmunol.aba7350.

53. N. Joshi, S. Watanabe, R. Verma, R. P. Jablonski, C.-I. Chen, P. Cheresh, N. S. Markov, P. A. Reyfman, A. C. McQuattie-Pimentel, L. Sichizya, Z. Lu, R. Piseaux-Aillon, D. Kirchenbuechler, A. S. Flozak, C. J. Gottardi, C. M. Cuda, H. Perlman, M. Jain, D. W. Kamp, G. R. S. Budinger, A. V. Misharin, A spatially restricted fibrotic niche in pulmonary fibrosis is sustained by M-CSF/M-CSFR signalling in monocyte-derived alveolar macrophages, *Eur. Respir. J.* **55**, 1900646 (2020).

54. T. Satoh, K. Nakagawa, F. Sugihara, R. Kuwahara, M. Ashihara, F. Yamane, Y. Minowa, K. Fukushima, I. Ebina, Y. Yoshioka, A. Kumanogoh, S. Akira, Identification of an atypical monocyte and committed progenitor involved in fibrosis, *Nature* **541**, 96–101 (2017).

936 55. M. A. Gibbons, A. C. MacKinnon, P. Ramachandran, K. Dhaliwal, R. Duffin, A. T. Phythian-Adams,
937 N. van Rooijen, C. Haslett, S. E. Howie, A. J. Simpson, N. Hirani, J. Gauldie, J. P. Iredale, T. Sethi, S. J.
938 Forbes, Ly6Chi monocytes direct alternatively activated profibrotic macrophage regulation of lung
939 fibrosis, *Am. J. Respir. Crit. Care Med.* **184**, 569–581 (2011).

940 56. H. Cui, D. Jiang, S. Banerjee, N. Xie, T. Kulkarni, R.-M. Liu, S. R. Duncan, G. Liu, Monocyte-
941 derived alveolar macrophage apolipoprotein E participates in pulmonary fibrosis resolution, *JCI Insight* **5**
942 (2020), doi:10.1172/jci.insight.134539.

943 57. A. J. Byrne, J. E. Powell, B. J. O'Sullivan, P. P. Ogger, A. Hoffland, J. Cook, K. L. Bonner, R. J.
944 Hewitt, S. Wolf, P. Ghai, S. A. Walker, S. W. Lukowski, P. L. Molyneaux, S. Saglani, D. C. Chambers,
945 T. M. Maher, C. M. Lloyd, Dynamics of human monocytes and airway macrophages during healthy aging
946 and after transplant, *The Journal of experimental medicine* **217** (2020), doi:10.1084/jem.20191236.

947 58. E. Evren, E. Ringqvist, K. P. Tripathi, N. Sleiers, I. C. Rives, A. Alisjahbana, Y. Gao, D. Sarhan, T.
948 Halle, C. Sorini, R. Lepzien, N. Marquardt, J. Michaëlsson, A. Smed-Sörensen, J. Botling, M. C. I.
949 Karlsson, E. J. Villablanca, T. Willinger, Distinct developmental pathways from blood monocytes
950 generate human lung macrophage diversity, *Immunity* **54**, 259–275.e7 (2021).

951 59. R. W. Lynch, C. A. Hawley, A. Pellicoro, C. C. Bain, J. P. Iredale, S. J. Jenkins, An efficient method
952 to isolate Kupffer cells eliminating endothelial cell contamination and selective bias, *Journal of leukocyte*
953 *biology* (2018), doi:10.1002/JLB.1TA0517-169R.

954 60. S. Tamoutounour, M. Guilliams, F. Montanana Sanchis, H. Liu, D. Terhorst, C. Malosse, E. Pollet, L.
955 Ardouin, H. Luche, C. Sanchez, M. Dalod, B. Malissen, S. Henri, Origins and functional specialization of
956 macrophages and of conventional and monocyte-derived dendritic cells in mouse skin, *Immunity* **39**, 925–
957 938 (2013).

958 61. C. L. Scott, C. C. Bain, A. M. Mowat, Isolation and Identification of Intestinal Myeloid Cells,
959 *Methods Mol. Biol.* **1559**, 223–239 (2017).

960 62. C. C. Bain, A. M. Mowat, CD200 receptor and macrophage function in the intestine, *Immunobiology*
961 (2011), doi:10.1016/j.imbio.2011.11.004.

962 63. M. S. Magalhaes, P. Smith, J. R. Portman, L. H. Jackson-Jones, C. C. Bain, P. Ramachandran, Z.
963 Michalidou, R. H. Stimson, M. R. Dweck, L. Denby, N. C. Henderson, S. J. Jenkins, C. Bénézech, Role
964 of Tim4 in the regulation of ABCA1+ adipose tissue macrophages and post-prandial cholesterol levels,
965 *Nat Commun* **12**, 4434–15 (2021).

966 64. C. C. Bain, S. J. Jenkins, Isolation and Identification of Murine Serous Cavity Macrophages, *Methods*
967 *Mol. Biol.* **1784**, 51–67 (2018).

968 65. K. J. Livak, T. D. Schmittgen, Analysis of relative gene expression data using real-time
969 quantitative PCR and the 2(-Delta Delta C(T)) Method, *Methods* **25**, 402–408 (2001).

970 66. R. Dobie, J. R. Wilson-Kanamori, B. E. P. Henderson, J. R. Smith, K. P. Matchett, J. R.
971 Portman, K. Wallenborg, S. Picelli, A. Zagórska, S. V. Pendem, T. E. Hudson, M. M. Wu, G. R.
972 Budas, D. G. Breckenridge, E. M. Harrison, D. J. Mole, S. J. Wigmore, P. Ramachandran, C. P.
973 Ponting, S. A. Teichmann, J. C. Marioni, N. C. Henderson, Single-Cell Transcriptomics

974 Uncovers Zonation of Function in the Mesenchyme during Liver Fibrosis, *Cell Rep* **29**, 1832–
975 1847.e8 (2019).

976 67. R. Satija, J. A. Farrell, D. Gennert, A. F. Schier, A. Regev, Spatial reconstruction of single-
977 cell gene expression data, *Nat. Biotechnol.* **33**, 495–502 (2015).

978 68. F. Fercoq, E. Remion, N. Vallarino-Lhermitte, J. Alonso, L. Raveendran, C. Nixon, J. Le
979 Quesne, L. M. Carlin, C. Martin, Microfilaria-dependent thoracic pathology associated with
980 eosinophilic and fibrotic polyps in filaria-infected rodents, *Parasit Vectors* **13**, 551 (2020).

981 69. P. Bankhead, M. B. Loughrey, J. A. Fernández, Y. Dombrowski, D. G. McArt, P. D. Dunne,
982 S. McQuaid, R. T. Gray, L. J. Murray, H. G. Coleman, J. A. James, M. Salto-Tellez, P. W.
983 Hamilton, QuPath: Open source software for digital pathology image analysis, *Sci Rep* **7**, 16878
984 (2017).

985 70. H. Luche, O. Weber, T. Nageswara Rao, C. Blum, H. J. Fehling. Faithful activation of an
986 extra-bright red fluorescent protein in "knock-in" Cre-reporter mice ideally suited for lineage
987 tracing studies. *Eur J Immunol*. **37**(1):43-53 (2002).
988
989

990
991
992

Figure 1

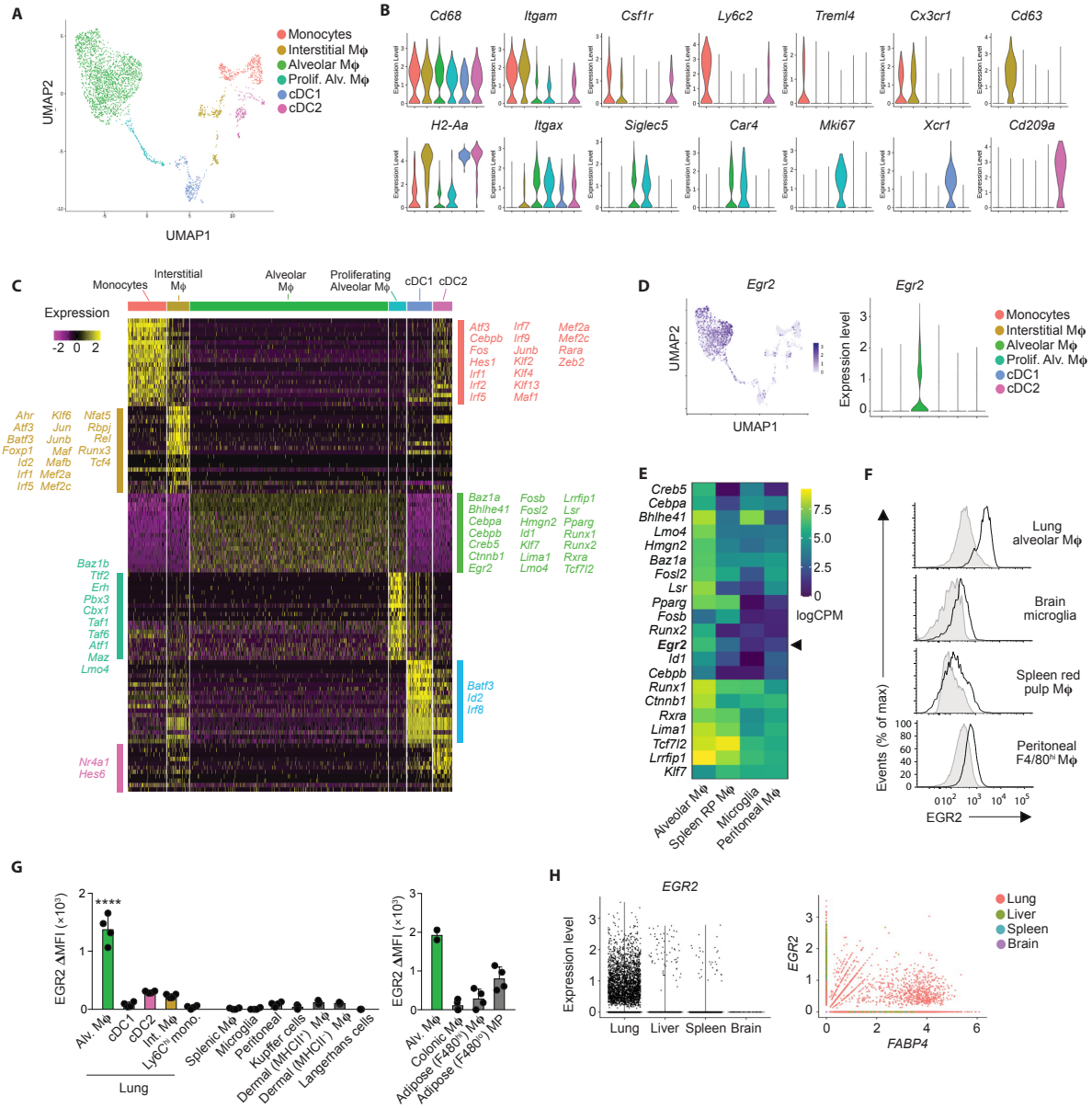

Figure 1. EGR2 expression is a selective property of alveolar macrophages

A. UMAP dimensionality reduction analysis of 3936 cells (non-granulocyte, myeloid cells) reveals six clusters of mononuclear phagocytes in murine lungs. Cells obtained from an individual *Rag1*$^{-/-}$ mouse.

B. Feature plots displaying expression of individual genes by clusters identified in **A.**

C. Heatmap showing the top 20 most differentially expressed genes by each cluster defined in **A**. and annotated to show upregulated transcription factors/regulators within each cluster.

D. Overlay UMAP plot and feature plot showing expression of *Egr2* by clusters identified in **A.**

E. Heatmap showing relative expression of selected transcription factors by lung alveolar macrophages, $CD102^+$ peritoneal macrophages, brain microglia and red pulp splenic macrophages as derived from the ImmGen consortium.

F. Representative expression of EGR2 by lung alveolar macrophages, $CD102^+$ peritoneal macrophages, brain microglia and red pulp splenic macrophages obtained from adult unmanipulated C57BL/6 mice. Shaded histograms represent isotype controls. Data are from one of three independent experiments.

G. Expression of EGR2 by the indicated macrophage and myeloid cell populations shown as relative MFI (MFI in *Egr2*$^{fl/fl}$ – MFI in *Lyz2*$^{Cre/+}$.*Egr2*$^{fl/fl}$ mice). Adipose & colonic macrophages shown on a separate graph due to measurements performed in an independent experiment with different flow cytometer settings. Repeat data for alveolar macrophages included as a reference. Data represent 3-4 mice (*left graph*) or 2-4 mice (right graph) per tissue. **** $p<0.0001$ (One-way ANOVA followed by Tukey's multiple comparisons post-test).

H. *In silico* analysis of *EGR2* and *FABP4* expression by lung, liver, spleen and brain macrophages extracted on the basis of *C1QA*$^+$ expression from *(17-19).*

Figure 2

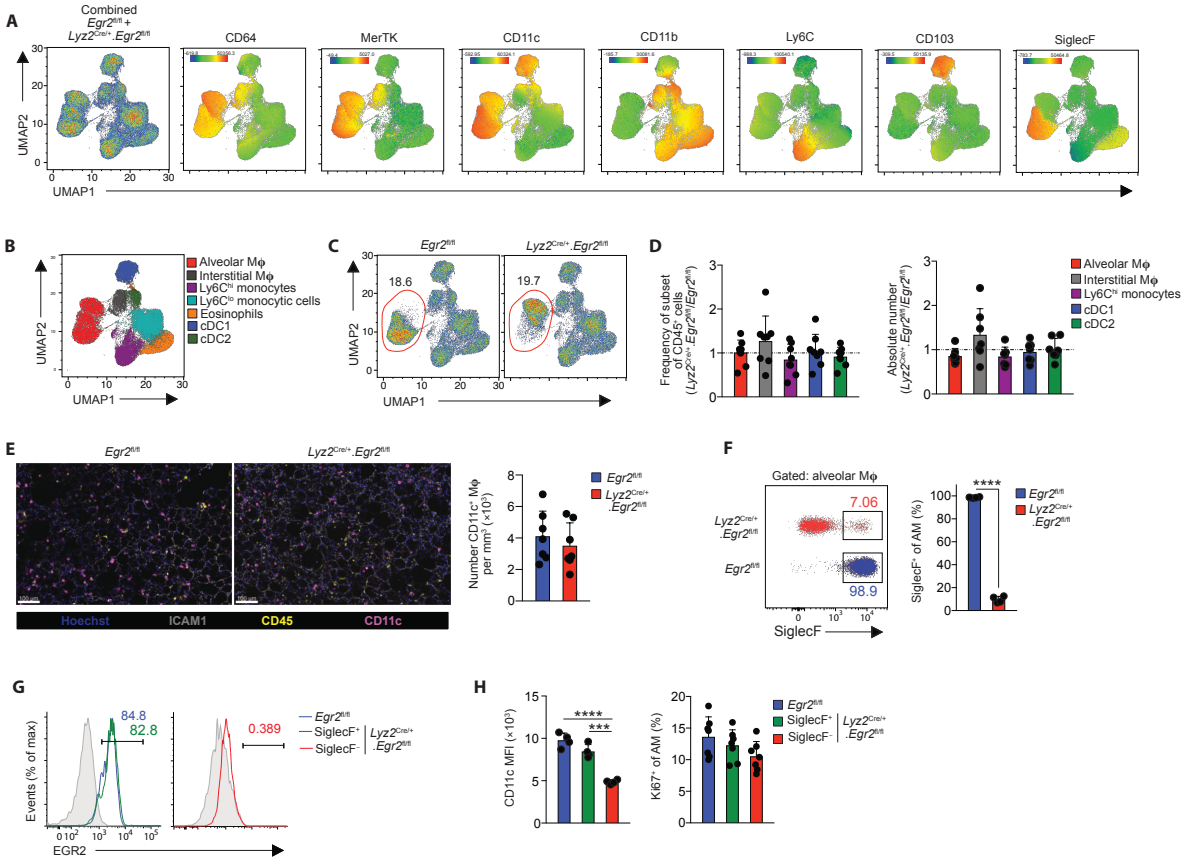

Figure 2: EGR2 is required for the phenotypic identity of alveolar macrophages

A. UMAP analysis of CD3$^-$CD19$^-$NK1.1$^-$Ly6G$^-$CD11b$^+$/CD11c$^+$ cells pooled from adult unmanipulated *Egr2*$^{fl/fl}$ and *Lyz2*$^{Cre/+}$.*Egr2*$^{fl/fl}$ mice (*left panel*). Heatmap plots showing the relative expression of the indicated markers by myeloid clusters.

B. Cluster identity confirmed by manual gating (see **Fig. S3A**).

C. Relative frequency of alveolar macrophages of all CD45$^+$ leukocytes in unmanipulated adult *Egr2*$^{fl/fl}$ and *Lyz2*$^{Cre/+}$.*Egr2*$^{fl/fl}$ mice.

D. Relative frequency and absolute number of alveolar macrophages, cDC1, cDC2, Ly6C^{hi} monocytes and CD64$^+$MHCII$^+$ interstitial macrophages in lung digests from adult unmanipulated *Lyz2*$^{Cre/+}$.*Egr2*$^{fl/fl}$ mice compared with their abundance in *Egr2*$^{fl/fl}$ littermates. Data are pooled from three independent experiments with 8 mice per group.

E. Confocal fluorescence imaging of Fixed Precision Cut Lung Slices from adult unmanipulated *Egr2*$^{fl/fl}$ or *Lyz2*$^{Cre/+}$.*Egr2*$^{fl/fl}$ mice stained with antibodies against ICAM1, CD45 and CD11c (*left*) and quantification of the number of CD11c$^+$ macrophages per mm^3 in each group (*right*). Data are pooled from three independent experiments with 7 mice per group.

F. Representative expression of SiglecF by CD11c^{hi}CD11b^{lo} alveolar macrophages (from **F**) obtained from lung digests from adult unmanipulated *Egr2*$^{fl/fl}$ or *Lyz2*$^{Cre/+}$.*Egr2*$^{fl/fl}$ mice (*left*), frequency of SiglecF$^+$

macrophages in each strain (*right*). Data are from 4 mice per group from one of at least 5 independent experiments. SiglecF; ****p<0.0001 (unpaired Student's *t* test).

G. Representative expression of EGR2 by SiglecF-defined alveolar macrophages. Shaded histograms represent isotype controls. Data are from one of three independent experiments.

H. Mean fluorescence intensity (MFI) of CD11c expression (*left*) and frequency of $Ki67^{+}$ SiglecF-defined $CD11c^{hi}CD11b^{lo}$ alveolar macrophages (*right*) amongst lung digests from adult unmanipulated $Egr2^{fl/fl}$ and $Lyz2^{Cre/+}.Egr2^{fl/fl}$ mice. Data are from 4 mice per group from one of at least 5 independent experiments. *** p<0.001, **** p<0.0001 (One-way ANOVA followed by Tukey's multiple comparisons post-test).

Symbols represent individual mice in all graphs and error bars represent the standard deviation.

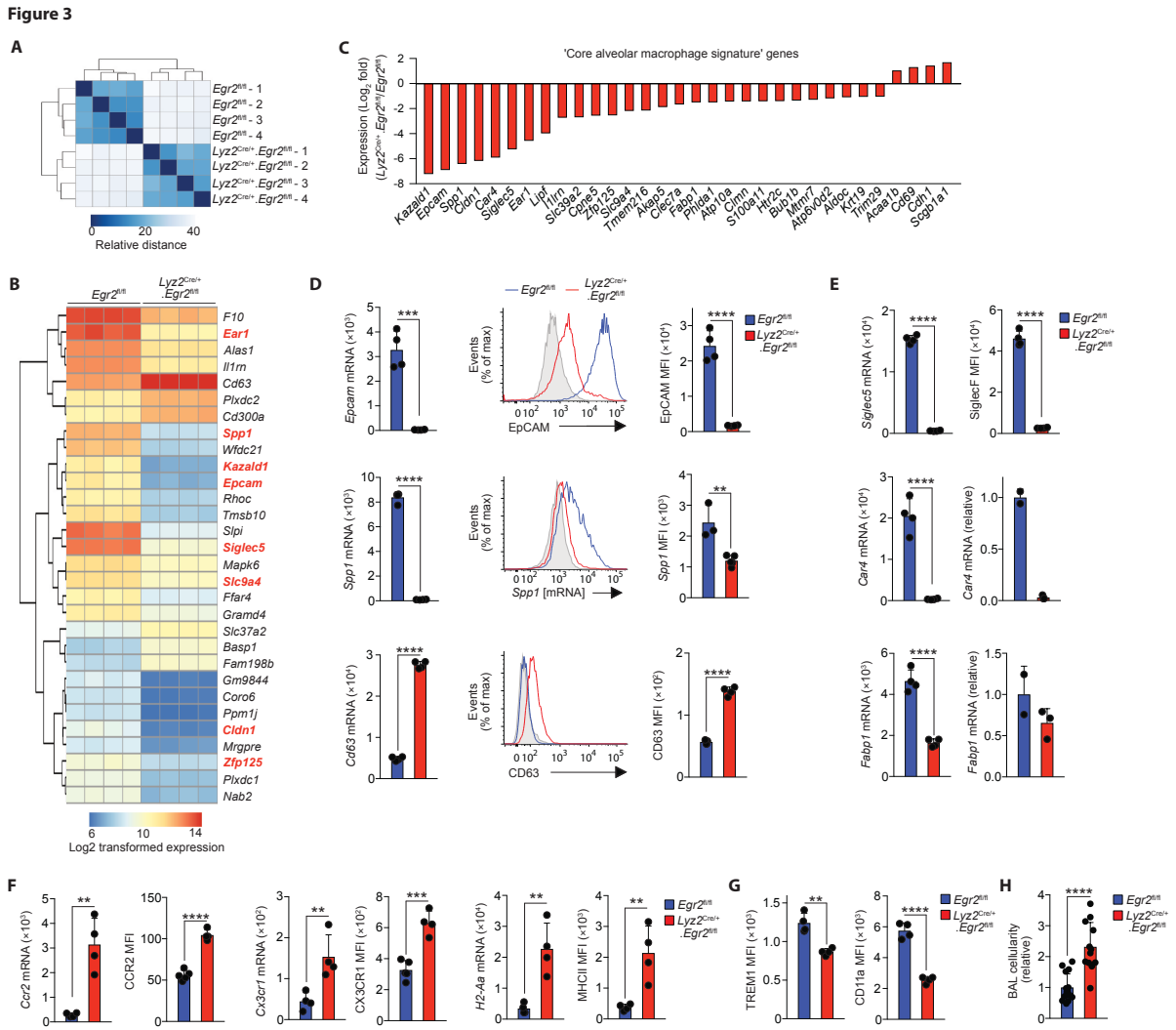

Figure 3: EGR2 controls tissue-specific transcriptional programme of alveolar macrophages

A. Heatmap of RNA-seq data showing the euclidean distance between samples from adult *Egr2*$^{fl/fl}$ and *Lyz2*$^{Cre/+}$.*Egr2*$^{fl/fl}$ mice.

B. Heatmap showing log2 transformed expression of the 30 most differentially expressed genes by alveolar macrophages *Egr2*$^{fl/fl}$ and *Lyz2*$^{Cre/+}$.*Egr2*$^{fl/fl}$ mice. Each column represents a biological replicate with four mice per group. Genes highlighted in red appear in the 'core signature' of alveolar macrophages as defined by the ImmGen Consortium *(12)*.

C. Log_2-fold expression of differentially expressed genes that form part of the 'core signature' of alveolar macrophages as defined by the ImmGen Consortium *(12)*.

D. Expression of *Epcam*, *Spp1* and *Cd63* from the RNA-seq dataset (*left panels*), representative flow cytometric validation of EpCAM, *Spp1* (mRNA detected by PrimeFlow technology) and CD63 expression (*middle panels*) and replicate MFI expression data of each of these markers by alveolar macrophages from adult unmanipulated *Egr2*$^{fl/fl}$ and *Lyz2*$^{Cre/+}$.*Egr2*$^{fl/fl}$ mice. Data are from one of two independent experiments with 5 (Cre^{-}) and 4 (Cre^{+}) mice per group.

E. Expression of *Siglec5*, *Car4* and *Fabp1* from the RNA-seq dataset (*left panels*) and validation by flow cytometry (SiglecF) or qPCR (*Car4*, *Fabp1*). Data for SiglecF is from one of at least 10 independent experiments with 5 ($Egr2^{fl/fl}$) and 4 ($Lyz2^{Cre/+}.Egr2^{fl/fl}$) mice per group. Data for *Car4* and *Fabp1* represents 2 ($Egr2^{fl/fl}$) and 4 ($Lyz2^{Cre/+}.Egr2^{fl/fl}$) mice per group.

F. Expression of *Ccr2*, *Cx3cr1* and *H2-Aa* from the RNA-seq dataset and replicate MFI expression data of CCR2, CX3CR1 and MHCII as determined by flow cytometry. Data are from one of two independent experiments with 5 ($Egr2^{fl/fl}$) and 4 ($Lyz2^{Cre/+}.Egr2^{fl/fl}$) mice per group.

G. Replicate MFI data of for CD11a and TREM1 expression as determined by flow cytometry. Data are from one of two independent experiments with 5 ($Egr2^{fl/fl}$) and 4 ($Lyz2^{Cre/+}.Egr2^{fl/fl}$) mice per group.

H. Absolute number of $CD11c^{hi}CD11b^{-}$ alveolar macrophages present in the BAL of adult unmanipulated $Lyz2^{Cre/+}.Egr2^{fl/fl}$ mice relative to their abundance in $Egr2^{fl/fl}$ littermates. Data are pooled from three independent experiments with 15 ($Egr2^{fl/fl}$) and 12 ($Lyz2^{Cre/+}.Egr2^{fl/fl}$) mice per group.

Symbols represent individual mice in all graphs and error bars represent the standard deviation. *p<0.05, **p<0.01, ***p<0.001, ****p<0.0001 (unpaired Student's *t* test).

Figure 4

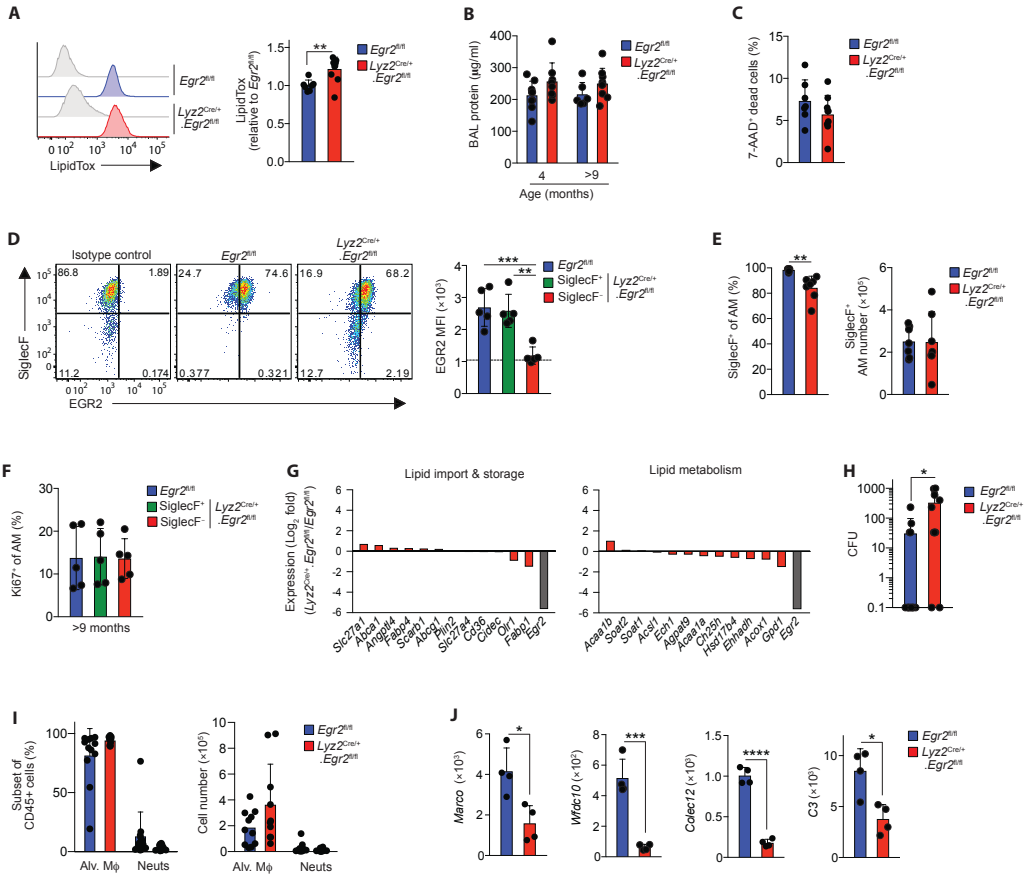

Figure 4: EGR2 controls distinct functional characteristics of alveolar macrophages

A. Representative LipidTox staining of alveolar macrophages from the BAL fluid of unmanipulated adult *Egr2*$^{fl/fl}$ or *Lyz2*$^{Cre/+}$.*Egr2*$^{fl/fl}$ mice (*left*). Graph shows the mean fluorescence intensity (MFI) of LipidTox in alveolar macrophages from *Lyz2*$^{Cre/+}$.*Egr2*$^{fl/fl}$ mice relative to those from *Egr2*$^{fl/fl}$ mice. Data are from 7 (*Egr2*$^{fl/fl}$) and 10 (*Lyz2*$^{Cre/+}$.*Egr2*$^{fl/fl}$) mice per group pooled from three independent experiments. **p<0.01 (unpaired Student's *t*-test).

B. Protein levels in the BAL fluid of *Egr2*$^{fl/fl}$ or *Lyz2*$^{Cre/+}$.*Egr2*$^{fl/fl}$ mice at 4 or 9-12 months of age. Data are from 6-9 mice per group pooled from two independent cohorts of aged mice.

C. Frequency of 7-AAD^{+} (dead) cells in the BAL fluid of *Egr2*$^{fl/fl}$ or *Lyz2*$^{Cre/+}$.*Egr2*$^{fl/fl}$ mice at 9-12 months of age. Data are from 6-9 mice per group pooled from two independent cohorts of aged mice.

D. Representative expression of SiglecF and EGR2 by CD11c^{hi}CD11b^{lo} macrophages and MFI of EGR2 by SiglecF-defined CD11c^{hi}CD11b^{lo} macrophages obtained from 11-12 month old *Egr2*$^{fl/fl}$ or *Lyz2*$^{Cre/+}$.*Egr2*$^{fl/fl}$ mice. Data are from 5 mice per group pooled from two independent cohorts of aged mice. ** p<0.01, *** p<0.001 (One-way ANOVA followed by Tukey's multiple comparisons post-test.)

E. Frequency (*left*) and absolute number (*right*) of SiglecF^{+} cells amongst CD11c^{hi}CD11b^{lo} macrophages obtained from 11-12 month old *Egr2*$^{fl/fl}$ or *Lyz2*$^{Cre/+}$.*Egr2*$^{fl/fl}$ mice. Data are from 7 mice per group pooled from three independent cohorts of aged mice. **p<0.01 (unpaired Student's *t*-test).

F. Frequency of Ki67^{+} cells amongst SiglecF-defined CD11c^{hi}CD11b^{lo} macrophages obtained from 11-12 month old *Egr2*$^{fl/fl}$ or *Lyz2*$^{Cre/+}$.*Egr2*$^{fl/fl}$ mice. Data are from 5 mice per group pooled from two independent experiments.

G. Log_2-fold expression of genes that are implicated in lipid uptake or metabolism in alveolar macrophages as defined by *(8)*. Expression of *Egr2* is included as a reference.

H. Bacterial levels (colony forming units, CFU) in the BAL fluid of $Egr2^{fl/fl}$ or $Lyz2^{Cre/+}.Egr2^{fl/fl}$ mice 14hrs after infection. Data are from 10 ($Lyz2^{Cre/+}.Egr2^{fl/fl}$) or 12 ($Egr2^{fl/fl}$) mice per group pooled from three independent experiments. *p<0.05 (Mann Whitney test).

I. Frequency (*left*) and absolute number (*right*) of $CD11c^{hi}CD11b^{lo}$ alveolar macrophages and $Ly6G^{+}$ neutrophils in the BAL fluid of $Egr2^{fl/fl}$ or $Lyz2^{Cre/+}.Egr2^{fl/fl}$ mice 14hrs after infection. Data represent 10 ($Lyz2^{Cre/+}.Egr2^{fl/fl}$) or 11 ($Egr2^{fl/fl}$) mice per group pooled from three independent experiments.

J. Expression of *Marco*, *Wfdc10, Colec12* and *C3* from the RNA-seq dataset (*left panels*). *p<0.05, ***p<0.001, ****p<0.0001 (unpaired Student's *t*-test).

Symbols represent individual mice in all graphs and error bars represent the standard deviation.

Figure 5

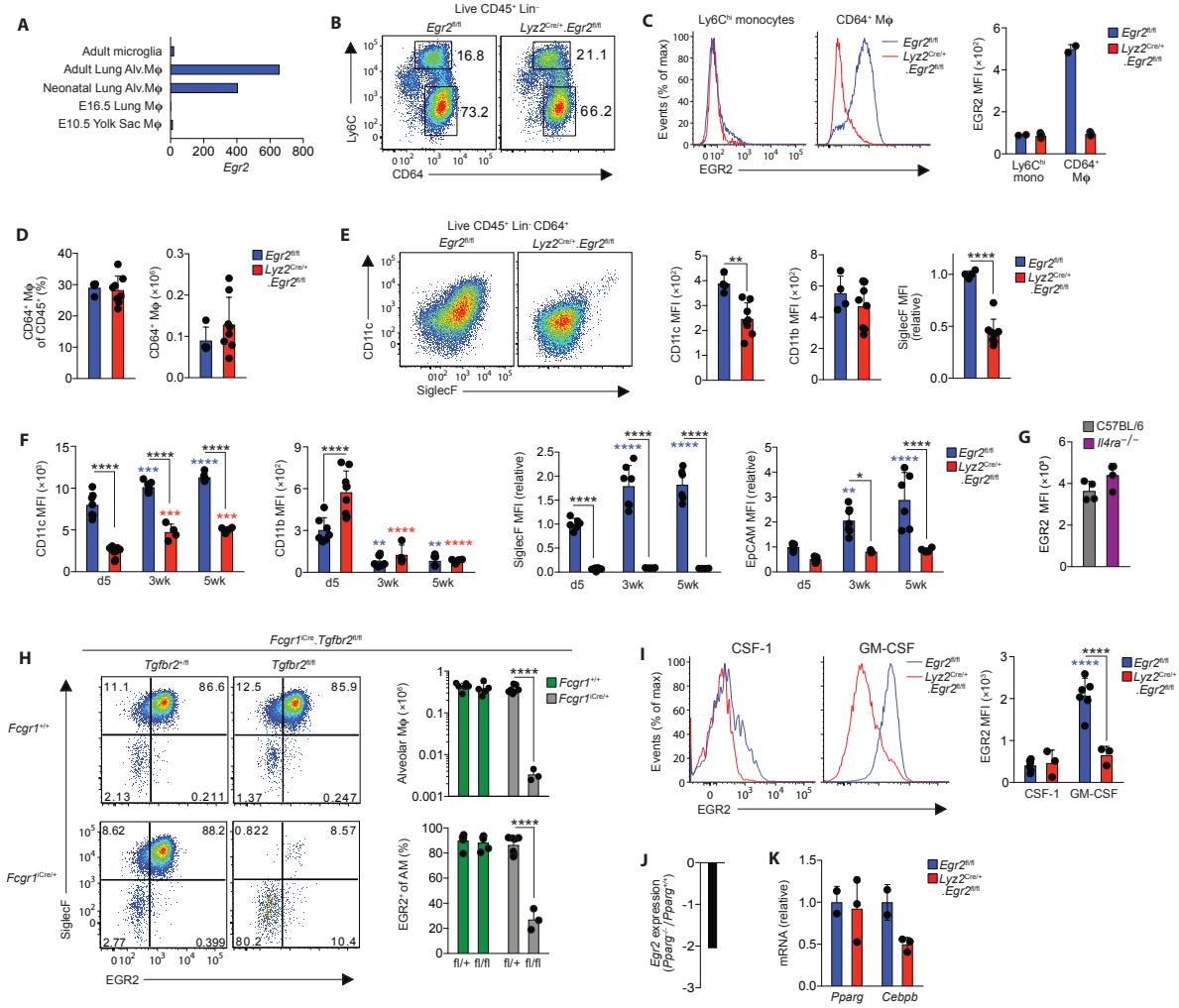

Figure 5: TGFβ and CSF2 drive EGR2 expression

A. Normalised expression (by DESeq2) of *Egr2* by the indicated populations (data obtained from the ImmGen Consortium).

B. Representative expression of Ly6C and CD64 by live CD45^{+}CD3^{-}CD19^{-}Ly6G^{-} cells from the lungs of unmanipulated newborn *Egr2*$^{fl/fl}$ or *Lyz2*$^{Cre/+}$.*Egr2*$^{fl/fl}$ mice. Data are from one of two independent experiments performed.

C. Histograms show representative expression of EGR2 by CD64^{+} 'pre-alveolar macrophages' and Ly6C^{hi} monocytes from the lungs of unmanipulated newborn *Egr2*$^{fl/fl}$ or *Lyz2*$^{Cre/+}$.*Egr2*$^{fl/fl}$ mice and bar chart shows the mean fluorescent intensity (MFI) of EGR2 expression by these cells. Data are from one of two independent experiments performed with 2 (*Egr2*$^{fl/fl}$) or 5 (*Lyz2*$^{Cre/+}$.*Egr2*$^{fl/fl}$) mice per group.

D. Frequency and absolute number of CD64^{+} 'pre-alveolar macrophages' from mice in **B.** Data are pooled from two independent experiments with 4 (*Egr2*$^{fl/fl}$) or 8 (*Lyz2*$^{Cre/+}$.*Egr2*$^{fl/fl}$) mice per group.

E. FACS plots show representative expression of CD11c and SiglecF by $CD64^+$ 'pre-alveolar macrophages' from mice in **B** and bar chart shows the MFI of CD11c, SiglecF and CD11b expression by these cells. Data are pooled from two independent experiments with 4 ($Egr2^{fl/fl}$) or 8 ($Lyz2^{Cre/+}.Egr2^{fl/fl}$) mice per group.

F. MFI of CD11c and CD11b and relative MFI of SiglecF and EpCAM (relative to cells from d5 old $Egr2^{fl/fl}$ mice) expression by $CD11c^{hi}CD11b^{lo}$ alveolar macrophages obtained from unmanipulated $Egr2^{fl/fl}$ or $Lyz2^{Cre/+}.Egr2^{fl/fl}$ mice at the indicated ages. Data are pooled from two independent experiments with 4-9 mice per group. Coloured * denote significance between d5 and 3 and 5 weeks within the $Egr2^{fl/fl}$ (blue) and $Lyz2^{Cre/+}.Egr2^{fl/fl}$ (red) data. **p<0.01, ***p<0.001, ****p<0.0001 (Two-way ANOVA with Tukey's multiple comparisons test).

G. Representative expression of EGR2 by alveolar macrophages from adult WT (C57BL/6) and $Il4ra^{-/-}$ adult mice. Data from one experiment with 4 mice per group.

H. Representative expression of EGR2 and SiglecF by $CD11c^{hi}CD11b^{lo}$ alveolar macrophages obtained from lungs of neonatal (d8) $Fcgr1^{iCre/+}.Tgfbr2^{fl/fl}$ and littermate controls. Bar charts show the absolute numbers of $CD11c^{hi}CD11b^{lo}$ alveolar macrophages (*upper*) and the mean frequency of $EGR2^+$ cells amongst $CD11c^{hi}CD11b^{lo}$ alveolar macrophages (*lower*). Data are pooled from two independent experiments with 3-7 mice per group. **** p<0.0001 (One-way ANOVA followed by Tukey's multiple comparisons post-test).

I. Representative expression of EGR2 (*left*) and MFI of EGR2 (*right*) by FACS-purified $Ly6C^{hi}$ monocytes cultured *in vitro* with recombinant CSF-1 (20ng/ml) or GM-CSF (20ng/ml) for five days. Symbols represent monocytes isolated from individual mice. Data are from 6 $Egr2^{fl/fl}$ (Cre^-) or 3 $Lyz2^{Cre}.Egr2^{fl/fl}$ (Cre^+) mice per group pooled from two independents experiment. **** p<0.0001 (Two-way ANOVA followed by Tukey's multiple comparisons post-test). Coloured * denote significance between CSF-1 and GM-CSF within the $Egr2^{fl/fl}$ (blue) and $Lyz2^{Cre}.Egr2^{fl/fl}$ (red) data.

J. Relative expression of *Egr2* by alveolar macrophages obtained from $Pparg^{fl/fl}$ or $Itgax^{Cre}.Pparg^{fl/fl}$ mice from the ImmGen Consortium.

K. qPCR analysis of *Pparg* and *Cebpb* mRNA by BAL cells from unmanipulated adult $Egr2^{fl/fl}$ or $Lyz2^{Cre}.Egr2^{fl/fl}$ mice. Data represent 2 $Egr2^{fl/fl}$ or 4 $Lyz2^{Cre}.Egr2^{fl/fl}$ mice per group.

Symbols represent individual mice in all graphs and error bars represent the standard deviation.

Figure 6

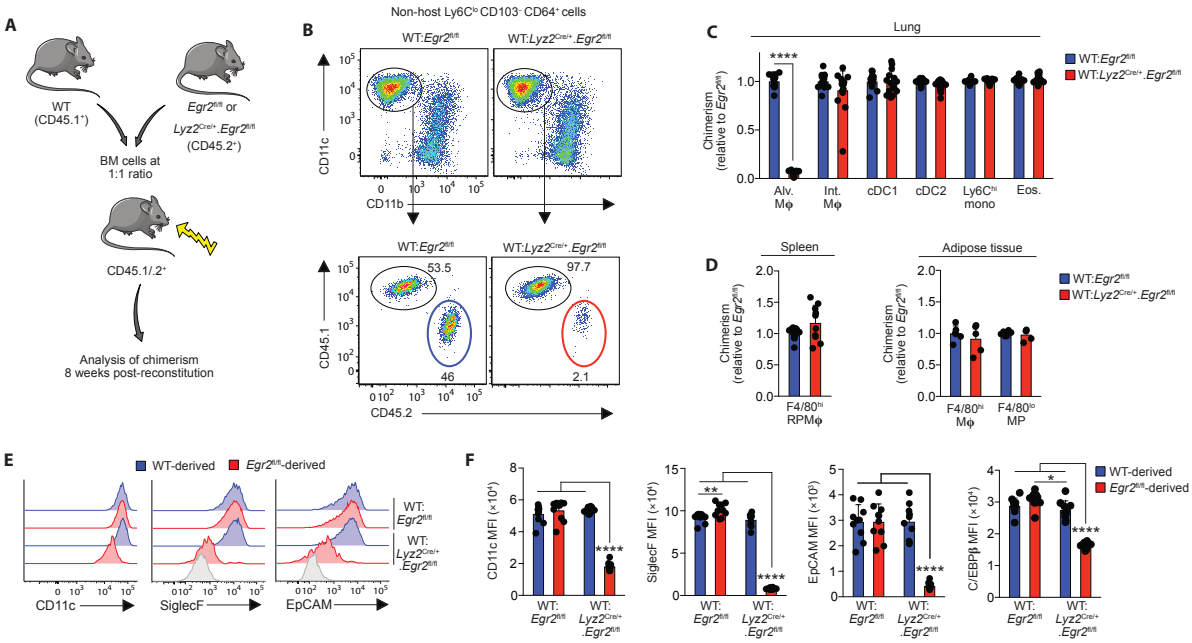

Figure 6: *Egr2* deficiency confers a competitive disadvantage on alveolar macrophages

A. Schematic of the generation of mixed bone marrow chimeric mice

B. Representative expression of CD11c and CD11b by Ly6C^{lo}CD64^{+} macrophages amongst live CD45^{+}CD3^{-}CD19^{-}Ly6G^{-}CD103^{-} cells (*upper panels*) and representative expression of CD45.1 and CD45.2 by CD11c^{hi}CD11b^{lo} alveolar macrophages (*lower panels*) from WT:*Egr2*$^{fl/fl}$ or WT:*Lyz2*$^{Cre/+}$.*Egr2*$^{fl/fl}$ chimeric mice.

C. Contribution of *Egr2*$^{fl/fl}$ BM to the indicated lung myeloid populations in WT:*Lyz2*$^{Cre/+}$.*Egr2*$^{fl/fl}$ chimeric mice relative to WT:*Egr2*$^{fl/fl}$ mice. Chimerism was normalised to Ly6C^{hi} blood monocytes before normalisation of *Lyz2*$^{Cre/+}$.*Egr2*$^{fl/fl}$ to *Egr2*$^{fl/fl}$. Data are from 15 (WT:*Lyz2*$^{Cre/+}$.*Egr2*$^{fl/fl}$) or 16 (WT:*Egr2*$^{fl/fl}$) mice per group pooled from three independent experiments. **** p<0.0001 (Student's *t*-test with Holm-Sidak correction).

D. Contribution of *Egr2*$^{fl/fl}$ BM to splenic red pulp F4/80^{hi} macrophages and F4/80-defined mononuclear phagocytes in adipose tissue from chimeric in **C.** Spleen data are from 15 (WT:*Lyz2*$^{Cre/+}$.*Egr2*$^{fl/fl}$) or 16 (WT:*Egr2*$^{fl/fl}$) mice per group pooled from three independent experiments and adipose data from 5 (WT:*Lyz2*$^{Cre/+}$.*Egr2*$^{fl/fl}$) or 6 (WT:*Egr2*$^{fl/fl}$) mice per group pooled from two independent experiments.

E. Representative expression of CD11c, SiglecF and EpCAM by WT- and *Egr2*$^{fl/fl}$-derived alveolar macrophages in WT:*Egr2*$^{fl/fl}$ or WT:*Lyz2*$^{Cre/+}$.*Egr2*$^{fl/fl}$ chimeric mice. Shaded histograms represent FMO controls.

F. Mean fluorescent intensity (MFI) of CD11c, SiglecF, EpCAM and C/EBPβ expression by WT- and *Egr2*$^{fl/fl}$-derived alveolar macrophages in WT:*Egr2*$^{fl/fl}$ or WT:*Lyz2*$^{Cre/+}$.*Egr2*$^{fl/fl}$ chimeric mice. Data represent 10 mice per group from one experiment of three performed. **** p<0.0001 (One-way ANOVA followed by Tukey's multiple comparisons post-test).

Symbols represent individual mice in all graphs and error bars represent the standard deviation.

Figure 7

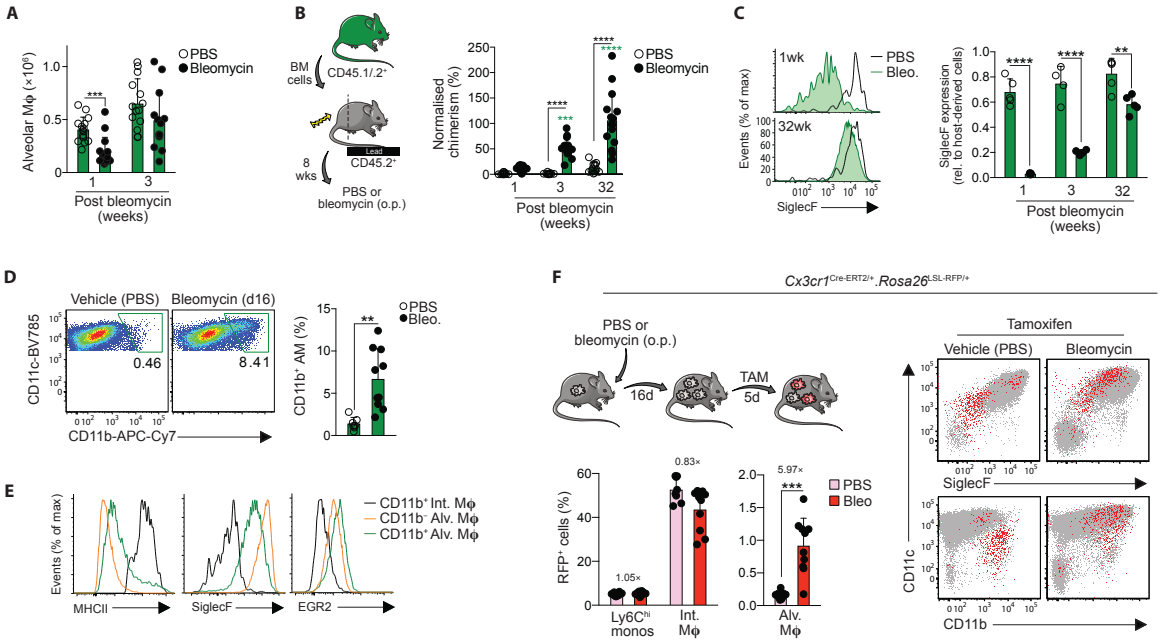

Figure 7: Monocyte-derived, CX3CR1^{+} parenchymal macrophages can replenish the alveolar macrophage niche following injury

A. Absolute numbers of alveolar macrophages 1- and 3-weeks following bleomycin administration or PBS vehicle control. Data are pooled from two independent experiments at each time point with 13-15 mice per group. ***p<0.001 (unpaired Student's *t* test with Holm-Sidak correction).

B. Non-host chimerism of alveolar macrophages in tissue protected bone marrow chimeric mice at 1-, 3- or 32-weeks following administration of bleomycin or PBS vehicle control. Chimerism is normalised to Ly6C^{hi} blood monocytes. Data are pooled from two independent experiments at each time point with 13-15 mice per group. ***p<0.001, ****p<0.0001 (Two-way ANOVA with Tukey's multiple comparisons test)

C. Expression of SiglecF by CD11c^{hi}CD11b^{lo} alveolar macrophages from the lung of mice in **B**. at 1 week and 32 weeks post bleomycin or PBS administration. Data are from one of two independent experiments at each time point with 4 mice per group. ***p<0.001, ****p<0.0001 (Two-way ANOVA with Tukey's multiple comparisons test).

D. Representative expression of CD11c and CD11b by CD11c^{hi}CD64^{+} cells obtained by BAL from WT mice two weeks after instillation of bleomycin or vehicle control (*left)*. Graph shows the mean frequency of CD11b^{+} alveolar macrophages (*right*). Data are pooled from two independent experiments with 7 (PBS) or 10 (bleomycin) mice per group. **p<0.01 (unpaired Student's *t* test).

E. Representative expression of MHCII, SiglecF and EGR2 by CD11b^{+} interstitial macrophages and CD11b-defined CD11c^{hi} alveolar macrophages.

F. Experimental scheme for the induction of lung injury and tamoxifen administration in *Cx3cr1*$^{Cre-ERT2/+}$.*Rosa26*$^{LSL-RFP/+}$ fate mapping mice. Lower graphs show the levels of recombination in Ly6C^{hi} monocytes, CD64^{+} interstitial macrophages and alveolar macrophages from *Cx3cr1*$^{Cre-ERT2/+}$.*Rosa26*$^{LSL-RFP/+}$

mice administered bleomycin or vehicle control. Representative expression of CD11c, SiglecF and CD11b by RFP^+ (red) or RFP^- (grey) cells present in the BAL fluid of *Cx3cr1*$^{Cre\text{-}ERT2/+}$.*Rosa26*$^{LSL\text{-}RFP/+}$ mice 3 weeks after bleomycin or vehicle instillation. Graphs show the mean fluorescent intensity (MFI) of CD11c and SiglecF expression by RFP^+ cells.

Symbols represent individual mice in all graphs and error bars represent the standard deviation.

Figure 8

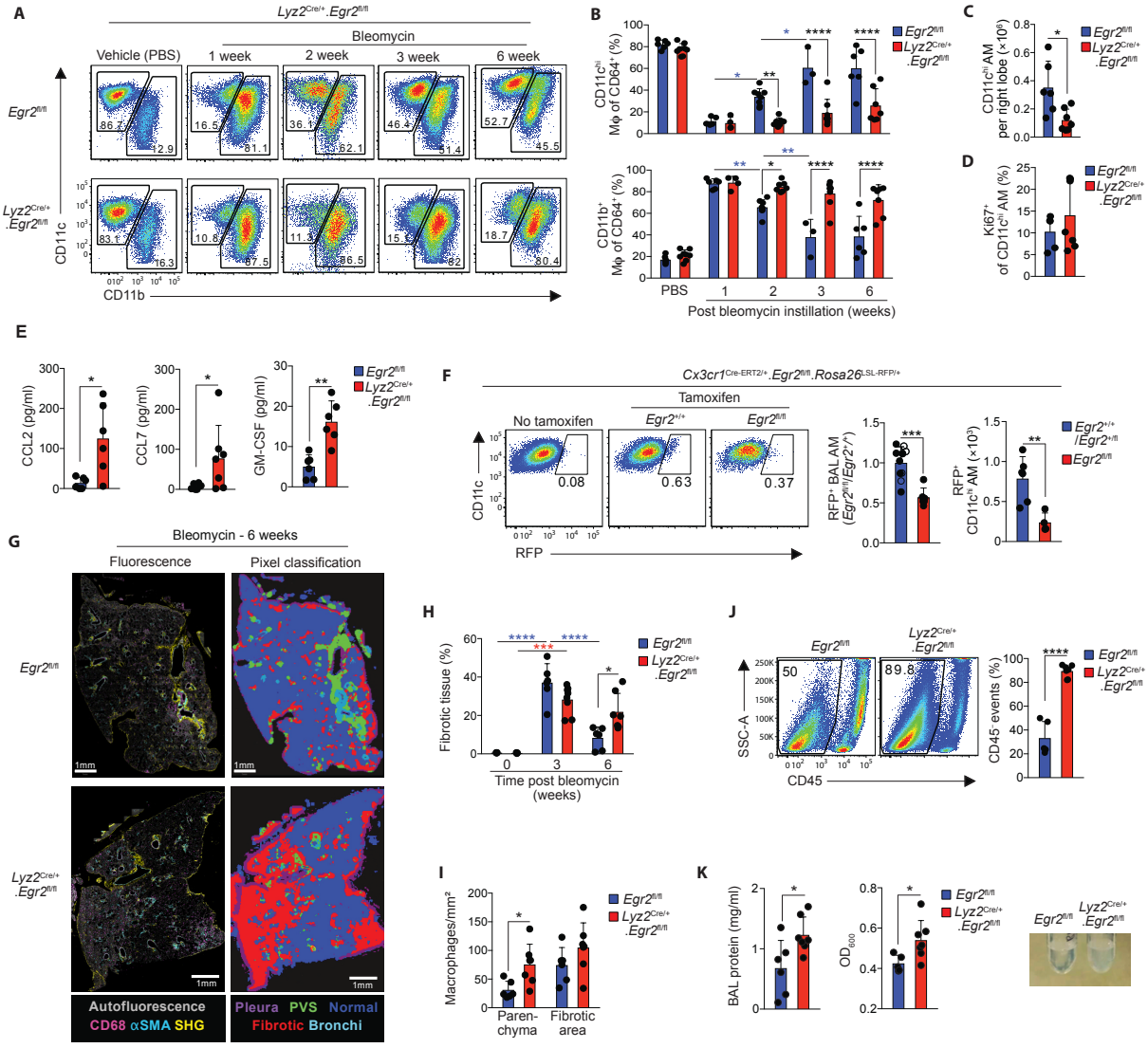

Figure 8: EGR2 is indispensable for the repopulation of the alveolar macrophage niche and tissue repair following lung injury

A. Representative expression of CD11c and CD11b by live CD45^{+}CD3^{-}CD19^{-}Ly6G^{-}CD64^{+} cells from the lungs of *Egr2*$^{fl/fl}$ and *Lyz2*$^{Cre/+}$.*Egr2*$^{fl/fl}$ mice at 1, 2, 3 or 6 weeks post bleomycin or vehicle controls.

B. Frequency of CD11c^{hi}CD11b^{lo} alveolar macrophages and CD11c^{var}CD11b^{+} cells from mice in **A.** Data are pooled from at least two independent experiments at each time point with 3-7 mice per group. *p<0.05. **p<0.01, p<0.001, ****p<0.0001 (Two-way ANOVA with Tukey's multiple comparisons test).

C. Absolute number of CD11c^{hi}CD11b^{lo} alveolar macrophages in lungs six weeks post bleomycin instillation. Data are pooled from two independent experiments with 6 (*Egr2*$^{fl/fl}$) or 7 (*Lyz2*$^{Cre/+}$.*Egr2*$^{fl/fl}$) mice per group. *p<0.05 (Mann Whitney test).

D. Frequency of Ki67^{+} CD11c^{hi}CD11b^{lo} alveolar macrophages in lungs six weeks post bleomycin instillation. Symbols represent individual mice. Data are pooled from two independent experiments with 6 (*Egr2*$^{fl/fl}$) or 7 (*Lyz2*$^{Cre/+}$.*Egr2*$^{fl/fl}$) mice per group.

E. CCL2, CCL7 and GM-CSF levels in BAL fluid obtained from *Egr2*$^{fl/fl}$ and *Lyz2*$^{Cre/+}$.*Egr2*$^{fl/fl}$ mice six weeks post bleomycin instillation. Data are pooled from two independent experiments with 6 mice per group. *p<0.05, Mann Whitney test (CCL2, CCL7), **p<0.01 (unpaired Student's *t* test; GM-CSF).

F. Representative expression of RFP by CD11c^{hi}CD64^{+} alveolar macrophages present in the BAL fluid of *Cx3cr1*$^{Cre-ERT2/+}$.*Rosa26*$^{LSL-RFP/+}$.*Egr2*$^{fl/fl}$ and their *Cx3cr1*$^{Cre-ERT2/+}$.*Rosa26*$^{LSL-RFP/+}$.*Egr2*$^{+/+}$ (open circles) or *Cx3cr1*$^{Cre-ERT2/+}$.*Rosa26*$^{LSL-RFP/+}$.*Egr2*$^{fl/+}$ (solid circles) controls 3 weeks following instillation of bleomycin or vehicle control. Graphs show the relative frequency (*left*) or absolute number (*right*) of RFP^{+} alveolar macrophages present in the BAL fluid. Data are from one experiment of two (number) with 6 (*Egr2*$^{+/+}$ [open symbols]/*Egr2*$^{fl/+}$ [filled symbols]) or 4 mice (*Egr2*$^{fl/fl}$) per group, or pooled from two independent experiments (frequency) at each time point with 10 (*Egr2*$^{+/+}$ [open symbols]/*Egr2*$^{fl/+}$ [filled symbols]) or 6 (*Egr2*$^{fl/fl}$) per group. ** p<0.01, ***p<0.001 (Unpaired Student's t test).

G. 2-photon fluorescence imaging of lung tissue from adult *Egr2*$^{fl/fl}$ and *Lyz2*$^{Cre/+}$.*Egr2*$^{fl/fl}$ mice 6 weeks following bleomycin administration. Sections were stained with CD68, αSMA and DAPI. Autofluorescence is depicted in grey and collagen was detected by second harmonic generation (SHG). Pixel classification was used to segment lung regions of interest: (1) normal lung parenchyma/alveolar tissue, (2) pathologic/fibrotic tissue and (3) collagen rich areas (perivascular/bronchial spaces and pleura) were segmented to avoid false fibrotic region detection.

H. Quantification of fibrotic score of lung tissue from *Egr2*$^{fl/fl}$ and *Lyz2*$^{Cre/+}$.*Egr2*$^{fl/fl}$ 3 or 6 weeks following bleomycin administration or PBS controls (from 3 week time point). See **Fig. S10.** Data are pooled from two independent experiments with 6 (*Egr2*$^{fl/fl}$) or 7 (*Lyz2*$^{Cre/+}$.*Egr2*$^{fl/fl}$) mice per group. *p<0.05, **p<0.01, ***p<0.001, ****p<0.0001 (Two-way ANOVA followed by Tukey's multiple comparisons test).

I. Quantification of macrophage density in the parenchyma and fibrotic areas of lung tissue from *Egr2*$^{fl/fl}$ and *Lyz2*$^{Cre/+}$.*Egr2*$^{fl/fl}$ 6 weeks following bleomycin administration. See **Fig. S10.** Data are pooled from two independent experiments with 6 (*Egr2*$^{fl/fl}$) or 7 (*Lyz2*$^{Cre/+}$.*Egr2*$^{fl/fl}$) mice per group. *p<0.05 (Student's t test with Holm-Sidak correction for multiple tests).

J. SSC-A profile and expression of CD45 by BAL obtained from *Egr2*$^{fl/fl}$ and *Lyz2*$^{Cre/+}$.*Egr2*$^{fl/fl}$ 6 weeks following bleomycin administration. Graph shows the mean frequency of CD45^{+} cells amongst all live, single events. Symbols represent individual mice. Data are pooled from two independent experiments with 5 (*Egr2*$^{fl/fl}$) or 7 (*Lyz2*$^{Cre/+}$.*Egr2*$^{fl/fl}$) mice per group. ****p<0.0001 (unpaired Student's t test).

K. Total protein concentration (*left*), turbidity (*centre*) and representative pictures (*right*) of BAL fluid from *Egr2*$^{fl/fl}$ and *Lyz2*$^{Cre/+}$.*Egr2*$^{fl/fl}$ 6 weeks following bleomycin administration. Symbols represent individual mice. Data are pooled from two independent experiments with 6 (*Egr2*$^{fl/fl}$) or 7 (*Lyz2*$^{Cre/+}$.*Egr2*$^{fl/fl}$) mice per group. *p<0.05 (Mann Whitney test).

Symbols represent individual mice in all graphs and error bars represent the standard deviation.

Supplementary Information

McCowan *et al.* The transcription factor EGR2 is indispensable for tissue-specific imprinting of alveolar macrophages in health and tissue repair

Supplementary Methods

Supplementary Figures

Supplementary Tables

Supplementary Material and Methods

Transcriptional Analysis.

qPCR: Real-time PCR assays for the detection of mRNAs were performed using Light Cycler System (Roche) and 384-Well Reaction Plates (Roche). Primer sequences detailed in **Table S4**. Reactions were performed using SYBR Green System (LightCycler® 480 SYBR Green I Master) according to the manufacturer protocol. 1ul of cDNA (1:50 dilution) were used per sample in a total reaction volume of 10uL. The temperature profile used was as follows: pre-denaturation 5 min at 95°C and then 45 cycles of denaturation for 10s at 95°C, annealing 10s at 60°C, elongation 10s at 72°C. Fluorescence data collection was performed at the end of each elongation step. All samples were tested in duplicates and nuclease free water was used as a non-template control. The relative change was calculated using the $2^{-\Delta\Delta Ct}$ method *(65)*, normalized to *Ppia*.

Bulk sequencing: Alveolar macrophages were FACS-purified from lung digests from unmanipulated female *Lyz2*^{Cre}.*Egr2*$^{fl/fl}$ mice or *Egr2*$^{fl/fl}$ controls. For each population, 25,000 cells were sorted into 500ml RLT buffer (Qiagen) and snap frozen on dry ice. RNA was isolated using the RNeasy Plus Micro kit (Qiagen). RNA samples were quantified using Qubit 2.0 Fluorometer (Life Technologies, Carlsbad, CA, USA) and RNA integrity was checked with 2100 TapeStation (Agilent Technologies, Palo Alto, CA, USA). SMART-Seq v4 Ultra Low Input Kit for Sequencing was used for full-length cDNA synthesis and amplification (Clontech, Mountain View, CA), and Illumina Nextera XT library was used for sequencing library preparation. Briefly, cDNA was fragmented and adaptor was added using Transposase, followed by limited-cycle PCR to enrich and add index to the cDNA fragments. The final library was assessed with Qubit 2.0 Fluorometer and Agilent TapeStation. The sequencing libraries were multiplexed and clustered on two lanes of a flowcell. After clustering, the flowcell were loaded on the Illumina HiSeq instrument according to manufacturer's instructions. The samples were sequenced using a 2x150 Paired End (PE) configuration. Image analysis and base calling were conducted by the HiSeq Control Software (HCS) on the HiSeq instrument. Raw sequence data (.bcl files) generated from Illumina HiSeq were be converted into fastq files and de-multiplexed using Illumina bcl2fastq v. 2.17 program. One mis-match was allowed for index sequence identification. After demultiplexing, sequence data was checked for overall quality and yield. Then, sequence reads were trimmed to remove possible adapter sequences and nucleotides with poor quality using Trimmomatic v.0.36. The trimmed reads were mapped to the *Mus musculus* mm10 reference genome available on ENSEMBL using the STAR aligner v.2.5.2b. The STAR aligner uses a splice aligner that detects splice junctions and incorporates them to help align the entire read sequences. BAM files were generated as a result of this step. Unique gene hit counts were calculated by using featureCounts from the Subread package v.1.5.2. Only unique reads that fell within exon regions were counted. After extraction of gene hit counts, the gene hit counts table was used for downstream differential expression analysis. Using DESeq2, a comparison of gene expression between the groups of samples was performed. The Wald test was used to generate p-values and Log2 fold changes. Genes with adjusted p-values < 0.05 and absolute log2 fold changes > 1 were called as differentially expressed genes for each comparison.

scRNA-seq: CD11c^{+} and CD11b^{+} cells, excluding Ly6G^{+} and SiglecF^{+}CD11b^{+} eosinophils, were FACS-purified from unmanipulated an adult *Rag1*$^{-/-}$ mouse. Single cells were processed through the Chromium Single Cell Platform using the Chromium Single Cell 3' Library and Gel Bead Kit V2 and the Chromium Single Cell A Chip Kit (both 10X Genomics) as per the manufacturer's protocol *(66)*. Briefly, single myeloid cells were purified by FACS into PBS/2% FBS, washed twice and cell number measured using a Bio-Rad TC20 Automated Cell Counter (BioRad). Approximately 10,000 cells were

loaded to each lane of a 10X chip and partitioned into Gel Beads in Emulsion containing distinct barcodes in the Chromium instrument, where cell lysis and barcoded reverse transcription of RNA occurred, followed by amplification, fragmentation and 5' adaptor and sample index attachment. Libraries were sequenced on an Illumina HiSeq 4000. For analysis, Illumina BCL sequencing files were demultiplexed using 10x Cell Ranger (version 2.1.1; https://www.10xgenomics.com; 'cellranger_mkfastq'). Resultant FASTQ files were fed into 'cellranger_count' with the transcriptome 'refdata-cellranger-mm10-1.2.0' to perform genome alignment, filtering, barcode counting and UMI counting. Downstream QC, clustering and gene expression analysis was performed using the Seurat R package (V3; R version 4.0.2) following the standard pre-processing workflow *(67)*. Cells were filtered on QC covariates used to identify nonviable cells or doublets: number of unique genes per cell (nFeatureRNA >200 & <4000); percentage mitochondrial genes (<20%). Data for resultant 3936 cells were normalized and scaled prior to PCA analysis. Unsupervised clustering based on the first 20 principal components of the most variably expressed genes was performed using a KNN graph-based approach and resultant clusters visualised using the Uniform Manifold Approximation and Projection (UMAP) method. Differential gene expression analysis was used to identify genes expressed by each cell cluster relative to all others, using the nonparametric Wilcoxon rank-sum test and p-value threshold of <0.05. Canonical cell phenotypes were assigned to individual clusters based on the expression of known landmark gene expression profiles.

Publicly available datasets were downloaded from the COVID-19 Cell Atlas *(17-19)* to perform *in silico* analysis of EGR2 expression in human tissue macrophages. Data were pre-processed and merged using the Seurat R package (V3; R version 4.0.2) following standard methods. Macrophages were extracted based on the expression of C1QA > 0 to compare expression of EGR2 in different human tissue settings.

Immunofluorescence imaging. Imaging was performed as described recently *(68)*. Briefly, samples were permeabilized and blocked for 20min in PBS/Neutral goat serum (NGS) 10%/BSA1%/TritonX-100 (Tx100) 0.3%/Azide 0.05% at 37 °C and stained with 150 µl rabbit anti-CD68 Ab (Polyclonal, ab125212, abcam, 1/200) diluted in PBS/ NGS10%/BSA1%/ TX-100 0.3%/Azide 0.05% for 20min. Samples were washed 3 times with PBS/BSA1%/TX-100 0.1%/Azide 0.05% before adding 150 µl of a solution containing DAPI (1/10000), aSMA-Cy3 (clone 1A4, Sigma, 1/1000), anti-rabbit-AF488 (polyclonal, A-21206 ThermoFisher) diluted in PBS/ NGS10%/BSA1%/ TX-100 0.3%/Azide 0.05% for 1h. Samples were washed 3 times with PBS/BSA1%/TX-100 0.1%/Azide 0.05% and 2 times in PBS. Finally slides were mounted with Vectashield (Vector Laboratories, H-1700). Images were acquired with a Zeiss LSM 880 NLO multiphoton microscope (Carl Zeiss, Oberkochen, Germany) equipped with a 32 channel Gallium arsenide phosphide (GaAsP) spectral detector using 20×/1 NA water immersion objective lens. Samples were excited with a tunable laser (680–1300 nm) set up at 1000 nm and signal was collected onto a linear array of the 32 GaAsp detectors in lambda mode with a resolution of 8.9 nm over the visible spectrum. Spectral images were then unmixed with Zen software (Carl Zeiss) using references spectra acquired from unstained tissues (tissue autofluorescence and second harmonic generation) or beads labelled with Cy3- or AF488-conjugated antibodies.

Image analysis. Fluorescence images were analysed with QuPath *(69)*. Full lung section was annotated using the "simple tissue detection" tool and non-pulmonary tissue (trachea, heart tissue) were manually removed from the annotation. In order to refine the analysis, "Pixel classification" was used to segment lung regions of interest. Briefly, software was trained to recognize the different regions using fluorescence (aSMA, SHG and autofluorescence) and texture (all available) features from example images. 2-3 example areas per regions of interest were annotated for each lung to train the pixel classifier. The following regions were analysed: (1) normal lung parenchyma/alveolar tissue, (2)

pathologic/fibrotic tissue and (3) collagen rich areas: perivascular/(peri)bronchial spaces + pleura were segmented to avoid false fibrotic region detection. Macrophages were detected using the "Positive cell detection" tool and were expressed as the number $DAPI^+$ $CD68^+$ cells/mm^2 of analysed region (full section or regions of interest). Fibrosis was defined as percentage of full section with fibrotic features. All fibrosis scoring and macrophage quantification was performed in a blinded fashion.

Live Precision Cut Lung Slices (PCLS) imaging. Live PCLS procedure was adapted from (https://doi.org/10.1101/680611). Mice were humanely killed by i.p. injection of sodium-pentobarbital, a small incision was made in the trachea and a customized blunted 22G needle was inserted. Subsequently, 1 mL of 2% low-melting point agarose was instilled slowly through the needle. Excised lungs were placed in 10% FBS/RPMI. Lungs were sliced into 300µm thick sections on a vibratome and stained with directly conjugated Ab (**Table S3**) in complete medium (phenol-red free DMEM substituted with 10% FBS) for 20 minutes at 37°C. Slices were imaged on a Zeiss LSM880 confocal microscope in a full incubation chamber at 37°C with 5% CO2. Lung slices were imaged for 2x11min with z-stacks of 22.5um. Acquisition was performed with a 32 channel Gallium arsenide phosphide (GaAsP) spectral detector using 20× objective. Samples were excited simultaneously with 405, 488, 561 and 633 laser lines and signal was collected onto a linear array of the 32 GaAsp detectors in lambda mode with a resolution of 8.9 nm over the visible spectrum. Spectral images were then unmixed with Zen software (Carl Zeiss) using reference spectra acquired from unstained tissues (tissue autofluorescence) or beads labelled with single fluorophores.

4D images analysis. Timelapse images analysis and visualization was performed using Imaris (Bitplane). Neutrophils and macrophages were segmented and tracked using the 'surface' tool using either CD11b and Ly6G fluorescence intensities (neutrophils) or CD11c (macrophages). All surfaces were checked manually to avoid any false detections. Cell behavior was determined using the track displacement length (indicating cell mobility) and the standard deviation of cell sphericity (indicating changes in cell shape over time).

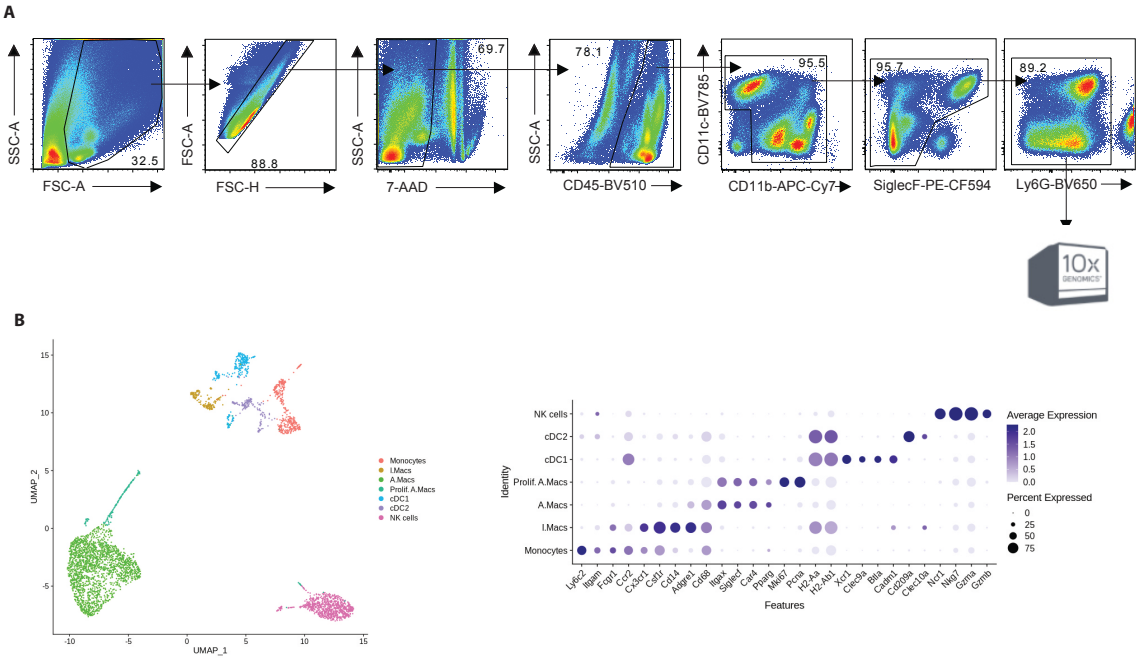

Figure S1: Gating strategy for and cluster annotation of scRNA-seq data

A. Gating strategy used for the purification of mononuclear phagocytes for scRNA-seq analysis using the 10X Genomics platform.

B. UMAP dimensionality reduction analysis of non-granulocyte reveals seven clusters of cells in lungs of adult *Rag1*$^{-/-}$ mice (*left*). Right, expression of canonical markers to validate annotations.

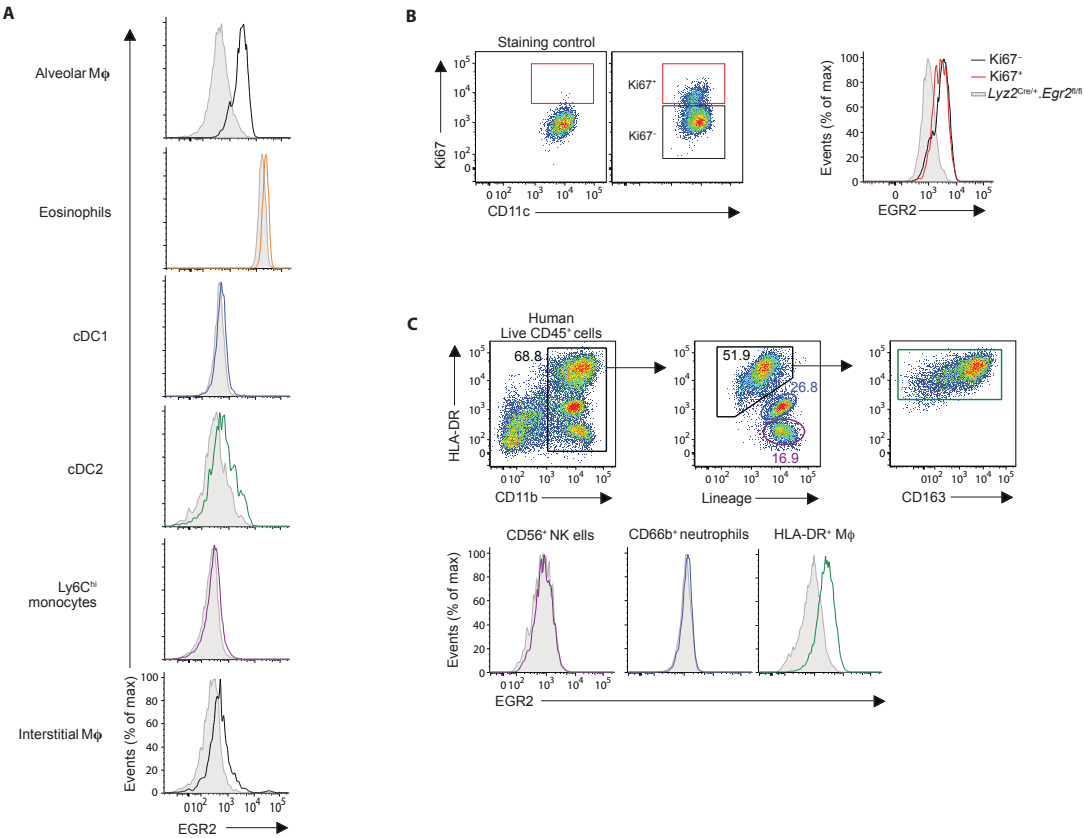

Figure S2: Validation of EGR2 expression by mouse and human alveolar macrophages

A. Expression of EGR2 by indicated myeloid cells in the lungs of *Egr2*$^{fl/fl}$ mice [coloured line] or *Lyz2*$^{Cre/+}$.*Egr2*$^{fl/fl}$ (Cre^{+}) mice [shaded histogram]. Data from one of at least three independent experiments. Alveolar macrophage histogram is duplicated from Figure 1 for reference.

B. Representative expression of EGR2 by Ki67-defined alveolar macrophages from *Egr2*$^{fl/fl}$ mice [coloured lines] or *Lyz2*$^{Cre/+}$.*Egr2*$^{fl/fl}$ mice [shaded histogram]. Data from one of at least three independent experiments.

C. Gating strategy for the identification of alveolar macrophages and granulocytes (lineage^{+}) in the BAL fluid from an individual with idiopathic pulmonary fibrosis (IPF) and expression of EGR2 by the indicated populations. Data is representative of three individual patients.

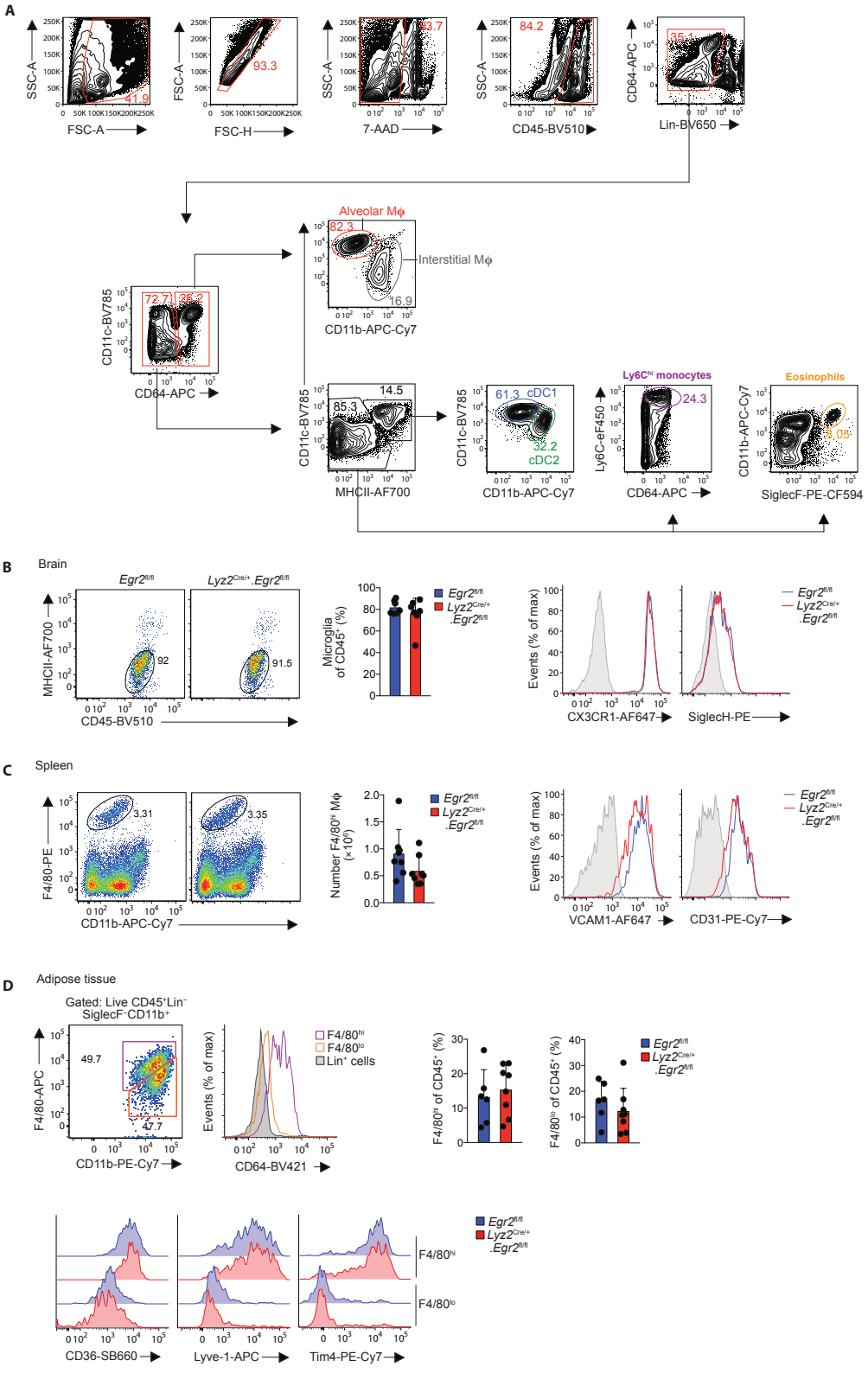

Figure S3: Effects of *Egr2* deficiency on macrophages in brain, spleen and adipose tissue

A. Gating strategy for the identification of distinct myeloid cell subsets in the lungs of *Egr2*$^{fl/fl}$ or *Lyz2*$^{Cre/+}$.*Egr2*$^{fl/fl}$ mice.

B. Representative expression of CD45 and MHCII by CD11b^{+}Ly6C^{-}lineage^{-} cells from brains of adult *Egr2*$^{fl/fl}$ or *Lyz2*$^{Cre/+}$.*Egr2*$^{fl/fl}$ mice. Graph shows the frequency of CD45^{lo}MHCII^{-} microglia of CD45^{+}

cells. Histograms show representative expression of CX3CR1 and SiglecH by CD45^{lo}MHCII^{-} microglia. Shaded histograms represent FMO controls. Data pooled from three independent experiments.

C. Representative expression of F4/80 and CD11b by lineage^{-} cells from spleens of adult *Egr2*$^{fl/fl}$ or *Lyz2*$^{Cre/+}$.*Egr2*$^{fl/fl}$ mice. Graph shows the absolute number of F4/80^{hi} macrophages per spleen in each group. Histograms show representative expression of VCAM1 and CD31 by F4/80^{hi} macrophages. Shaded histograms represent FMO controls. Data pooled from three independent experiments.

D. Representative expression of F4/80 and CD11b by lineage^{-} cells from gonadal adipose tissue of adult *Egr2*$^{fl/fl}$ mice to define mononuclear phagocyte subsets and their expression of CD64. Graphs shows the frequencies of F4/80-defined subsets in adult *Egr2*$^{fl/fl}$ or *Lyz2*$^{Cre/+}$.*Egr2*$^{fl/fl}$ mice. Histograms show representative expression of CD36, Lyve-1 and Tim4 by F4/80^{hi} macrophages. Shaded histograms represent FMO controls. Data pooled from three independent experiments.

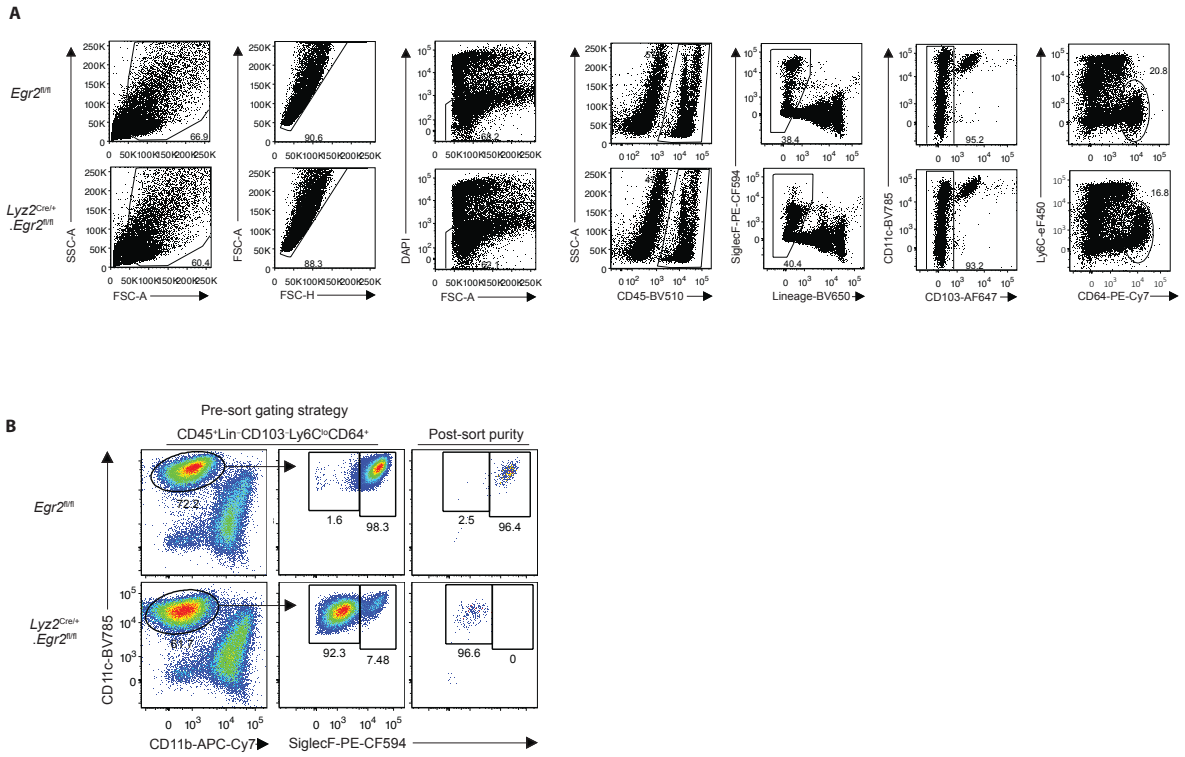

Figure S4: Gating strategy for alveolar macrophage purification and representative purity

A. Gating strategy for the FACS purification of alveolar macrophages from adult *Egr2*$^{fl/fl}$ or *Lyz2*$^{Cre/+}$.*Egr2*$^{fl/fl}$ mice for bulk RNA-seq.

B. Representative post-sort purity of alveolar macrophages in each group.

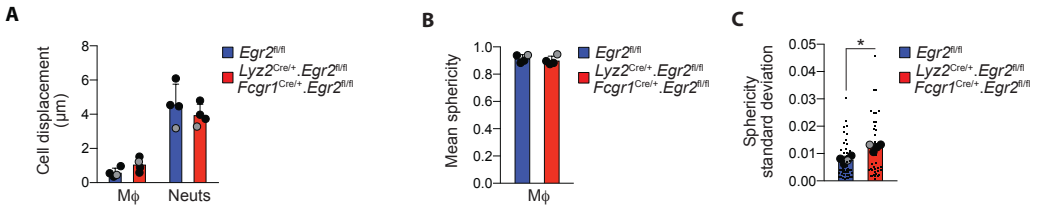

Figure S5: Analysis of alveolar macrophage motility and morphodynamics

A. Mean displacement length of alveolar macrophages and neutrophils in lungs from *Lyz2*$^{Cre/+}$.*Egr2*$^{fl/fl}$ mice (black symbols) or *Fcgr1*$^{iCre/+}$.*Egr2*$^{fl/fl}$ mice (grey symbol) or *Egr2*$^{fl/fl}$ littermate controls over 11mins in Precision Lung slices *ex vivo* – see **Data file S3** and **S4** for representative timelapse images.
B. Mean sphericity of alveolar macrophages calculated from **A**.
C. Standard deviation of alveolar macrophage sphericity over time calculated from **A**. All individual macrophages are displayed (small symbols) together with mean values for individual mice (large symbols). *p<0.05 (Mann-Whitney test).

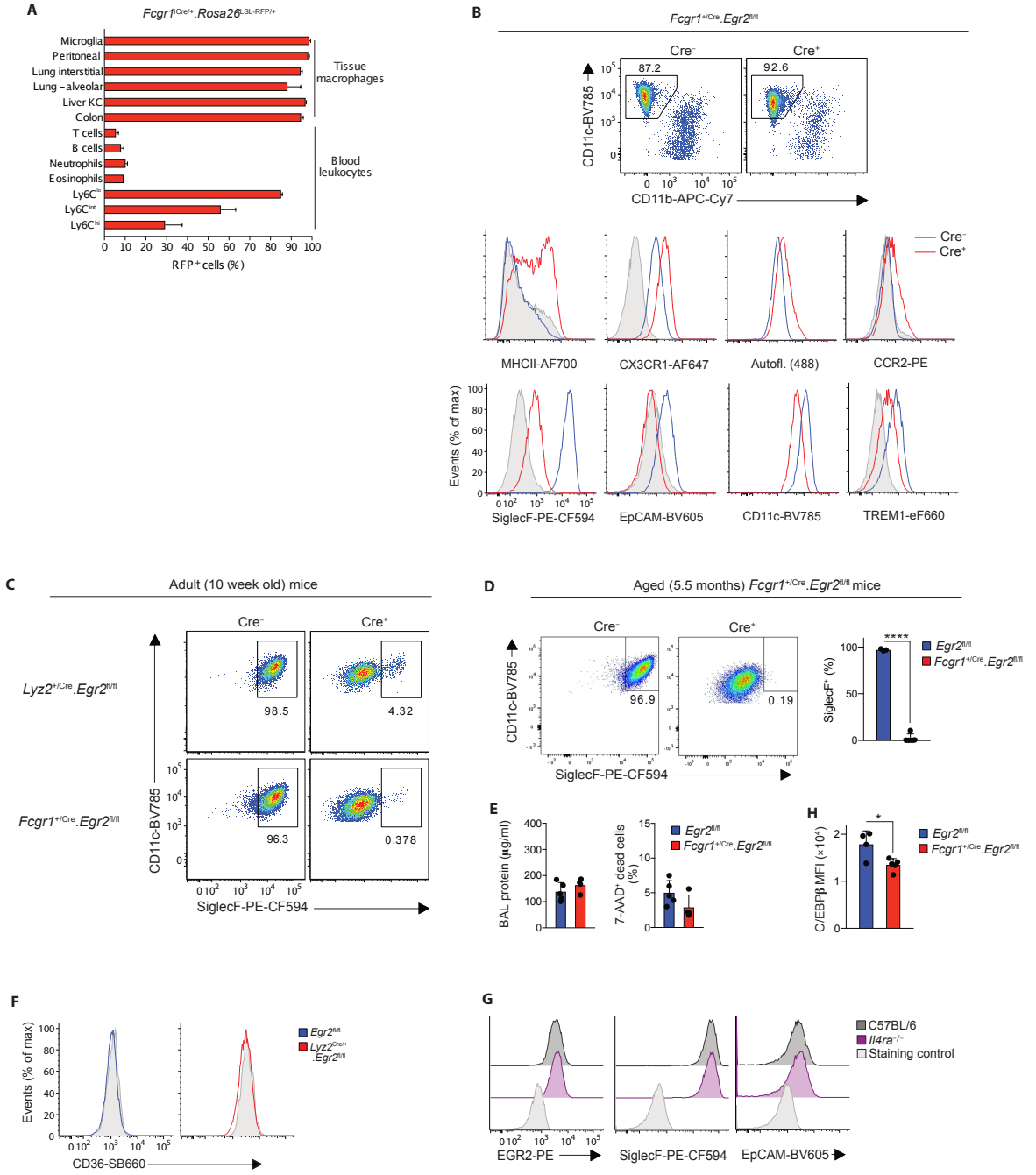

Figure S6: Analysis of *Fcgr1*$^{iCre/+}$.*Egr2*$^{fl/fl}$ and *Il4ra*$^{-/-}$ mice

A. Expression of RFP by indicated leukocytes obtained from adult *Fcgr1*$^{iCre/+}$.*Rosa26*$^{LSL\text{-}RFP/+}$ mice. Data from one of two independent experiments performed with 2-3 mice per tissue.

B. Representative expression of CD11c and CD11b by lineage^{-}Ly6C^{-}CD64^{+} cells amongst lung tissue isolates from *Egr2*$^{fl/fl}$ mice or *Fcgr1*$^{iCre/+}$.*Egr2*$^{fl/fl}$ littermates. Data are from one experiment of two performed.

C. Representative expression of CD11c and SiglecF by lineage^{-}Ly6C^{-}CD64^{+}CD11c^{+}CD11b^{-} alveolar macrophages from 8 week old *Egr2*$^{fl/fl}$ mice or *Lyz2*$^{Cre/+}$.*Egr2*$^{fl/fl}$ littermates and an independent colony of *Egr2*$^{fl/fl}$ mice or *Fcgr1*$^{iCre/+}$.*Egr2*$^{fl/fl}$ littermates. Data are from one experiment of two performed.

D. Representative expression of CD11c and SiglecF by lineage^{-}Ly6C^{-}CD64^{+}CD11c^{+}CD11b^{-} alveolar macrophages from 5.5 month old *Egr2*$^{fl/fl}$ mice or *Fcgr1*$^{iCre/+}$.*Egr2*$^{fl/fl}$ littermates. Graph shows the

frequency of SiglecF^{+} macrophages of all alveolar macrophages in each group. Data are from one experiment with 3 (*Egr2*$^{fl/fl}$) or 5 (*Fcgr1*$^{iCre/+}$.*Egr2*$^{fl/fl}$) mice per group. ****p<0.0001 (unpaired Student's *t* test).

E. Protein levels and frequency of 7-AAD^{+} dead cells in the BAL fluid of *Egr2*$^{fl/fl}$ mice or *Fcgr1*$^{iCre/+}$.*Egr2*$^{fl/fl}$ littermates at 5.5 months months of age. Symbols represent individual mice and error is s.d.. Data represent 3-4 mice per group from one experiment. Data are from one experiment with 5 (*Egr2*$^{fl/fl}$) or 5 (*Fcgr1*$^{iCre/+}$.*Egr2*$^{fl/fl}$) mice per group.

F. Representative expression of CD36 by by alveolar macrophages amongst lung digests from adult *Egr2*$^{fl/fl}$ mice or *Lyz2*$^{Cre/+}$.*Egr2*$^{fl/fl}$ littermates.

G. Expression of EGR2, SiglecF and EpCAM by alveolar macrophages amongst lung digests from adult C57BL/6 or *Il4ra*$^{-/-}$ mice. Data represent 4 mice per group from one experiment.

H. Expression of C/EBPβ (MFI) by lineage^{-}Ly6C^{-}CD64^{+}CD11c^{+}CD11b^{-} alveolar macrophages from 5.5 month old *Egr2*$^{fl/fl}$ mice or *Fcgr1*$^{iCre/+}$.*Egr2*$^{fl/fl}$ littermates. Data are from one experiment with 3 (*Egr2*$^{fl/fl}$) or 5 (*Fcgr1*$^{iCre/+}$.*Egr2*$^{fl/fl}$) mice per group. *p<0.05 (unpaired Student's *t* test).

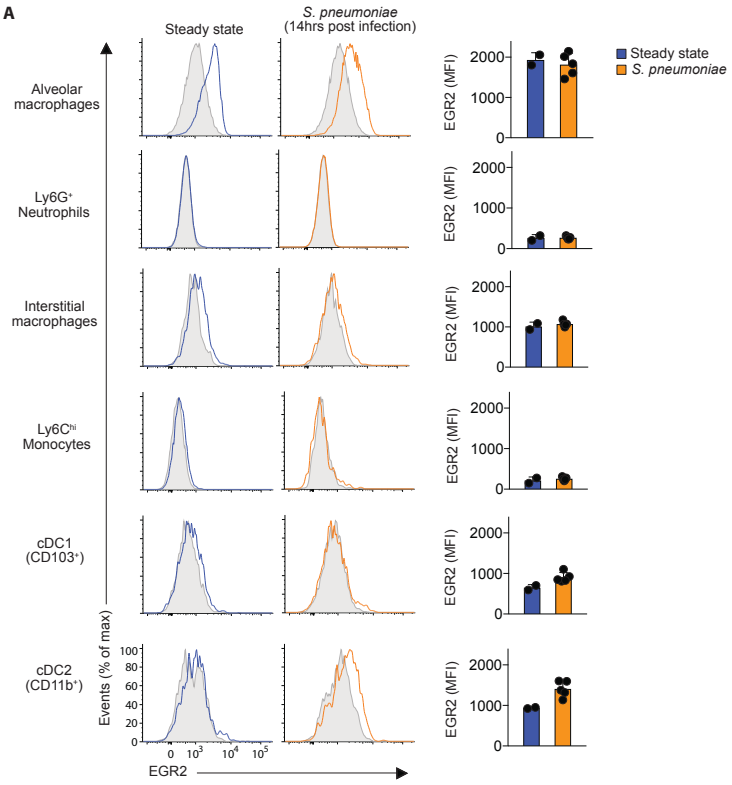

Figure S7: EGR2 expression in context of *Strepococcus pneumoniae* infection

A. Expression of EGR2 by indicated leukocytes obtained from adult *Egr2*$^{fl/fl}$ mice infected with 10^4 CFU *Streptococcus pneumoniae* 14hrs earlier (orange lines) or left uninfected (blue lines). Shaded histograms represent EGR2 expression by indicated cells from *Lyz2*$^{Cre/+}$.*Egr2* mice. Graphs show the mean fluorescence intensity (MFI) of EGR2 expression by the indicated subsets at steady state or after infection. Data are from one experiment with 2 (steady state) or 5 (*S. pneumoniae*).

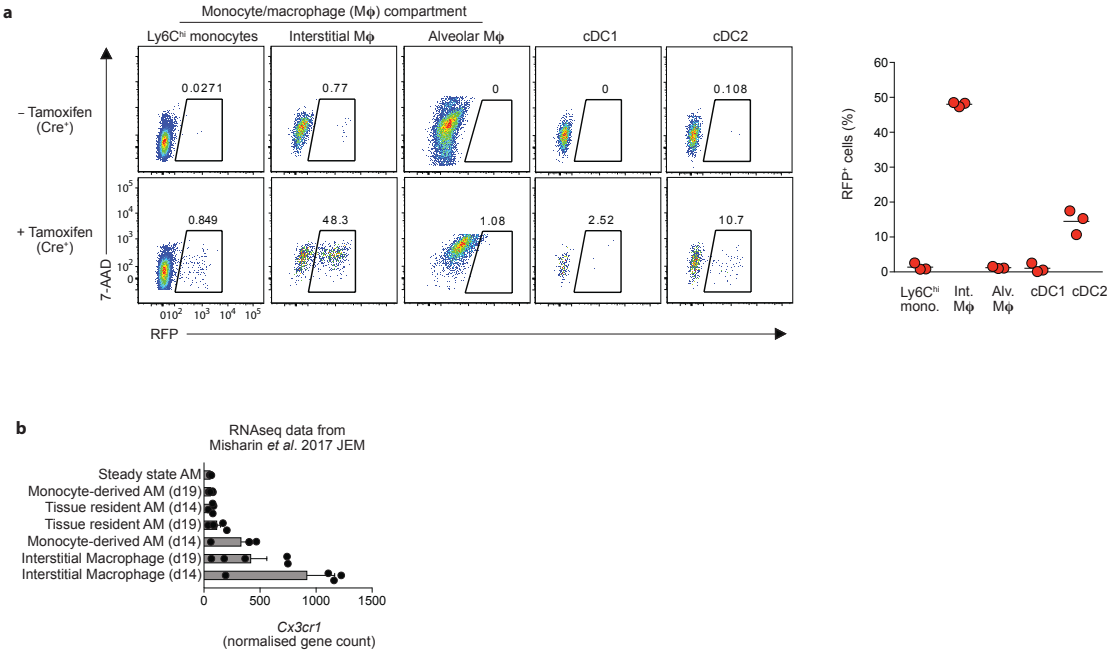

Figure S8: Validating the use of the *Cx3cr1*$^{\text{Cre-ERT2/+}}$.*Rosa26*$^{\text{LSL-RFP/+}}$ fate mapping model

A. Expression of RFP by indicated myeloid cells obtained from adult *Cx3cr1*$^{\text{Cre-ERT2/+}}$.*Rosa26*$^{\text{LSL-RFP/+}}$ mice 24hrs after the final dose of tamoxifen. Mice were administered 5mg tamoxifen by oral gavage for 5 consecutive days. Graph shows the frequency of RFP^{+} amongst each myeloid population. Data are from one of three independent experiments performed.

B. Expression of *Cx3cr1* by the indicated populations in steady state or the fibrotic phase of bleomycin-induced fibrosis. Data obtained from *(40)*.

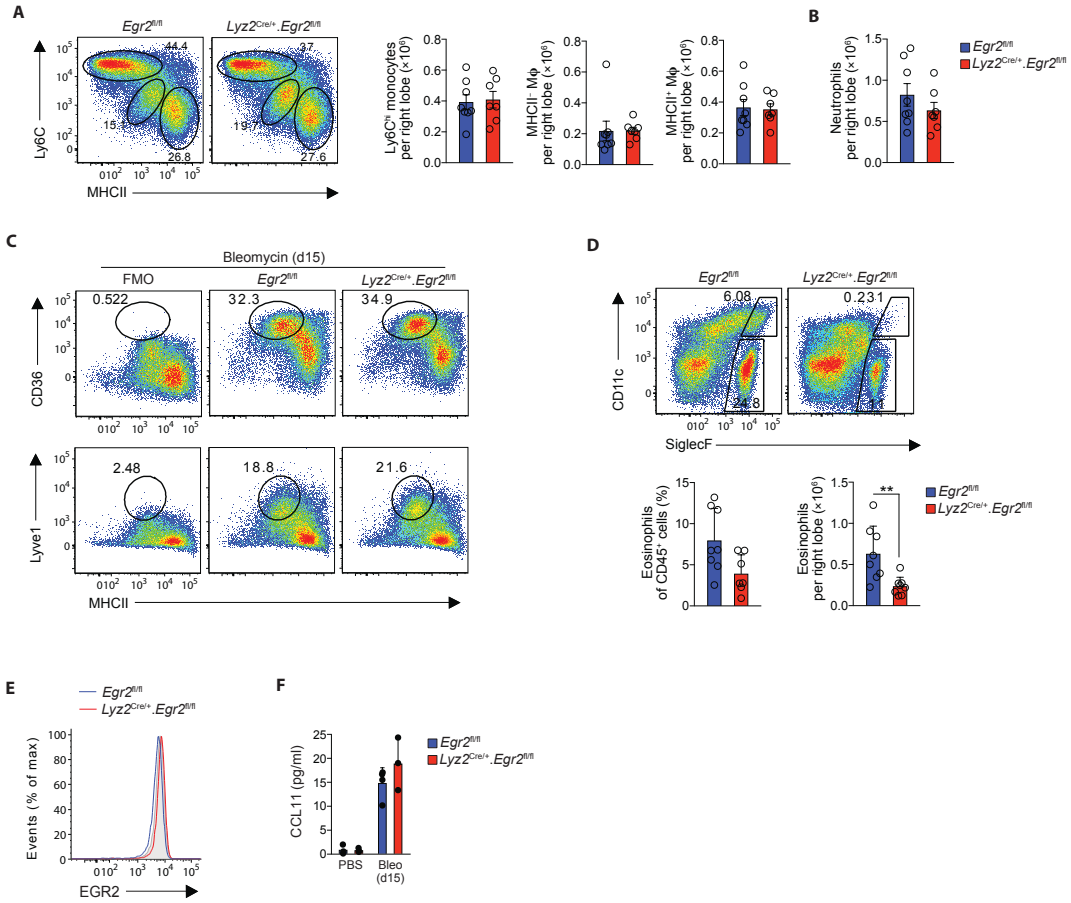

Figure S9: Effects of *Egr2* deficiency on parenchymal myeloid cells during bleomycin induced fibrosis

A. Representative expression of Ly6C and MHCII by lineage$^-$CD64$^+$CD11c^{var}CD11b$^+$ cells obtained from tissue digests of lungs obtained from adult *Egr2*$^{fl/fl}$ mice or *Lyz2*$^{Cre/+}$.*Egr2*$^{fl/fl}$ littermates 15 days after the administration of bleomycin. Graphs show the absolute number of Ly6C^{hi} monocytes and MHCII-defined macrophages per right lung lobe. **p<0.01, unpaired Student's *t* test.

B. Absolute number of Ly6G$^+$ neutrophils per right lung lobe of mice in **A**.

C. Representative expression of CD36 and Lyve-1 by Ly6C$^-$ interstitial macrophages in lungs of adult *Egr2*$^{fl/fl}$ mice or *Lyz2*$^{Cre/+}$.*Egr2*$^{fl/fl}$ littermates 15 days after the administration of bleomycin.

D. Representative expression of CD11c and SiglecF by live CD45$^+$ leukocytes obtained from tissue digests of lungs obtained from adult *Egr2*$^{fl/fl}$ mice or *Lyz2*$^{Cre/+}$.*Egr2*$^{fl/fl}$ littermates 15 days after the administration of bleomycin. Graphs show the frequency and absolute number of SiglecF$^+$CD11c^{lo} eosinophils per right lung lobe. **p<0.01 (unpaired Student's *t* test).

E. Representative expression of EGR2 by CD11c^{lo}SiglecF$^+$ eosinophils 15 days after the administration of bleomycin. Symbols represent individual mice and data are pooled from two independent experiments with 8 (*Egr2*$^{fl/fl}$) or 7 (*Lyz2*$^{Cre/+}$.*Egr2*$^{fl/fl}$) mice per group.

F. Levels of CCL11 in BAL fluid from adult *Egr2*$^{fl/fl}$ mice or *Lyz2*$^{Cre/+}$.*Egr2*$^{fl/fl}$ littermates 15 days after the administration of bleomycin or PBS controls. Symbols represent individual mice with 3-4 mice per group.

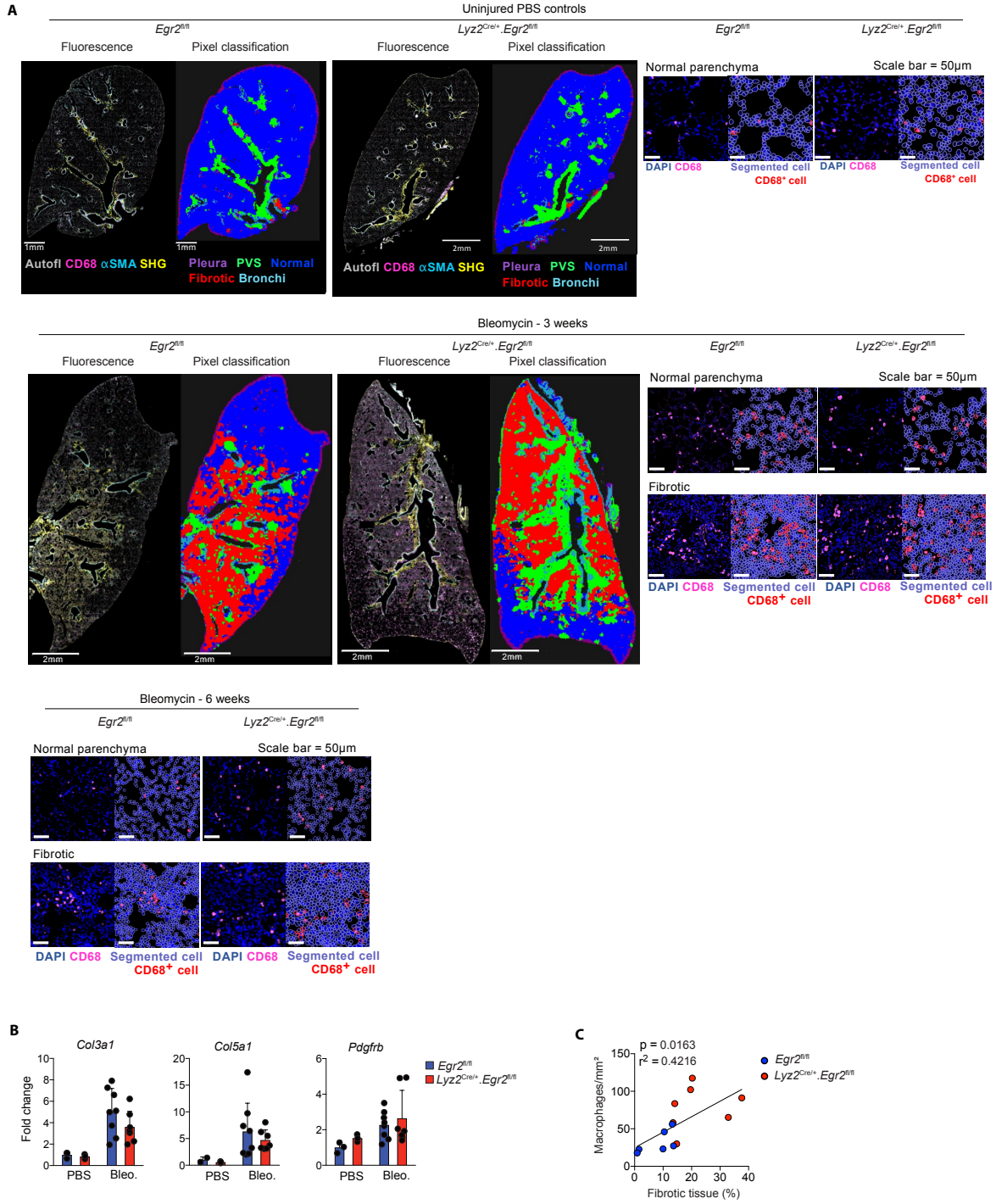

Figure S10: Assessment of the effects of *Egr2* deficiency on lung injury and fibrosis

A. 2-photon fluorescence imaging analysis of lung tissue from adult $Egr2^{fl/fl}$ mice or $Lyz2^{Cre/+}.Egr2^{fl/fl}$ mice administered PBS (uninjured) or bleomycin 3 or 6 weeks earlier. Sections were stained for CD68, αSMA and DAPI. Autofluorescence is depicted in grey and collagen detected by second harmonic generation (SHG). Pixel classification was used to segment lung regions of interest: (1) normal lung parenchyma/alveolar tissue, (2) pathologic/fibrotic tissue and (3) collagen rich areas (perivascular/bronchial spaces and pleura) were segmented to avoid false fibrotic region detection. *Right,* $CD68^{+}$ macrophage segmentation in lung parenchyma and fibrotic areas.

B. Quantitative RT-PCR analysis of *Col3a1* and *Pdgfrb* mRNA in tissue homogenates from lungs of uninjured adult *Egr2*$^{fl/fl}$ mice or *Lyz2*$^{Cre/+}$.*Egr2*$^{fl/fl}$ littermates or mice administered bleomycin 14 days earlier. Data are pooled from two independent experiments with 3 (PBS groups), 7 (*Lyz2*$^{Cre/+}$.*Egr2*$^{fl/fl}$) or 8 (*Egr2*$^{fl/fl}$) mice per bleomycin group.

C. Correlation between the number of macrophages (per mm^2) in the lung section and lung fibrosis (% of tissue). Linear regression: $R^2 = 0{,}4216$, p=0.0163. n=7 (*Lyz2*$^{Cre/+}$.*Egr2*$^{fl/fl}$) and 8 (*Egr2*$^{fl/fl}$) mice.

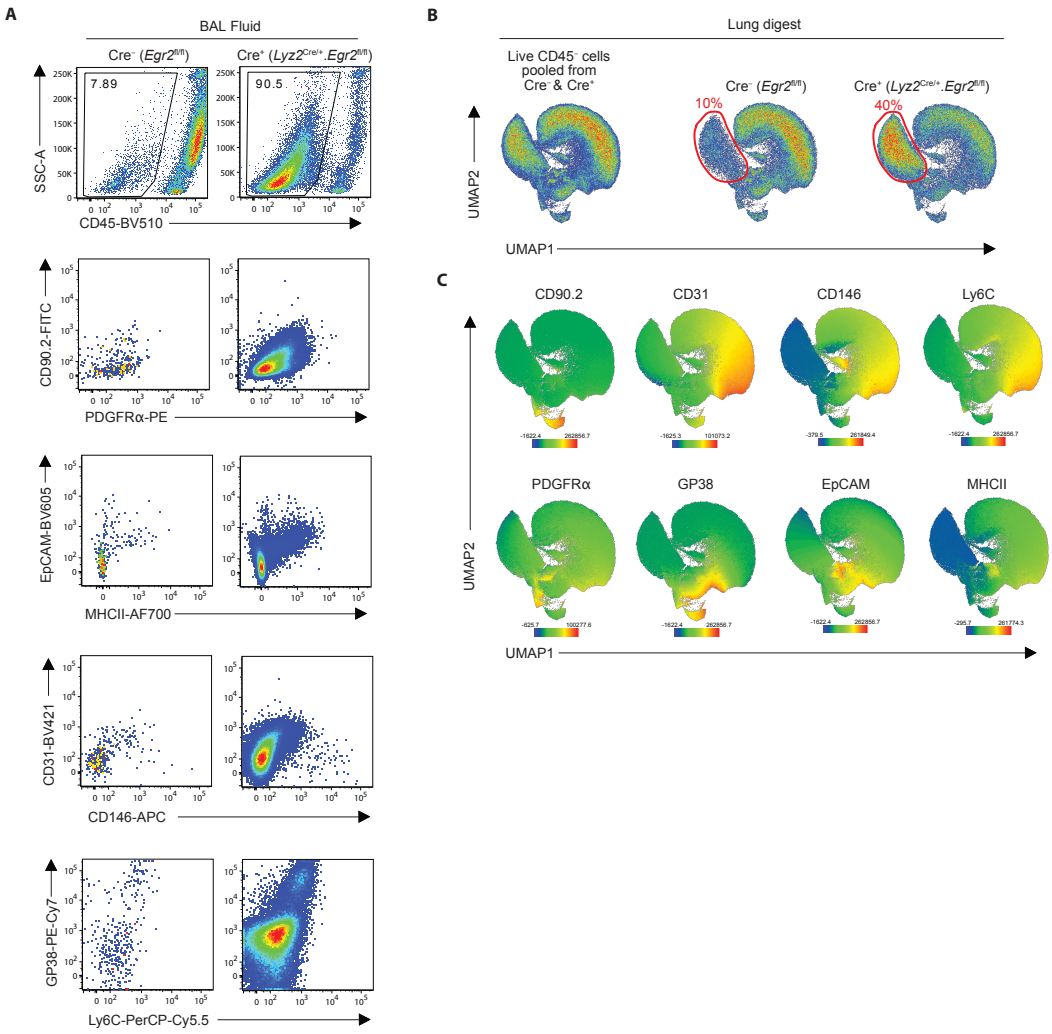

Figure S11: Phenotypic characterisation of the airway and parenchymal CD45⁻ fraction during resolution of bleomycin induced lung injury

A. Representative expression of CD45, CD90.2, PDGFRα, EpCAM, MHCII, CD31, CD146, GP38 and Ly6C by events present in the BAL fluid of adult *Egr2*$^{fl/fl}$ mice or *Lyz2*$^{Cre/+}$.*Egr2*$^{fl/fl}$ littermates administered bleomycin 6 weeks earlier.

B. UMAP analysis of CD45⁻ cells pooled from adult *Egr2*$^{fl/fl}$ mice or *Lyz2*$^{Cre/+}$.*Egr2*$^{fl/fl}$ littermates 6 weeks after bleomycin-induced injury (*left panel*). Right panel show the contribution of cells deriving from *Egr2*$^{fl/fl}$ mice and *Lyz2*$^{Cre/+}$.*Egr2*$^{fl/fl}$ mice to each cluster. Heatmap plots showing the relative expression of the indicated markers by clusters in **B**.

Table S1: Gene ontology analysis of differentially expressed genes between alveolar macrophages from *Egr2*$^{fl/fl}$ and *Lyz2*$^{Cre/+}$.*Egr2* mice (relates to Figure 3).

Process_name	Significant_genes_count	Total_genes_count	%_significant_genes	P-value	Padj-value
GO:0006935~chemotaxis	18	119	15.12605042	3.81E-06	0.01100219
GO:0060326~cell chemotaxis	12	58	20.68965517	1.03E-05	0.01482853
GO:0002376~immune system process	33	384	8.59375	4.93E-05	0.03558469
GO:0043931~ossification involved in bone maturation	5	7	71.42857143	4.66E-05	0.03558469
GO:0043406~positive regulation of MAP kinase activity	10	51	19.60784314	8.29E-05	0.04786246

Table S2: List of mouse strains

Strain	Source	Identifier
C57BL/6J CD45.1	University of Edinburgh	
C57BL/6J CD45.2^{+}	University of Edinburgh	
C57BL/6J CD45.1/.2^{+}	University of Edinburgh	
Rag1$^{-/-}$ (*Tgfbr1*$^{fl/fl}$)	University of Glasgow, UK	
Il4ra$^{-/-}$	Prof. Rick Maizels, University of Glasgow, UK	
Lyz2^{Cre}.*Egr2*$^{fl/fl}$	Generated for this study.	*Lyz2*^{Cre} mice – *(24)* *Egr2*$^{fl/fl}$ mice – *(25)*
Fcgr1^{Cre} (*B6-Fcgr1*$^{tm2\text{-}Ciphe}$)	Prof. Bernard Malissen, Dr Sandrine Henri, CIML and CIPHE, France	*(13)*
Fcgr1^{Cre}.*Egr2*$^{fl/fl}$	Generated for this study.	
Cx3cr1$^{tm2.1(cre/ERT2)Jung}$	Jackson Laboratories (JAX)	Stock ID: 020940
Rosa26$^{LSL\text{-}tdRFP}$ (*Gt(Rosa)26Sor*^{tm1Hjf})	Elaine Dzierzak, University of Edinburgh	*(70)*
Cx3cr1$^{Cre\text{-}ERT2}$.*Egr2*$^{fl/fl}$.*Rosa26*$^{LSL\text{-}RFP}$	Generated for this study.	*Cx3cr1*$^{Cre\text{-}ERT2}$ mice – *(44)*
Tgfbr2$^{fl/fl}$	Jackson Laboratories (JAX)	Stock ID: 012603
Fcgr1^{Cre}.*Tgfbr2*$^{fl/fl}$	Generated for this study.	

Table S3: List of antibodies and associated reagents

	Clone	Supplier	Cat. Number	RRID
Flow cytometry				
Mouse				
Rat monoclonal CD3 Biotin	17A2	Biolegend	100244	AB_2563947
Rat monoclonal CD11a PE-Cy7	I21/7	Biolegend	153108	AB_2716057
Rat monoclonal CD11b APC-Fire750	M1/70	Biolegend	101262	AB_2572122
Rat monoclonal CD11b PE-Cy7	M1/70	Biolegend	101216	AB_312799
Armenian hamster monoclonal CD11c BV785	N418	Biolegend	117336	AB_2565268
Rat monoclonal CD19 Biotin	6D5	Biolegend	115504	AB_313639
Rat monoclonal CD31 PE-Cy7	390	Biolegend	102418	AB_830757
Rat monoclonal CD31 BV421	390	Biolegend	102424	AB_2650892
Mouse monoclonal CD36 SuperBright 660	HM36	eBioscience	63-0362-82	AB_2734971
Rat monoclonla CD45 BV510	30-F11	Biolegend	103138	AB_2563061
Mouse monoclonal CD45.1 FITC	A20	Biolegend	110706	AB_313495
Mouse monoclonal CD45.2 AF700	104	Biolegend	109822	AB_493731
Rat monoclonal CD63 PE	NVG-2	Biolegend	143904	AB_11204430
Mouse monoclonal CD64 PE-Cy7	X54-5/7.1	Biolegend	139314	AB_2563904
Mouse monoclonal CD64 APC	X54-5/7.1	Biolegend	139306	AB_11219391
Mouse monoclonal CD64 BV421	X54-5/7.1	Biolegend	139309	AB_2562694
Rat monoclonal CD90.2 FITC	30-H12	Biolegend	105305	AB_313176
Rat monoclonal CD102 AF647	3C4	Biolegend	105612	AB_2122182
Rat monoclonal CD103 AF488	2E7	Biolegend	121408	AB_535950
Rat monoclonal CD103 AF647	2E7	Biolegend	121410	AB_535952
Rat monoclonal CD106 (VCAM1) AF647	429	Biolegend	105711	AB_493430
Rat monoclonal CD115 APC	AFS98	Biolegend	135510	AB_2085221
Rat monoclonal CD140a (PDGFRa) PE	APA5	BD Biosceince	526776	AB_2737787
Rat monoclonal CD146 APC	ME-9F1	Biolegend	134712	AB_2563088
Rat monoclonal CD192 (CCR2) PE	SA203G11	Biolegend	150610	AB_2616982
Rat monoclonal CD326 (EpCAM) BV605	G8.8	Biolegend	118227	AB_2563984
Rat monoclonal CD326 (EpCAM) PE	G8.8	Biolegend	118206	AB_1134172
Rat monoclonal CD354 (TREM1) eF660	TR3MBL1	eBioscience	50-3541-82	AB_2574205
Mouse monoclonal C/EBPb AF647	H7	Santa Cruz Biotech	Sc-7962	AB_626772
Mouse monoclonal CX3CR1 AF647	SA011F11	Biolegend	149004	AB_2564273
Rat monoclonal EGR2 PE	erongr2	eBioscience	12-6691-82	AB_10717804
Rat monoclonal EGR2 APC	erongr2	eBioscience	17-6691-82	AB_11151502
Rat monoclonal F4/80 PE	BM8	Biolegend	123110	AB_893486
Rat monoclonal GP38 PE-Cy7	8.1.1	Biolegend	127412	AB_10613648
Recombinant Ki67 FITC	REA183	Miltenyi Biotec	130-117-691	AB_2733585
Rat monoclonal Ly6C eFluor450	HK1.4	eBioscience	48-5932-82	AB_10805519
Rat monoclonal Ly6C PerCP-Cy5.5	HK1.4	Biolegend	128012	AB_1659241
Rat monoclonal Ly6G Biotin	1A8	Biolegend	127604	AB_1186108
Rat monoclonal Lyve1 eFluor 660	ALY7	eBioscience	50-0443-82	AB_10597449
Rat monoclonal MerTK PE	2B10C42	Biolegend	151506	AB_2617037
Rat monoclonal MHCII (IA-IE) AF700	M5/114.15.2	Biolegend	107622	AB_493727
Mouse monoclonal NK1.1 Biotin	PK136	Biolegend	108704	AB_313391
Rat monoclonal SiglecF PE-CF594	E50-2440	BD Bioscience	562757	AB_2687994
Rat monoclonal Siglec H PE	551	Biolegend	129605	AB_1227763
Human				
Rabbit polyclonal EGR2 (unconjugated)		Invitrogen	PA565091	AB_2662529
Mouse monoclonal HLA-DR eFluor450	LN3	eBioscience	48-9956-42	AB_10718248
Mouse monoclonal CD3 FITC	UCHT1	Biolegend	300452	AB_2564148
Mouse monoclonal CD19 FITC	HIB19	Biolegend	302206	AB_314236
Mouse monoclonal CD56 FITC	5.1H11	Biolegend	362546	AB_2565964
Mouse monoclonal CD66b FITC	G10F5	Biolegend	305104	AB_314496
Mouse monoclonal CD163 APC	RM3/1	Biolegend	326510	AB_2564015
Rat monoclonal CD11b PE-Cy7	M1/70	Biolegend	101216	AB_312799
Other flow cytometry reagents				
Streptavidin BV650	N/A	Biolegend	405232	
7-AAD		Biolegend	420404	
Zombie NIR Fiable Viability Dye		Biolegend	423106	
Immunofluorescence imaging				
Rabbit polyclonal CD68 (unconjugated)	N/A	Abcam	Ab125212	AB_10975465
Mouse monoclonal aSMA Cy3	1A4	Merck (Sigma)	C6198	AB_476856
Donkey anti-rabbit AF488	N/A	ThermoFisher	A-21206	AB_2535792
Ly6G-Dylight550	1A8	Novusbio	FAB10371L	

Rat monoclonal CD31 BV421	390	Biolegend	102424	AB_2650892
Rat monoclonal CD11b AF647	M1/70	Biolegend	101218	AB_389327
Armenian hamster monoclonal CD11c AF594	N418	Biolegend	117346	AB_2563323
Rat monoclonal CD45-Spark-NIR	30-F11	Biolegend	103168	AB_2832301

333

334 **Table S4: List of primers**

	Forward	Reverse
Ppia	5'-ACGCCACTGTCGCTTTTC-3	5'-CTGCAAACAGCTCGAAGGA-3'
Car4	5'-CAAACCAAGGATCCTAGAAGCA-3'	5'-GGGGACTGCTGATTCTCCTT-3'
Fabp1	5'-CCATGACTGGGGAAAAAGTC-3'	5'-GCCTTTGAAAGTTGTCACCAT-3'
Col3a1	5'-AACCTGGTTTC TTCTCACCCTTC-3'	5'-ACTCATAGGACTGACCAAGGTGG-3'
Pdgfrb	5'-TCCAGGAGTGATACCAGCTTT-3'	5'-CAGGAGCCATAACACGGACA-3'

335